Etude de la structure lithosphérique 3D du bouclier balte par l'analyse des ondes de Rayleigh

Marianne Bruneton

VERSITE JOSEPH FOURIER, GRENOBLE I
IRE DES SCIENCES DE L'UNIVERS DE GRENOBLE
LABORATOIRE DE GEOPHYSIQUE INTERNE ET TECTONOPHYSIQUE

Thèse de Doctorat

Spécialité: **Sciences de la Terre et de l'Univers – Terre Solide et Couches Profondes**

Marianne BRUNETON

Etude de la structure lithosphérique 3D du Bouclier Balte par l'analyse des ondes de Rayleigh

Thèse dirigée par **Helle A. PEDERSEN**

Soutenue le 29 septembre 2003

Composition du Jury:

M. M. Campillo	président	Professeur, UJF, Grenoble
Mme V. Maupin	rapporteur	Professeur, Université d'Oslo
M. J. Virieux	rapporteur	Professeur, UNSA, Nice
Mme H. A. Pedersen	directeur de thèse	Maître de Conférence, UJF, Grenoble
Mme V. Farra	examinateur	Physicien Adjoint, IPG, Paris
M. J.-J. Lévêque	examinateur	DR CNRS, EOST, Strasbourg
M. N. T. Arndt	invité	Professeur, UJF, Grenoble

UNIVERSITE JOSEPH FOURIER, GRENOBLE I
OBSERVATOIRE DES SCIENCES DE L'UNIVERS DE GRENOBLE
LABORATOIRE DE GEOPHYSIQUE INTERNE ET TECTONOPHYSIQUE

Thèse de Doctorat

Spécialité: **Sciences de la Terre et de l'Univers – Terre Solide et Couches Profondes**

Marianne BRUNETON

Etude de la structure lithosphérique 3D du Bouclier Balte par l'analyse des ondes de Rayleigh

Thèse dirigée par **Helle A. PEDERSEN**

Soutenue le 29 septembre 2003

Composition du Jury:

M. M. Campillo	président	Professeur, UJF, Grenoble
Mme V. Maupin	rapporteur	Professeur, Université d'Oslo
M. J. Virieux	rapporteur	Professeur, UNSA, Nice
Mme H. A. Pedersen	directeur de thèse	Maître de Conférence, UJF, Grenoble
Mme V. Farra	examinateur	Physicien Adjoint, IPG, Paris
M. J.-J. Lévêque	examinateur	DR CNRS, EOST, Strasbourg
M. N. T. Arndt	invité	Professeur, UJF, Grenoble

Remerciements

Le premier de mes remerciements s'adresse naturellement à ma directrice de thèse, Helle Pedersen. Pendant quatre années elle m'a guidée, m'a supportée (au sens anglophone comme francophone) et m'a remonté le moral quand nécessaire. J'ai beaucoup apprécié sa gentillesse, sa disponibilité et sa conviction scientifique. Un trait essentiel de sa personnalité réside pour moi dans l'importance qu'elle accorde aux choix de vie personnels.

Je tiens ensuite à remercier tous les membres de mon jury d'avoir bien voulu y prendre part. Le président Michel Campillo, les rapporteurs Valérie Maupin et Jean Virieux, les examinateurs Véronique Farra et Jean-Jacques Lévêque et l'invité Nick Arndt ont tous apporté des commentaires constructifs.

Merci aux collaborateurs proches ou lointains qui ont permis de construire ce travail. Bien qu'assez éloigné du projet, Georges Poupinet a prêté maintes fois sa signature de directeur de thèse officiel, de même que quelques-unes de ses excellentes idées. Véronique Farra m'a (fortement) aidée sur la théorie des rais en particulier et la théorie en général. Jérôme Mars et François Glangeaud m'ont mis le pied à l'étriller du traitement du signal. Nick Arndt et Pierre Vacher ont été indispensables à la partie interprétation de ce travail. Même si elle n'a pas abouti, la collaboration avec Eléonore Stutzman m'a apporté un nouvel éclairage sur les ondes de surface.

Je remercie chaleureusement l'ensemble des membres du projet SVEKALAPKO. Ils sont trop nombreux pour que je puisse tous les citer nommément ici mais certains ont pris une part plus active dans mon travail. Senen Sandoval s'est montré toujours serviable et disponible. Ilmo Kukkonen nous a lancés sur la piste des xénolites. Jarka Plomerová et Vladislav Babuška se sont montrés très prévenants lors de mes premiers séjours en solitaire à Lammi. Mes remerciements vont également vers tous ceux qui m'ont apporté des suggestions, des conseils et des informations toujours utiles: Edi Kissling (Zurich), Wolfgang Friederich

et Sigward Funke (Francfort), Uli Achauer (Strasbourg), Günter Bock et Ali Alinaghi (Potsdam), Annakaisa Korja et Tellervo Hyvönen (Helsinki), Sven-Eric Hjelt et Elena Kozlovskaya (Oulu), Roland Roberts (Uppsala), Monika Wilde-Piorko (Varsovie).

Voici enfin le moment de remercier tous ceux dont le travail est indispensable mais que l'on nomme rarement dans les papiers. Un immense merci à Catherine, sans elle j'aurais eu à me débattre beaucoup plus durement dans les méandres de l'informatique. Merci aux secrétaires: France, Martine, Jocelyn, Karine, Linda et Jacques. Merci aux personnels techniques, en particulier ceux avec qui j'ai travaillé sur le terrain ou au labo: Liliane, Robert, Michel et Yves. Merci à Rod Bark pour la relecture de mes papiers avec son œil anglophone. Merci enfin aux auteurs des deux livres que j'ai le plus utilisés: *A guide to LaTeX 2ε, document preparation for beginners and advanced users*, H. Kopla et P. W. Daly (Addison-Wesley, 1995), et *UNIX in a Nutshell* (O'Reilly & Associates, 1992?).

Pendant mes cinq années de présence au LGIT, j'ai pu apprécier ce cadre de vie et de travail, merci à tous ceux qui le composent. Merci aux permanents qui m'ont, suivant les cas, accueillie, écoutée, conseillée, critiquée ou aidée. Merci à tous les (ex-)étudiants que j'ai pu côtoyer: David, Mirko, François J., Nathalie, Pascal et Christophe, Super-Bruno, Marielle, Julien, Céline L., Cécile, Renaud, Bruno B., Xavier, Agnès, Martin, Mika, Olivier, Sylvie, Muriel, Céline B., Katia, Farzam et Roya, Clarisse, Ayoub, Nicolas, Nathanaël, François D., Sylvette, Eric, Ebrahim, ... et tous les autres, pour tous les moments d'échange que nous avons pu avoir. Merci aux géologues dont la venue a permis de tempérer nos bureaux et d'élargir notre horizon.

Merci aux parents, aux sœurs, aux tantes et à l'oncle, aux cousines et aux cousins qui sont là quoi qu'il arrive. Merci surtout à Vincent qui est resté tout le temps en première ligne à me soutenir quelle que soit mon humeur.

Trop de noms me viennent encore à l'esprit, je finirai donc en plagiant Rosemonde Gérard:

Grand merci à tous ceux qui m'aiment
Et qui m'entendent ici-bas,
Et grand merci aussi quand même
A tous ceux qui ne m'aiment pas.

Résumé

La tomographie sismologique à l'échelle régionale permet d'obtenir des informations sur la structure profonde des continents anciens et par suite sur leur formation et leur évolution. Nous avons développé une méthode de tomographie télésismique en ondes de surface à l'échelle régionale. Cette méthode a ensuite été appliquée aux données large-bande du projet SVEKALAPKO sur le bouclier Balte.

La méthode que nous avons développée est basée sur le tracé de rais en deux dimensions. Elle a l'avantage de prendre en considération la courbure des fronts d'onde incidents sur la région d'étude, ce qui réduit les artefacts dus aux hétérogénéités situées à l'extérieur de la zone d'étude.

L'inversion des ondes de Rayleigh nous a permis d'obtenir un profil moyen en vitesse des ondes S pour l'ensemble de la région jusqu'à 300 km de profondeur. Le modèle obtenu est environ 4% plus rapide que des modèles de Terre standards jusqu'à 200 km de profondeur, il ne présente pas de zone à moindre vitesse. La comparaison avec des données provenant d'études sur des xénolites implique une stratification chimique de la lithosphère, le manteau superficiel étant composé d'une roche produisant des vitesses sismiques plus lentes qu'une péridotite normale de lithosphère continentale.

Nous avons ensuite inversé les données SVEKALAPKO pour obtenir un modèle tridimensionnel en vitesse des ondes S sous la région couverte par le réseau jusqu'à 150 km de profondeur. Ce modèle montre des variations latérales de $\pm$ 3%, que nous attribuons à des différences de composition des roches. La principale structure géologique de la zone d'étude – la frontière Archéen-Protérozoïque – n'a pas de signature claire dans les cartes de vitesse d'onde S à différentes profondeurs. Toutefois une classification des profils de vitesse en fonction de la profondeur permet de voir apparaître une juxtaposition de blocs lithosphériques de composition différente.

Abstract

Regional seismic tomography can provide information on the deep structure of the old continents and therefore on their formation and evolution. We develop a tomography method using surface waves of teleseismic events at a regional scale. This method is then applied to the Rayleigh waves recorded during the SVEKALAPKO deep seismic experiment in the central Baltic Shield.

Our new method is based on two-dimensional ray tracing. It takes into account the curvature of incident wavefronts, therefore reducing artifacts due to heterogeneous structure outside the study region.

From the inversion of Rayleigh wave data we obtain a regional average S-wave velocity profile with depth down to 300 km. This model is 4% faster than standard Earth models down to 200 km depth, it does not exhibits any low velocity zone. A comparison with computations based on xenolith analysis leads us to propose a chemical stratification of the lithosphere. The shallower mantle is composed of a rock producing a seismic velocity slower than a normal continental lithospheric peridotite.

SVEKALAPKO data are inverted to obtain a 3-dimensionnal S-wave velocity model under the seismic array down to 150 km. Lateral variations have amplitude of $\pm$ 3% attributed to differences in the rock compositions. The major geological structure of the region – the Archean-Proterozoic boundary – does not present a clear signature in the velocity maps at different depths. However a classification of the velocity profiles with depth shows the juxtaposition of lithospheric blocs of different composition.

Table des matières

Introduction

La naissance et l'évolution des premiers continents reste une des énigmes des sciences de la Terre. En particulier les questions liées à la stabilisation de larges masses continentales sont toujours d'actualité. La présence d'un manteau lithosphérique épais, peu dense et résistant semble être un facteur clef dans la préservation de la croûte continentale contre le recyclage dans la convection mantellique. Cependant de nombreuses questions concernant cet épaississement lithosphérique subsistent: quelle est sa nature? quand se forme-t-il? sur quelle durée? par quels mécanismes? pourquoi et comment est-il préservé sur des milliards d'années?

Les méthodes géophysiques – et la tomographie sismologique en particulier – permettent de répondre à une partie de ces questions. La tomographie permet en effet d'obtenir une image de l'état actuel de l'intérieur de la Terre à différentes échelles. Cette image montre les variations de vitesse de propagation des ondes sismiques. Elle peut ensuite être interprétée en terme de température ou de composition du milieu. Les modèles tomographiques d'échelle globale ont montré que les vitesses sismiques sous les boucliers sont sensiblement plus rapides que sous les régions plus récentes, et ce jusqu'a des profondeurs de 200 à 400 km. La lithosphère continentale ancienne est donc épaisse et froide, mais la résolution de ce type d'étude ne permet pas de faire des interprétations autres que qualitatives. Les incertitudes sur les amplitudes des variations obtenues par tomographie, sur les paramètres élastiques des roches – en particulier dans les conditions de pression et de température du manteau – et la compensation entre les effets des

variations de composition et de température rendent les interprétations difficiles. Il est nécessaire de faire des hypothèses, soit en considérant que les variations de vitesse dues à la composition sont négligeables face à celles dues à la température, soit utilisant un modèle local du géotherme obtenu à l'aide d'autres types de données (ce modèle amenant ses propres incertitudes).

Les xénolites ramenées jusqu'à la surface de la Terre par des épisodes volcaniques d'origine profonde sont les seuls échantillons directs que nous ayons du manteau. Des études géochimiques et isotopiques permettent d'avoir des informations sur la composition, l'âge et parfois l'histoire de ces roches. Toutefois cet échantillonnage se fait uniquement en des points particuliers, il n'existe aucun moyen d'en vérifier la représentativité. En particulier une large majorité des xénolites mantelliques provient de profondeurs supérieures à 100-150 km, les caractéristiques du manteau continental plus superficiel sont inconnues. Coupler les informations précises mais ponctuelles des xénolites avec les informations sur la structure d'une région du globe données par la sismologie permet de formuler des hypothèses sur sa formation et son évolution.

Nous avons étudié les données large-bande d'un réseau sismologique temporaire bidimensionnel installé entre août 1998 et mai 1999 sur le bouclier Balte au sud de la Finlande. Ces données nous ont permis d'analyser les ondes de surface – mode fondamental de Rayleigh uniquement – pour des périodes comprises entre 10 et 200 secondes. Ces ondes échantillonnent la surface de la Terre jusqu'à 300 km de profondeur environ. Elles sont principalement sensibles à la vitesse de propagation des ondes S. Nous avons donc obtenu une image de la structure lithosphérique en vitesse des ondes de cisaillement, pour la région située sous le réseau de stations.

Pour améliorer les modèles issus de la tomographie, augmenter le nombre et la qualité des données ne suffit pas. Il est actuellement nécessaire de développer de nouvelles méthodes d'analyse, prenant en compte un plus grand nombre de phénomènes dus à la propagation des ondes dans un milieu réel. Pour étudier les

données large-bande finlandaises nous avons développé plus particulièrement une méthode prenant en compte la courbure des fronts d'onde.

Le premier chapitre de ce manuscrit présente le contexte général de cette étude. Y sont résumées les connaissances actuelles sur la lithosphère continentale, plus précisément dans les régions cratoniques qui ne montrent pas de traces d'événement tectonique depuis des milliards d'années. Nous donnons également une description de la Fennoscandie (bouclier Balte), région sur laquelle a porté cette étude, ainsi que du projet européen SVEKALAPKO qui en a été le point de départ.

Ce travail étant basé sur l'analyse des ondes de surface, le deuxième chapitre contient des rappels sur les caractéristiques de ces ondes. Il présente ensuite les méthodes de traitement du signal que nous avons utilisées pour l'analyse de nos sismogrammes, ainsi que les techniques permettant l'interprétation des mesures.

Le troisième chapitre décrit la méthode de tomographie télésismique en ondes de surface que nous avons développée. Cette méthode est le fruit d'une collaboration avec Véronique Farra de l'Institut de Physique du Globe de Paris. Elle est basée sur le tracé de rais en deux dimensions et utilise la théorie des rais paraxiaux pour obtenir une carte de vitesse de phase pour chaque onde et chaque période étudiée. La principale innovation réside dans le fait que nous prenons en compte la courbure des fronts d'onde incidents sur la zone d'étude. Les modifications du champ d'onde introduites par des hétérogénéités situées en dehors de la région étudiée sont donc prises en compte. Cette modélisation est possible car les récepteurs sont placés à l'intérieur de la zone d'étude et non pas simplement sur un bord comme c'est généralement le cas dans la tomographie en ondes de volume.

Dans le chapitre quatre nous présentons les résultats obtenus en terme de structure moyenne pour le centre du bouclier Balte. Notre analyse des ondes de surface a permis dans un premier temps de calculer un modèle 1D de vitesse des ondes S en fonction de la profondeur. Ce modèle est ensuite comparé à des

calculs théoriques de vitesse des ondes basés sur l'étude de xénolites mantelliques échantillonnées en Finlande. Nous analysons également un certain nombre de compositions qui nous permettraient d'expliquer les données sismologiques.

Le cinquième chapitre a pour objet le modèle tridimensionnel en vitesse des ondes S que nous avons obtenu par application de la méthode du chapitre trois. Il présente également les implications géodynamiques de nos résultats concernant l'histoire du bouclier Balte.

Chapitre 1

Contexte général de cette étude

Mon travail de thèse a porté sur les données d'une expérience sismologique de grande envergure, le projet SVEKALAPKO. Ce chapitre présente tout d'abord les connaissances et les questions encore en suspens qui ont amené des chercheurs à construire ce projet. Ces questions concernent la lithosphère continentale des cratons et plus précisément celle du bouclier Balte en Scandinavie.

1.1 La lithosphère continentale

La lithosphère est définie comme l'enveloppe superficielle rigide de la Terre comprenant la croûte et une partie du manteau supérieur. D'un point de vue rhéologique il s'agit d'une couche mécaniquement résistante posée sur l'asthénosphère mécaniquement plus faible ayant un comportement ductile aux échelles de temps géologiques. D'un point de vue thermique la lithosphère est une couche limite à travers laquelle la chaleur interne de la Terre est perdue par conduction alors qu'elle est transmise par convection dans le manteau sous-jacent. Sa température doit également être inférieure au solidus pour être en accord avec le comportement mécanique. En sismologie l'asthénosphère a été définie comme une zone à moindre vitesse, phénomène ayant été associé à la présence éventuelle

de fusion partielle. La présence de fluides permet aussi de définir une lithosphère électromagnétique résistante sur un conducteur asthénosphérique. Ces différentes définitions de la lithosphère correspondent à des processus physiques différents et donc généralement à des profondeurs différentes.

Dans un contexte océanique la lithosphère est simplement modélisée par un refroidissement de matériel mantellique. Celui-ci arrive en surface au niveau de la ride océanique avec une température donnée puis s'éloigne en refroidissant. La base de la lithosphère est alors définie comme une isotherme, soit celui marquant la transition entre un comportement rigide et un comportement visqueux (lithosphère mécanique), soit celui à partir duquel le gradient de température est adiabatique (lithosphère thermique, légèrement plus épaisse). Dans ce cas les mesures correspondent bien au modèle, les expériences sismologiques sont également compatibles.

En contexte continental la situation est beaucoup plus complexe. Un simple modèle de refroidissement ne permet plus d'expliquer la majorité des données. La lithosphère continentale gagne une définition supplémentaire en terme de pétrologie puisqu'elle est considérée comme une couche appauvrie en constituants basaltiques. Les définitions chimiques et physiques de la lithosphère peuvent alors être incompatibles en terme d'épaisseur. La lithosphère continentale est également beaucoup plus diversifiée que la lithosphère océanique, des différences importantes sont observées entre les régions tectoniques actives, les plates-formes phanérozoïques et les boucliers et plates-formes précambriens. Sur des péridotites mantelliques Boyd [1989] a étudié les différences géochimiques entre ces différents types de lithosphère. Les observations d'épaisseur importante de la lithosphère sous les cratons ont amené Jordan [1979] à définir la tectosphère comme une couche mécaniquement faible mais chimiquement de caractère lithosphérique qui suivrait le mouvement des plaques rigides. Kukkonen & Peltonen [1999] ont été amenés à des conclusions similaires par une étude de xénolites d'origine mantellique échantillonnées en Finlande. En effet leurs calculs rhéologiques basés sur le

géotherme obtenu par thermobarométrie donnent une épaisseur de la lithosphère mécanique comprise entre 130 et 185 km; alors que la structure et la composition des xénolites permettent de conclure à une épaisseur de la lithosphère chimique et thermique de l'ordre de 240 km. Sous les continents une zone à moindre vitesse n'est pas systématiquement observée, la lithosphère peut alors être définie en sismologie comme la limite en dessous de laquelle les hétérogénéités sont faibles et ne sont plus corrélées avec des structures superficielles.

1.2 Le Précambrien

Les régions du globe qui n'ont pas subi d'événement tectonique depuis plus d'un milliard d'années sont appelées des cratons. La plupart possèdent un cœur de matériel continental formé dès l'Archéen il y a plus de 2,5 Ga (figure 1.1).

D'un point de vue géophysique, ces régions sont caractérisées par un faible flux de chaleur et des vitesses sismiques élevées. Le flux de chaleur est de l'ordre de 40 mW/m^2 [Nyblade, 1999] alors que la moyenne pour les continents s'élève à 57 mW/m^2 et la moyenne globale à 82 mW/m^2 [Fowler, 1990]. Les vitesses sismiques sont plus élevées de quelques pourcents jusqu'à des profondeurs de plusieurs centaines de kilomètres [voir par exemple, Montagner & Tanimoto, 1991]. Cette signature s'explique au premier ordre par l'évolution thermique de ces régions. Elles sont très anciennes, depuis longtemps à l'équilibre thermique et n'ont pas été réchauffées par des événements tectoniques. Il en résulte une lithosphère épaissie et plus froide qui explique le flux de chaleur et les vitesses sismiques plus élevées.

Mais le refroidissement entraîne une augmentation de la densité qui tendrait à faire disparaître la lithosphère dans la convection mantellique. Pour expliquer la stabilité des cratons Jordan [1979] a proposé une différence de composition du manteau lithosphérique. La lithosphère cratonique serait composée de matériel plus fortement appauvri en éléments basaltiques. Boyd [1989] a montré, dans une

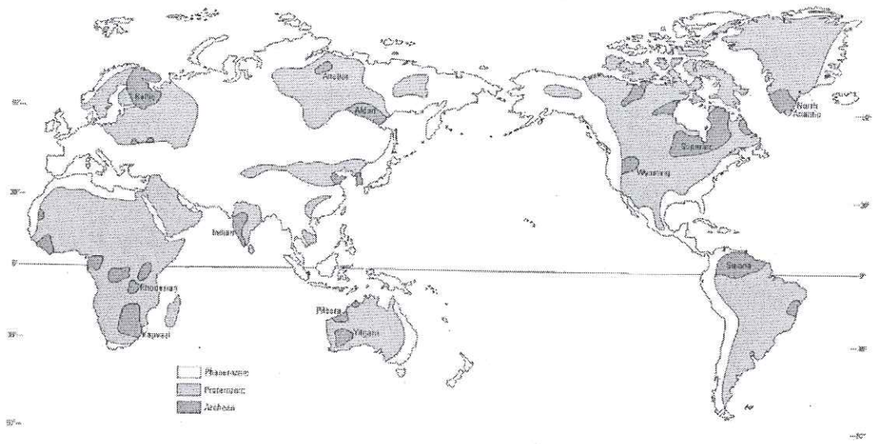

FIG. 1.1 – *Distribution des roches archéennes (plus de 2,5 Ga) et protérozoïques (entre 530 Ma et 2,5 Ga) d'après Dalrymple [1991].*

étude sur les xénolites du craton Kaapvaal en Afrique du Sud, que le manteau lithosphérique des cratons constituait une hétérogénéité chimique substantielle par rapport à la lithosphère océanique et à la lithosphère continentale hors craton. Le lien entre le pourcentage d'olivine modale[1] et le rapport magnésium sur magnésium plus fer[2] de plusieurs ensembles d'échantillons montre des différences nettes entre les lithosphères océanique et continentale récente d'une part et la lithosphère cratonique d'autre part (figure 1.2). Cet auteur suppose que ce matériel est formé par l'extraction d'un magma ultramafique plutôt que basaltique (c'est-à-dire qu'il contient presque exclusivement des silicates ferromagnésiens) et à de très grandes profondeurs (supérieures à 200 km). Ces magmas très riches en fer et magnésium auraient formé les komatiites, laves exclusivement archéennes, et auraient laissé un résidu fortement appauvri. Le résultat de cet appauvrissement en terme de vitesses sismiques est complexe [Goes *et al.*, 2000]. Le grenat et

1. Pourcentage d'olivine parmi les minéraux mesurés dans la roche
2. «Mg number» généralement utilisé comme indice de la fusion partielle

le clinopyroxène vont être les premiers minéraux à disparaître, le grenat étant le minéral le plus rapide et le clinopyroxène le plus lent des minéraux principaux l'effet total est mineur avec généralement une très légère augmentation des vitesses. L'effet le plus important est une augmentation des vitesses due à la diminution du contenu en fer.

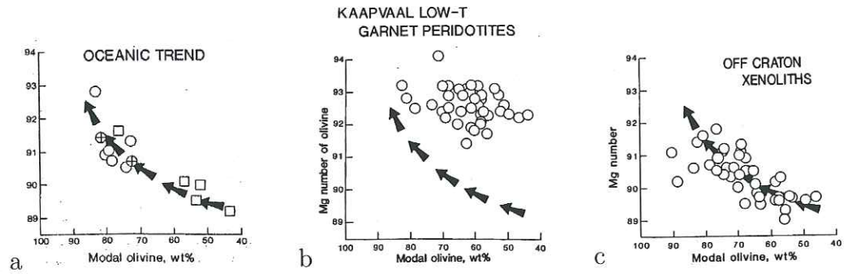

FIG. 1.2 – *Différences géochimiques entre a) une séquence de résidus de basaltes océaniques; b) les xénolites du craton Kaapvaal et c) des xénolites trouvées hors craton. L'abscisse est la quantité d'olivine modale dans les échantillons en pourcentage du poids, l'ordonnée est le rapport Mg/(Mg+Fe) [figure 1, 2 et 4 de Boyd, 1989].*

Les komatiites sont pratiquement inconnues dans des terrains plus récents que l'Archéen, il est probable que le refroidissement général de la Terre ait fait disparaître les conditions dans lesquelles elles se formaient. D'un point de vue géochimique la lithosphère archéenne est donc sensiblement différente d'une lithosphère continentale ou océanique plus récentes. Il reste à déterminer si ces différences ont un effet sur les vitesses sismiques suffisamment important et systématique pour être détecté.

1.3 La Fennoscandie

1.3.1 Tectonique

Le bouclier Balte regroupe l'ensemble des roches précambriennes affleurant au Nord de l'Europe. La Fennoscandie est une unité crustale plus large qui couvre le bouclier Balte et continue sous les sédiments Riphéens (mésoproterozoïques) à l'Est et au Sud. Elle se termine à l'Est par un fossé tectonique, l'aulacogène de Volhyn-Russie Centrale, qui la sépare des segments crustaux de Volga-Oural à l'Est et de Sarmatie au Sud-Est (figure 1.3a). Ces trois unités forment le craton Est-Européen. Le bouclier Balte est la seule partie de ce craton qui présente des roches précambriennes exposées sur de larges étendues.

La Fennoscandie est formée par un cœur de roches archéennes, la Carélie, bordée au Nord-Est par la ceinture Laponie-Kola, datée de la fin Archéen et du début Protérozoïque, et au Sud-Ouest par la Svecofennie d'âge protérozoïque (figure 1.3b) [Gorbatschev & Bogdanova, 1993]. Cette étude concerne les provinces de Carélie et de Svecofennie.

La formation des granites et roches vertes de Carélie a débuté il y a environ 3,5 milliards d'année et s'est continuée pendant l'Archéen avec des orogenèses importantes autour de 2,9 et 2,7 Ga [Gorbatschev & Bogdanova, 1993]. La croissance de cette croûte continentale a continué sur une très longue échelle de temps à la fin de l'Archéen et au Protérozoïque par l'accrétion de blocs lithosphériques en particulier vers le Nord-Est avec les terrains de Laponie et de la presqu'île de Kola.

La structure du domaine Svecofennien était jusqu'à récemment considérée comme relativement simple [Gorbatschev & Bogdanova, 1993]. Il serait composé d'un vaste domaine de roches sédimentaires détritiques métamorphisées, entouré de ceintures volcaniques. La plupart des âges de formation de ces roches sont situées entre 1,9 et 1,86 Ga. Toutefois les études les plus récentes proposent une

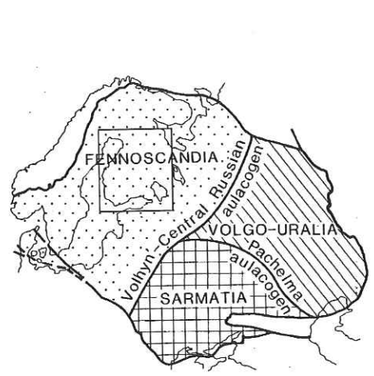

a

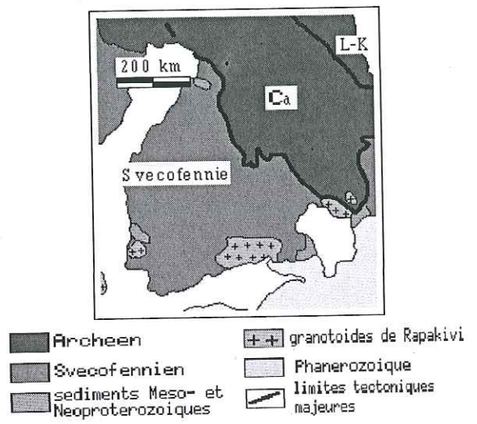

b

FIG. 1.3 – *a) Segments crustaux du craton Est-Européen, d'après Gorbatschev & Bogdanova [1993]; le rectangle marque la région d'étude. b) Carte géologique simplifiée du centre du bouclier Balte (modifié d'après Hjelt & Daly [1996]); Ca: Carélie, L-K: Laponie-Kola.*

histoire beaucoup plus complexe. Nironen *et al.* [2002] ont proposé une succession de cinq orogenèses entre 1,92 et 1,79 Ga. Ces orogenèses auraient accolé un certain nombre de micro-continents et d'arcs insulaires formés préalablement, d'abord entre eux, puis avec la Carélie déjà stabilisée. Elles se superposent en partie en espace et en temps et alternent, en particulier à la frontière Archéen-Protérozoïque, avec des épisodes d'extension continentale. Ces conclusions sont étayées entre autre par les observations électromagnétiques qui montrent une structure complexe dans le bloc Svecofennien [Korja *et al.*, 2002; Engels *et al.*, 2002]. Les derniers événements tectoniques enregistrés dans ces roches sont de nature extensive avec l'intrusion des granitoïdes de Rapakivi (1,65-1,2 Ga) et la sédimentation des grès Subjotniens (1,2 Ga) [Korja *et al.*, 1993]. Depuis cette époque, la Fennoscandie n'a pas été reprise dans des événements tectoniques, si ce n'est sur sa bordure Ouest lors de l'orogenèse Calédonienne.

1.3.2 Structure lithosphérique

La Finlande est une des régions au monde les mieux couvertes par des profils sismiques portant sur toute l'épaisseur de la croûte [pour une compilation des différents profils, voir Luosto, 1997]. Ces profils ont permis de mettre en évidence une croûte anormale ayant une épaisseur moyenne de près de 50 km et pouvant atteindre 65 km par endroit malgré l'absence de topographie en surface. Cette croûte anormalement épaisse est caractérisée par une couche inférieure très rapide avec des vitesses d'onde P comprises entre 7 et 7,7 km.s^{-1} [Korja *et al.*, 1993].

Une nouvelle interprétation des données sismiques a été menée récemment par Sandoval *et al.* [2003], aboutissant à un modèle de croûte tridimensionnel en vitesse des ondes P.

De nombreuses études sismologiques d'échelle lithosphérique ont également eu lieu en Scandinavie. Les tentatives de mesure de l'épaisseur de la lithosphère donnent des valeurs très variables entre 170 et 350 km.

Sacks *et al.* [1979] ont interprété des données de conversions d'ondes S en ondes P comme la limite lithosphère-asthénosphère située à 250 km de profondeur. Cette mesure est basée sur un modèle de vitesse extrêmement simple et utilise uniquement cinq événements. Une tomographie en ondes P a été menée par Husebye & Hovland [1982]. Leur paramétrisation comprend des blocs de 250 km de coté environ et quatre niveaux en profondeur (0-100 km, 100-300 km, 300-500 km, 500-600 km). Ils observent une hétérogénéité notable dans la tranche 100-300 km, relativement bien corrélée avec la couche superficielle. Dans le niveau suivant les variations latérales sont beaucoup plus faibles et non corrélées. Ils en déduisent que la base de la lithosphère en dessous de laquelle il ne doit plus y avoir de variations latérales se situe vers 300 km de profondeur. Des analyses de dispersion d'ondes de Rayleigh ont été interprétées comme montrant la base de la lithosphère plus basse que 170 km [Calcagnile, 1982], puis autour de 350 km [Calcagnile, 1991]. Elles sont basées sur très peu de données, aucun profil ne recoupe la région d'intérêt de cette étude. Récemment Sandoval [2002]; Sandoval *et al.* [submitted] ont trouvé par une tomographie en ondes P à haute résolution une structure rapide située au centre de la Finlande et descendant jusqu'à 300 km de profondeur. Cette structure est interprétée comme une racine lithosphérique.

De grandes incertitudes subsistent donc sur l'étendue et la structure de la lithosphère dans cette région. Des informations supplémentaires peuvent également être apportées par l'étude des xénolites présentes dans les kimberlites de Finlande. Kukkonen & Peltonen [1999] ont étudié une série d'échantillons mantelliques provenant de kimberlites à l'est de la Finlande. La thermobarométrie montre qu'ils sont originaires de profondeurs allant jusqu'à 230 km alors qu'ils présentent tous une structure de type lithosphérique (sans signe de cisaillement). Les auteurs supposent que la base de la lithosphère est située au moins à 230-240 km de profondeur. Les xénolites montrent également une stratification de la lithosphère. En effet les échantillons provenant de profondeurs inférieures à 110 km ont une composition de lithosphère archéenne très appauvrie, alors que les

échantillons plus profonds sont plus fertiles.

1.4 Le projet SVEKALAPKO

Le bouclier Balte présente des terrains n'ayant pas été remaniés par la tectonique depuis plus d'un milliard d'années, non recouverts de sédiments et déjà en partie connus suite à de nombreuses études géophysiques. C'est donc un endroit idéal pour étudier les différences entre lithosphères archéenne et protérozoïque.

Cette région a été choisie pour l'une des investigations du programme EUROPROBE [Gee & Zeyen, 1996]: le projet SVEKALAPKO [SVEcofenia-KArelia-LAPland-KOla, Hjelt & Daly, 1996]. Comme élément d'une approche pluridisciplinaire une expérience de sismologie passive a eu lieu entre août 1998 et mai 1999 [Bock & SVEKALAPKO Seismic Tomography W. G., 2001]. Son objectif était de donner une image précise du système lithosphère-asthénosphère au centre de la Fennoscandie, en particulier à travers la frontière Archéen-Protérozoïque.

Ce projet était proposé comme la continuation vers le Nord-Est du programme TOR [Gregersen & TOR W. G., 1999]. Celui-ci a permis d'obtenir une coupe d'échelle lithosphérique partant de l'Europe phanérozoïque (centre de l'Allemagne), traversant l'éventail de Tornquist au Danemark pour finir en Suède sur le bouclier Balte. Le modèle en vitesse d'ondes S obtenu par Cotte & Pedersen [2002] montre des variations nettes et abruptes dans la structure lithosphérique des différents compartiments (figure 1.4). Les modèles obtenus par tomographie en ondes de volume [Shomali *et al.*, 2002; Arlitt, 1999] sont très proches. Le pari du projet SVEKALAPKO était de voir une structure du même type entre le Protérozoïque et l'Archéen, mais en trois dimensions. De plus, étant donné que cette région n'a pas subi d'événement thermique majeur depuis des centaines de millions d'année, d'éventuelles variations des vitesses sismiques ne peuvent pas y être expliquées en terme de température et sont forcément dues à des différences lithologiques.

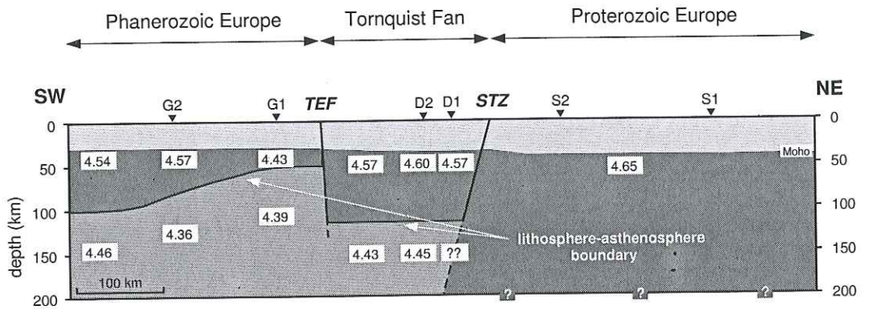

FIG. 1.4 – *Coupe d'échelle lithosphérique le long du réseau TOR d'après l'analyse des ondes de surface [Cotte & Pedersen, 2002].*

Quinze instituts ont participé au déploiement et à l'entretien du réseau de stations sismologiques: Centre Scientifique de Kola RAS Apatity, Université de Grenoble, Université de Helsinki, Institut de Physique de la Terre RAS Moscou, Spetzgeofisika MNR Moscou, Université d'Oulu, GFZ Potsdam, Institut de Géophysique CAS Prague, Université de Saint Petersbourg, Université de Strasbourg, Université de Stuttgart, Université d'Uppsala, Université d'Utrecht, Université de Varsovie et Institut de Géophysique ETH Zurich.

Le réseau comprenait 144 stations temporaires ou permanentes, distribuées sur une grille bidimensionnelle de 500 sur 700 km (figure 1.5). La distance entre deux stations courte période est d'environ 50 km et 100 km entre deux stations large-bande. Ce réseau a été dessiné pour avoir une bonne résolution jusqu'à 400 km de profondeur pour la tomographie en ondes de volume.

De tous les tremblements de Terre ayant eu lieu entre août 1998 et mai 1999, une liste comprenant 1356 séismes a été sélectionnée pour être analysée par les différents participants du projet. Parmi ces événements 442 sont des téléséismes de distance épicentrale supérieure à 30° et de magnitude supérieure à 5,0. Les autres sont des séismes proches et des explosions de carrière. Les données ont

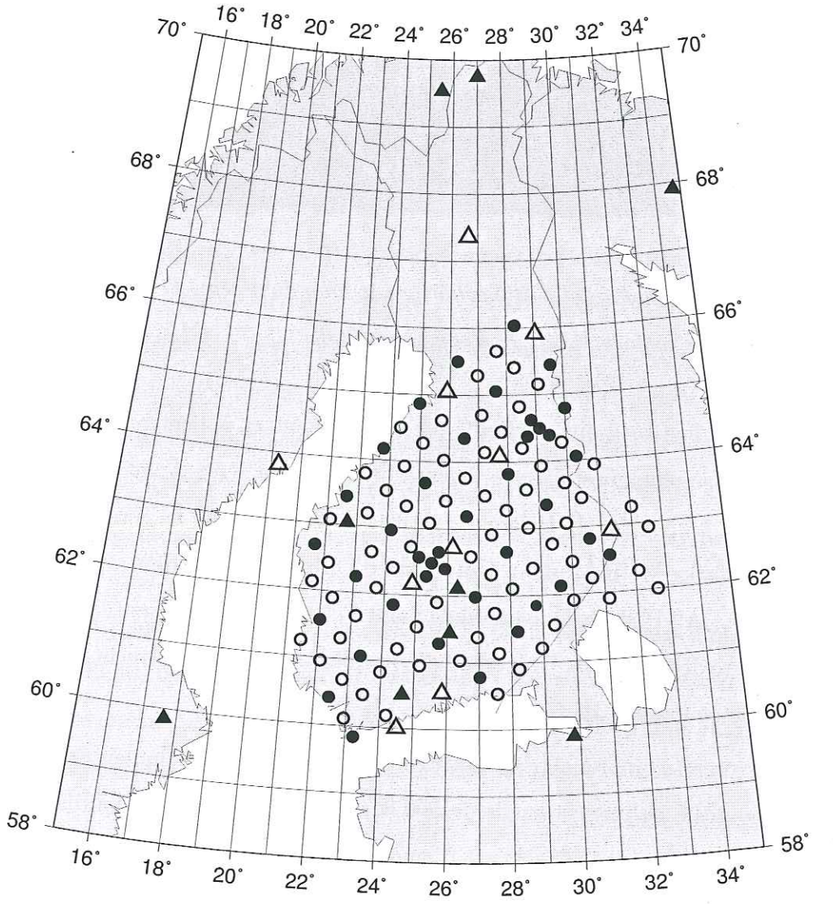

FIG. 1.5 – *Réseau de stations sismologiques de l'expérience SVEKALAPKO; cercle: station temporaire; triangle: station permanente; signe plein: sismomètre large-bande; signe vide: courte période.*

d'abord été extraites des bandes de terrain dans chaque institut, transférées dans un format commun, rassemblées et redistribuées. Ces manipulations ont pris plus de deux ans, les données complètes et corrigées n'ont été disponibles qu'à partir de la fin de l'année 2001.

Bibliographie

Arlitt, R., 1999. *Teleseismic body wave tomography across the Trans-European Suture Zone between Sweden and Denmark*, thèse de doctorat, Swiss Federal Institute of Technology, Zurich.

Bock, G. & the SVEKALAPKO Seismic Tomography Working Group, 2001. Seismic probing of Fennoscandian lithosphere, *EOS, Trans. Am. Geophys. Un.*, **82**, 621, 628–629.

Boyd, F. R., 1989. Compositional distinction between oceanic and cratonic lithosphere, *Earth Plant. Sci. Lett.*, *96*, 15–26.

Calcagnile, G., 1982. The lithosphere-asthenosphere system in Fennoscandia, *Tectonophysics*, **90**, 19–35.

Calcagnile, G., 1991. Deep structure of Fennoscandia from fundamental and higher mode dispersion of Rayleigh waves, *Tectonophysics*, **195**, 139–149.

Cotte, N. & H. A. Pedersen, 2002. Sharp contrast in lithospheric structure across the Sorgenfrei-Tornquist Zone as inferred by Rayleigh wave analysis of TOR1 project data, *Tectonophysics*, **360**, 75–88.

Dalrymple, G. B., 1991. *The age of the Earth*, Stanford University Press, Stanford, California.

Engels, M., T. Korja and the BEAR Working Group, 2002. Multisheet modelling of the electrical conductivity structure in the Fennoscandian Shield, *Earth Planets Space*, **54**, 559–573.

Fowler, C. M. R., 1990. *The solid Earth, an introduction to global geophysics*, Cambridge University Press.

Gee, D. G. & H. J. Zeyen (eds.), 1996. *EUROPROBE 1996 – lithosphere dynamics: origin and evolution of continents*, EUROPROBE secretariat, Uppsala University, Uppsala, Sweden.

Goes, S., R. Govers & P. Vacher, 2000. Shallow mantle temperatures under Europe from P and S wave tomography *J. Geophys. Res.*, **105**, 11153–11169.

Gorbatschev, R. & S. Bogdanova, 1993. Frontiers in the Baltic Shield. *Precambrian Res.*, **64**, 3–21.

Gregersen, S. & the TOR Working Group, 1999. Important findings expected from Europe's largest seismic array, *EOS, Trans. Am. Geophys. Un.*, **80**, 1–2.

Hjelt, S.-E. & J. S. Daly, 1996. SVEKALAPKO, evolution of Paleoproterozoic and Archean lithosphere, in *EUROPROBE 1996 – lithosphere dynamics: origin and evolution of continents*, D. G. Gee and H. J. Zeyen (eds.), EUROPROBE secretariat, Uppsala University, Uppsala, Sweden.

Husebye, E. S. & J. Hovland, 1982. On upper mantle seismic heterogeneities beneath Fennoscandia, *Tectonophysics*, **90**, 1–17.

Jordan, T. H., 1979. The deep structure of the continents, *Scientific American*, **240**, 92–107.

Korja, A., T. Korja, U. Luosto & P. Heikkinen, 1993. Seismic and geoelectric evidence for collisional and extensional events in the Fennoscandian Shield – implication for Precambrian crustal evolution, *Tectonophysics*, **219**, 129–152.

Korja, T., M. Engels, A. A. Zhamaletdinov, A. A. Kovtun, N. A. Palshin, M. Y. Smirnov, A. D. Tokarev, V. E. Asming, L. V. Vanyan, I. L. Vardaniants and the BEAR Working Group, 2002. Crustal conductivity in Fennoscandia – a compilation of a database on crustal conductance in the Fennoscandian Shield, *Earth Planets Space*, **54**, 535–558.

Kukkonen, I. T. & P. Peltonen, 1999. Xenolith-controlled geotherm for the central Fennoscandian Shield: implications for lithosphere-asthenosphere relations. *Tectonophysics*, **304**, 301–315.

Luosto, U., 1997. Structure of the Earth's crust in Fennoscandia as revealed from refraction and wide-angle reflection studies, *Geophysica*, **33**, 3–16.

Montagner, J.-P. & T. Tanimoto, 1991. Global upper mantle tomography of seismic velocities and anisotropies, *J. Geophys. Res.*, **96**, 20337–20351.

Nironen, M., R. Lahtinen & A. Korja, 2002. Paleoproterozoic tectonic evolution of the Fennoscandian shield – comparison to modern analogues, in *Lithosphere 2002 – second symposium on the structure, composition and evolution of the lithosphere in Finland. Programme and extended abstracts, Espoo, Finland*, R. Lahtinen, A. Korja, K. Arhe, O. Eklund, S.-E. Hjelt and L. J. Pesonen (eds.), Institute of Seismology, University of Helsinki, report S-42, 95–97.

Nyblade, A. A., 1999. Heat flow and the structure of Precambrian lithosphere, *Lithos*, **48**, 81–91.

Sacks, I. S., J. A. Snoke & E. S. Husebye, 1979. Lithosphere thickness beneath the Baltic Shield, *Tectonophysics*, **56**, 101–110.

Sandoval, S., 2002. *The lithosphere-asthenosphere system beneath Fennoscandia (Baltic Shield) by body-wave tomography*, thèse de doctorat, Swiss Federal Institute of Technology, Zurich.

Sandoval, S., E. Kissling, J. Ansorge & the SVEKALAPKO Seismic Tomography Working Group, 2003. High-resolution body wave tomography beneath the SVEKALAPKO array: I. A priori 3D crustal model and associated traveltime effects on teleseismic wavefronts, *Geophys. J. Int.*, **153**, 75–87.

Sandoval, S., E. Kissling, J. Ansorge & the SVEKALAPKO Seismic Tomography Working Group, submitted. High-resolution body wave tomography beneath the SVEKALAPKO array: II. anomalous upper mantle structure beneath central Baltic Shield, *Geophys. J. Int.*.

Shomali, H. Z., R. G. Roberts & the TOR Working Group, 2002. Non-linear body wave teleseismic tomography along the TOR array, *Geophys. J. Int.*, **148**, 562–574.

Chapitre 2

Ondes de surface: théorie et méthodes

Mon travail au sein du projet SVEKALAPKO est entièrement basé sur l'analyse des ondes de surface. Ce chapitre a pour objet de présenter les principales caractéristiques des ondes de surface ainsi que les méthodologies classiques que nous avons utilisées: filtrage temps-fréquence, mesure de délais en temps, inversion de courbes de dispersion pour déterminer des modèles lithosphériques de vitesse des ondes S en fonction de la profondeur et prise en compte de l'atténuation.

2.1 Les ondes de surface

Ce chapitre a été rédigé à l'aide de divers ouvrages qui ne seront pas cités au long du texte: Aki & Richards [2002], Coulomb & Jobert [1972] et Keilis-Borok [1989].

Les séismes sont dus à une brusque rupture de roches le long d'une surface de faille. Dans un milieu élastique homogène et isotrope il y a alors propagation d'énergie sous forme de deux types d'ondes dans le milieu élastique environnant. Ces deux types d'ondes sont les ondes de compression dites ondes P, et les ondes

de cisaillement dites ondes S.

Si le milieu présente une surface libre, on voit également se développer les ondes de surface qui se propagent parallèlement à cette surface et sont évanescentes en grande profondeur la profondeur. Du fait de leur propagation le long d'une surface leur atténuation due à l'expansion géométrique est plus faible que celle des ondes de volume qui se propagent en trois dimensions. Dès que l'on s'éloigne de la source elles dominent en amplitude le signal sismique pour les périodes de 10 à 200 s. Leur vitesse de propagation apparente plus lente que les ondes de volume permet également de les séparer sur des séismes lointains (figure 2.1). Cette figure montre également qu'elles sont dispersives, c'est-à-dire que les différentes fréquences se propagent à des vitesses différentes.

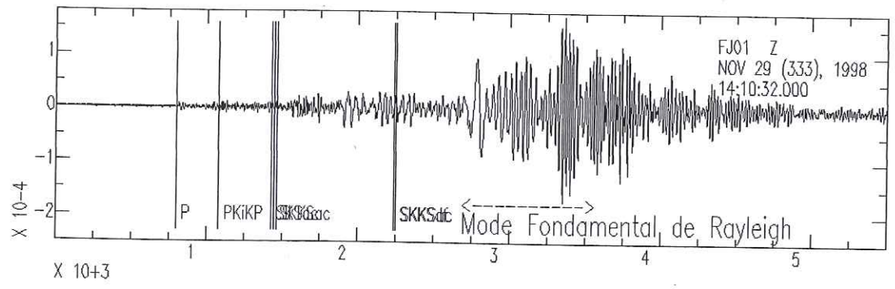

FIG. 2.1 – *Composante verticale du signal enregistré par la station FJ01 provenant du séisme du 29 novembre 1998 au Sud des Philippines en Indonésie (magnitude Mw=7,7 (GS)). L'abscisse est le temps en secondes, l'ordonnée l'amplitude des mouvements en unités arbitraires.*

2.1.1 Ondes de Rayleigh et de Love

Il existe deux types d'ondes de surface: les ondes de Rayleigh et les ondes de Love. Les ondes de Rayleigh résultent d'un couplage le long de la surface libre entre des ondes P et des ondes S_V (ondes S de polarisation verticale).

Le mouvement des particules sous le passage de cette onde se fait dans le plan contenant les composantes verticales et radiales, selon un mouvement elliptique rétrograde. Les ondes de Love sont créées par les interférences constructives des ondes S_H piégées entre la surface libre et des interfaces profondes, elles sont dépendantes des variations de vitesse des ondes S en profondeur. Le mouvement des particules est horizontal transverse.

Sur un enregistrement trois composantes, s'il n'y a pas d'hétérogénéités latérales, l'onde de Rayleigh est présente sur les composantes verticale et radiale, l'onde de Love uniquement sur la composante transverse. L'onde de Rayleigh est isolée sur la composante verticale des sismogrammes. Pour isoler l'onde de Love, il faut faire une rotation des composantes horizontales dans la direction de propagation de l'onde, pour transformer les composantes Nord et Est de la station sur le terrain en composantes radiale et transversale par rapport au séisme. De plus, si le milieu n'est pas isotrope et homogène le mouvement des particules dû à l'onde de Love et celui dû à l'onde de Rayleigh peuvent ne pas être parfaitement perpendiculaires. Il devient alors difficile de les séparer complètement. Le niveau de bruit sur les composantes horizontales d'un sismogramme est aussi généralement plus élevé que sur la composante verticale. Pour ces raisons, nous n'avons travaillé dans cette étude que sur l'onde de Rayleigh enregistrée sur la composante verticale des sismogrammes.

2.1.2 Caractéristiques des ondes de surface

Les ondes de surfaces sont décrites par la résolution de l'équation des ondes avec pour conditions aux limites une surface libre (tractions nulles) et une amplitude tendant vers zéro à l'infini dans la direction opposée. De telles solutions n'existent pas pour des pulsations ω et des nombres d'onde k quelconques. Pour une valeur donnée de ω, il peut exister un certain nombre de valeurs $k_n(\omega)$ permettant de trouver une solution. Ces valeurs particulières de k sont les valeurs

propres de la fonction d'onde. La plus grande de ces valeurs propres k_0 correspond au mode fondamentale de l'onde considérée (Rayleigh ou Love), les valeurs propres suivantes correspondent aux modes appelés supérieurs ou harmoniques.

La vitesse de phase de chacune de ces ondes particulières va également dépendre de ω et de la solution particulière k_n:

$$c_n(\omega) = \frac{\omega}{k_n(\omega)} \tag{2.1}$$

Ces vitesses de phase prennent également des valeurs discrètes c_0, c_1, c_2, ... pour chaque mode. Les courbes $c_n(\omega)$ montrent l'évolution de la vitesse de propagation d'une phase particulière en fonction de ω, ce sont les courbes de dispersion en vitesse de phase.

Un paquet d'onde constitué de contributions de fréquences proches de ω se propage avec une vitesse de groupe $U(\omega)$ généralement différente de $c(\omega)$. Les pics, creux et zéros du paquet d'onde se propagent eux à la vitesse de phase $c(\omega)$. La vitesse de groupe traduit la vitesse de propagation de l'enveloppe du signal, autrement dit de l'énergie. Elle est égale à:

$$U_n(\omega) = \frac{d\omega}{dk_n(\omega)} \tag{2.2}$$

La vitesse de groupe est reliée à la vitesse de phase par les équations:

$$U = c + k\frac{dc}{dk} = c - \lambda\frac{dc}{d\lambda} \tag{2.3}$$

où λ est la longueur d'onde.

Les ondes de surface échantillonnent la surface de la Terre avec une sensibilité qui diminue avec la profondeur. La forme de cette sensibilité dépend du mode considéré et de la longueur d'onde étudiée. La figure 2.2 montre l'amplitude normalisée du déplacement des particules pour le mode fondamental de l'onde de Rayleigh dans un demi-espace homogène en fonction de la profondeur. Pour le mode fondamental de Rayleigh on considère généralement que la profondeur de pénétration est de l'ordre de $\lambda/3$ où λ est la longueur d'onde. Pour les modes supérieurs la distribution de l'énergie augmente la sensibilité en profondeur pour une même fréquence.

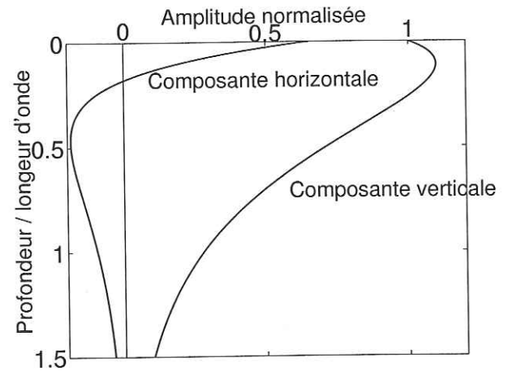

FIG. 2.2 – *Amplitude normalisée du mouvement des particules au passage du mode fondamental de l'onde de Rayleigh en fonction de la profondeur, dans un demi-espace homogène.*

2.2 Méthodes utilisées dans cette étude

2.2.1 Filtrage temps-fréquence

Dans un sismogramme brut peuvent coexister tous les types d'ondes (de volume et de surface) et tous les modes. Il contient également un certain niveau de bruit aléatoire ou cohérent, le bruit cohérent correspond à une partie du signal que nous ne souhaitons pas analyser ici, due à tous les paquets d'énergie qui ont suivi des chemins différents du chemin direct en raison des hétérogénéités du milieu. Ces différentes contributions peuvent être superposées en temps et/ou en fréquence rendant inefficace une coupure en temps ou un filtrage simple.

Pour isoler le signal qui nous intéresse, par exemple le mode fondamental de l'onde de Rayleigh, nous allons tirer partie de la dispersion des ondes de surface. Elle permet en effet d'identifier dans le plan temps-fréquence une courbe de dispersion et d'éliminer (parfois en partie seulement) la partie du sismogramme qui correspond à d'autres ondes.

La méthode que nous utilisons est développée par Herrin & Goforth [1977]

[voir aussi Lander & Levshin, 1989], le code a été écrit par Baumont [1999].

La première étape consiste en une analyse du sismogramme dans un plan temps-fréquence. Le signal $x(t)$ est filtré dans la gamme de fréquences visée et une fenêtre en temps contenant le paquet d'énergie qui nous intéresse est sélectionnée. Son spectre $X(\omega)$ est calculé par transformée de Fourier, ω étant la pulsation. Dans le domaine fréquentiel nous appliquons un filtrage multiple avec une fenêtre glissante centrée en ω_0:

$$X'(\omega_0) = X(\omega)\ e^{-\frac{1}{2}\left(\frac{\omega-\omega_0}{\alpha\omega_0}\right)^2} \tag{2.4}$$

le paramètre α détermine la largeur relative du filtre.

Pour chaque fréquence ω_0 une transformée de Fourier inverse est calculée:

$$D(t,\omega_0) = \frac{1}{\sqrt{2\pi}} \int_{-\infty}^{\infty} X'(\omega_0) e^{i\omega t} d\omega \tag{2.5}$$

La figure 2.3 représente l'enveloppe de $D(t,\omega_0)$ dans le plan temps-fréquence. L'amplitude est normalisée pour chaque fréquence de façon à pouvoir définir la courbe de dispersion sur la plus vaste gamme fréquentielle possible. L'amplitude de l'enveloppe pour une fréquence ω_0 donnée passe par un maximum pour des temps $t_g(\omega_0)$ correspondant aux temps d'arrivée des groupes de fréquence ω_0 pour les différents modes présents dans le signal.

Par pointé sur cette représentation graphique, nous mesurons la courbe de vitesse de groupe du signal que l'on cherche à extraire. La vitesse de groupe $U(\omega_0)$ étant simplement reliée au temps $t_g(\omega_0)$ par la distance épicentrale *dist*.

Nous voulons ensuite filtrer le signal pour ne conserver que la partie située dans une bande centrée sur la courbe de dispersion sélectionnée dans le plan temps-fréquence. Pour cela il faut déphaser le signal pour amener tous les temps de groupe $t_g(\omega_0)$ à interférer au même temps t_0. Le déphasage $\Phi(\omega)$ à imposer à chaque phase de pulsation ω est:

$$\Phi(\omega) = \omega(t_0 - t_\phi(\omega)) \tag{2.6}$$

où $t_\phi(\omega)$ est le temps d'arrivée de la phase de pulsation ω. Le calcul de $t_\phi(\omega)$ est basé sur la relation 2.3 entre vitesse de groupe U et vitesse de phase c et sur

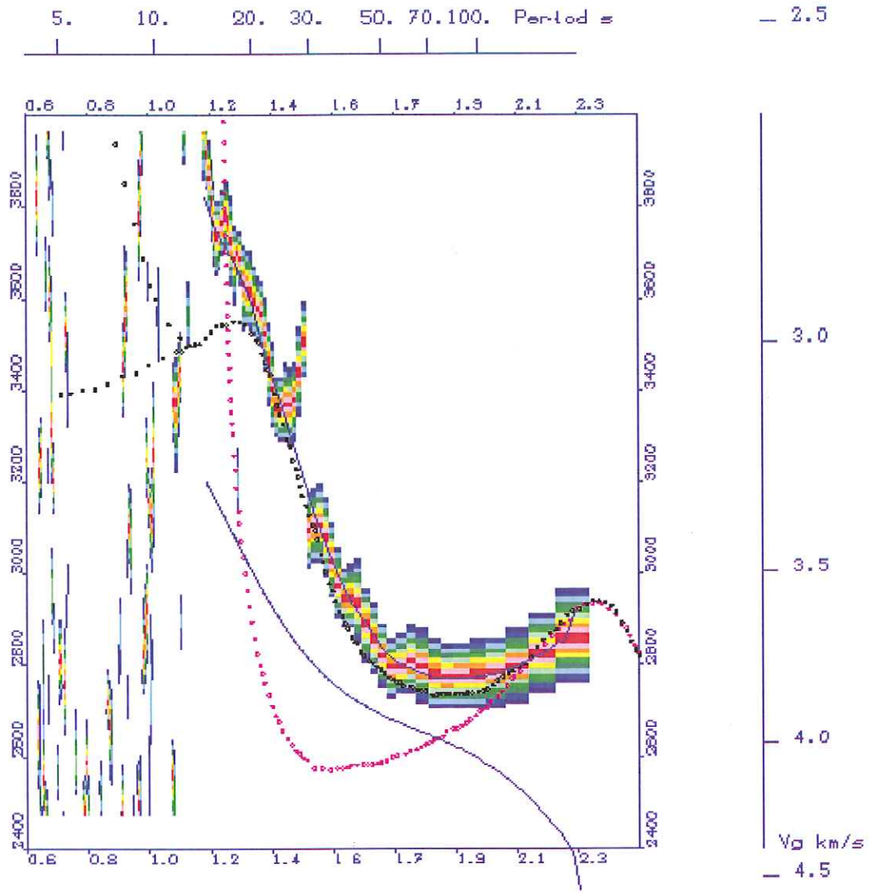

FIG. 2.3 – *Image du signal de la figure 2.1 dans le plan temps – logarithme décimal de la période (amplitude maximale en rouge) et sélection visuelle de la courbe de temps de groupe (courbe en trait plein sur les zones d'amplitude maximale); les pointillés donnent des valeurs moyennes de dispersion en milieu continental (noir) et océanique (rose); la ligne continue qui ne suit pas l'image du signal est la courbe des temps de phase.*

l'égalité $t_g\ U = t_\phi\ c = dist$ [Baumont, 1999]:

$$\omega\ t_\phi(\omega) = \omega_i\ t_\phi(\omega_i) + \int_{\omega_i}^{\omega} t_g(\omega_q) d\omega_q \tag{2.7}$$

Cette formulation suppose qu'il existe une phase de pulsation ω_i pour laquelle t_ϕ est connu et que le temps de groupe $t_g(\omega_q)$ est défini entre ω_i et ω. Ce point d'ancrage est choisi d'après les travaux d'Olivier [1962] à une période de 200 s. A cette période les vitesses de phase en milieux continentaux et océaniques convergent avec une valeur de 4,55 km.s^{-1} pour le mode fondamental de l'onde de Rayleigh.

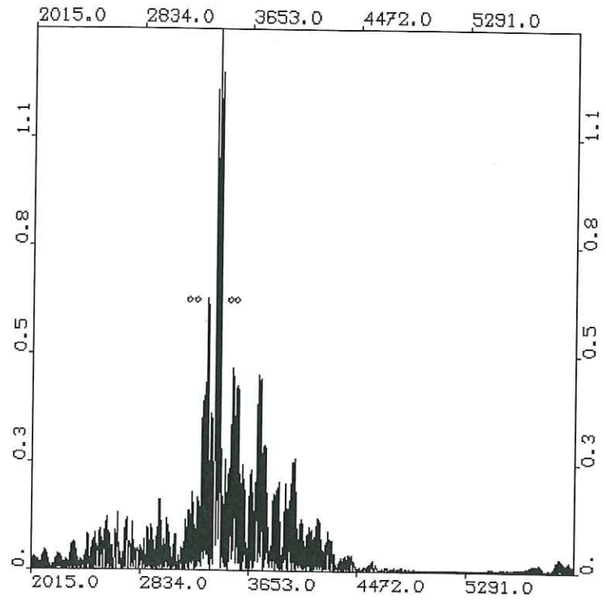

FIG. 2.4 – *Signal temporel après soustraction de la dispersion observée en vitesse de groupe; les ronds autour du pic marquent la position de la fenêtre de filtrage.*

Le signal obtenu après déphasage est présenté dans la figure 2.4. Ce signal est alors apodisé par une fenêtre centrée sur le temps t_0. Enfin la phase $\Phi(\omega)$ précédemment enlevée au signal est ajoutée. Après une transformée de Fourier inverse, nous retrouvons notre signal en temps avec un rapport signal sur bruit fortement amélioré (figure 2.5). L'ensemble des signaux utilisés dans cette étude

pour deux événements sont dessinés dans les figures 2.6 et 2.7 avant et après filtrage temps-fréquence.

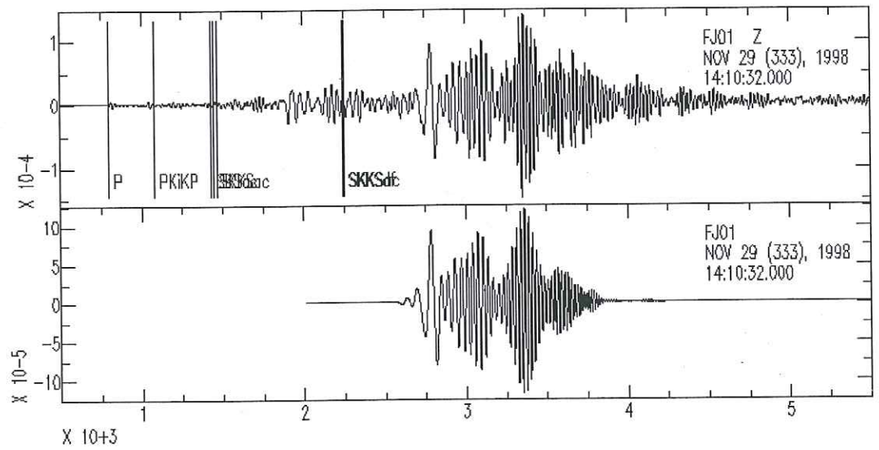

FIG. 2.5 – *Signal sismique avant (haut) et après (bas) filtrage temps-fréquence.*

Cette méthode est souvent indispensable pour pouvoir mesurer des délais en temps entre signaux car elle diminue les instabilités dues à des interférences d'ondes ou à du bruit. Son principal inconvénient est que la sélection d'une courbe de dispersion de référence pour une série de traces est manuelle. Cela implique d'une part un temps de traitement des données conséquent et d'autre part une sélection laissée au propre arbitre de l'utilisateur, donc subjective.

2.2.2 Mesure des délais en temps

Le temps de propagation d'une onde peut se mesurer entre la source et la station, ou entre deux stations. La première possibilité suppose de connaître la phase du signal source et de modéliser l'ensemble du trajet de l'onde. Dans le cadre du projet SVEKALAPKO nous nous intéressons uniquement à la région comprise sous le réseau de stations temporaires, nous avons donc mesuré des temps de propagation relatifs entre les stations de ce réseau. Cette mesure a en outre l'avantage

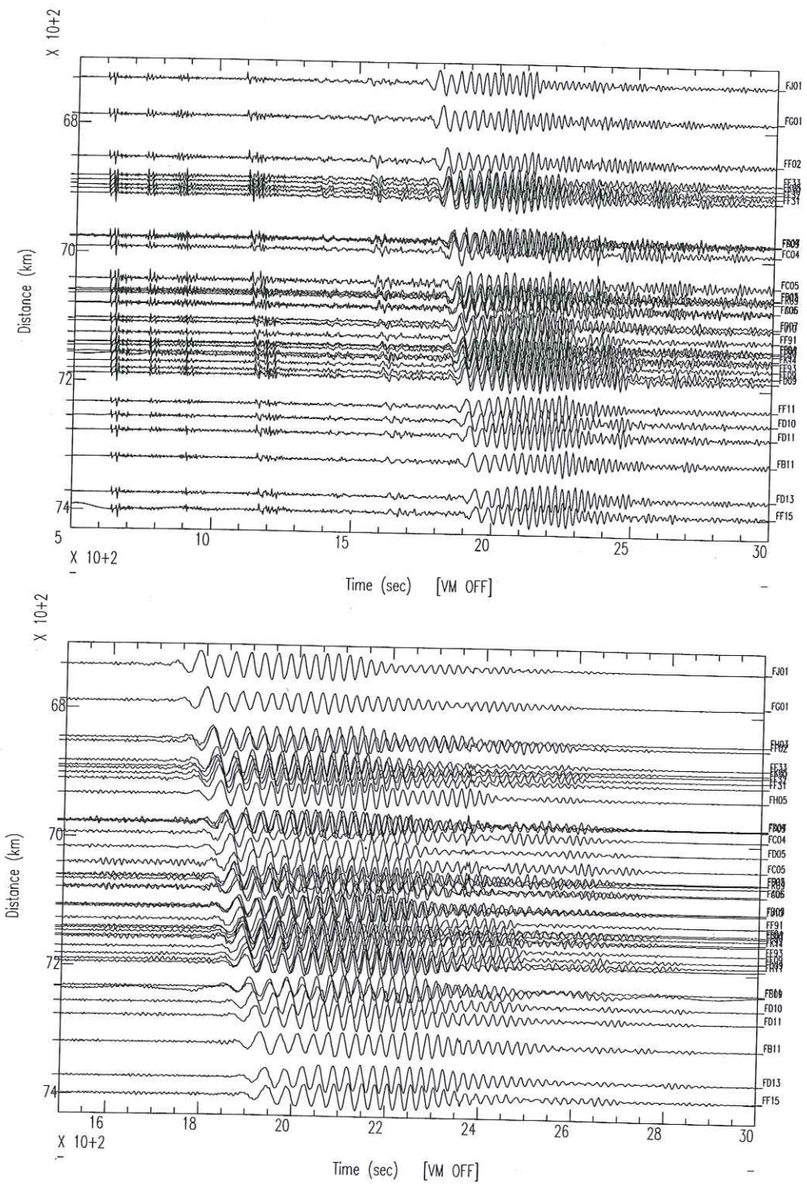

FIG. 2.6 – *Section de sismogrammes pour le séisme du 28 janvier 1999 (Mw=6,6 d=64°): haut avant filtrage temps-fréquence; bas après filtrage (tous les signaux sont filtrés entre 12 et 200 secondes de période.*

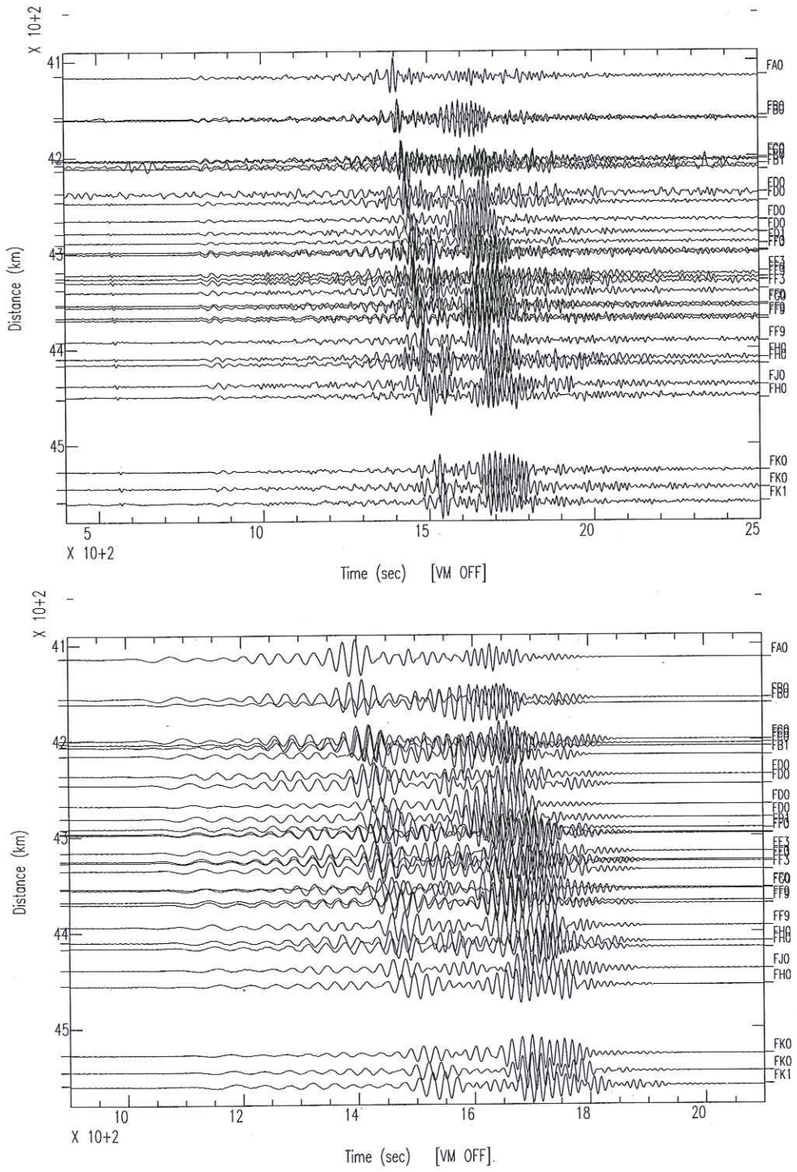

FIG. 2.7 – *Section de sismogrammes pour le séisme du 11 février 1999 (Mw=6,0 d=39°): haut avant filtrage temps-fréquence; bas après filtrage (tous les signaux sont filtrés entre 12 et 200 secondes de période.*

de permettre l'utilisation de séismes lointains, ou téléséismes, pour lesquelles les signaux d'ondes de surface sont bien dispersés en temps et bien séparés des ondes de volume.

La façon classique de procéder est de mesurer la phase de l'interspectre de deux signaux. Cette méthode est simple mais peut présenter des instabilités s'il y a des trous dans le spectre ou si la phase du signal présente des oscillations en raison d'interférences entre plusieurs ondes. Pour stabiliser notre mesure nous utilisons le filtre de Wiener [Wiener, 1949] et nous sélectionnons les points en fréquence d'après leur rapport signal sur bruit dans chacune des traces et leur cohérence (voir équation (2.14)).

Pour chaque couple de stations l'interspectre S entre les deux signaux $x(t)$ et $y(t)$ est donné par:

$$S_{xy}(\nu) = X(\nu)\, Y^*(\nu) \tag{2.8}$$

$X(\nu)$ et $Y(\nu)$ sont les transformées de Fourier des deux signaux, * représente le complexe conjugué, ν est la fréquence.

Après transformée de Fourier inverse l'intercorrélation Γ_{xy} est apodisée par une fenêtre de Hanning en temps $han(t)$ centrée sur son maximum t_0

$$\Gamma_{xy}(t)\ han(t-t_0) = TFI\left\{S_{xy}(\nu)\right\}\ \frac{1}{2}\left[1+\cos\left(\frac{2\pi(t-t_0)}{n_t}\right)\right]^n \tag{2.9}$$

TFI représente la transformée de Fourier inverse. Une apodisation en temps équivaut à un lissage en fréquence, l'interspectre lissé est alors une estimation de la densité spectrale d'interaction γ_{xy} des deux signaux considérés:

$$\widehat{\gamma}_{xy}(\nu) = TF\left\{\Gamma_{xy}(t)\ han(t-t_0)\right\} \tag{2.10}$$

$$= S_{xy}(\nu) * Han(\nu) e^{i\omega t_0} \tag{2.11}$$

$Han(\nu)$ est la transformée de Fourier de la fenêtre de Hanning.

Le filtre de Wiener W est le rapport entre la densité spectrale d'interaction des deux signaux et la densité spectrale de l'un d'eux.

$$W(f) = \frac{\widehat{\gamma}_{xy}(\nu)}{\widehat{\gamma}_{xx}(\nu) + A} \tag{2.12}$$

La densité spectrale d'un signal $\widehat{\gamma}_{xx}(\nu)$ est calculée comme la densité spectrale d'interaction $\widehat{\gamma}_{xy}(\nu)$ en prenant deux fois le même signal et $t_0 = 0$. La constante A est un seuil d'énergie utilisé pour stabiliser la mesure, dans notre cas nous lui avons préféré une sélection sur la cohérence des signaux et nous avons pris $A = 0$.

La phase du filtre de Wiener $\Phi_W(\nu)$ est convertie en temps de propagation de l'onde entre les deux stations $\Delta t(\nu)$:

$$\Delta t(\nu) = \frac{\Phi_W(\nu) + 2\pi N}{2\pi\nu} \tag{2.13}$$

N est le nombre de cycles qu'il faut ajouter à la phase pour la dérouler.

Le coefficient de cohérence entre les deux signaux est ensuite calculé par:

$$C(\nu) = \frac{\widehat{\gamma}_{xy}(\nu)}{\sqrt{\widehat{\gamma}_{xx}(\nu)\widehat{\gamma}_{yy}(\nu)}} \tag{2.14}$$

Il mesure la ressemblance entre les signaux et donc la validité de la mesure de déphasage.

La procédure de déroulage de la phase que nous avons utilisée pour obtenir nos données finales est itérative.

Calcul initial de la phase:

- La fonction phase est lue en partant des longues périodes et pour chaque saut supérieur à π entre deux points successifs un cycle (2π) est ajouté.
- Cette mesure de phase est interprétée en terme de temps d'arrivée puis l'ensemble des mesures pour un événement est inversé pour obtenir une courbe de dispersion par une méthode de réseau [Pedersen *et al.*, 2003]. Selon la qualité des sismogrammes la courbe de dispersion obtenue peut montrer des instabilités autour de fréquences où le rapport signal sur bruit est faible. Les vitesses obtenues pour certains événements peuvent être aberrantes car l'ensemble de la courbe de dispersion peut dans certains cas être faux de $n \cdot 2\pi$. La moyenne des courbes de dispersion pour tous les événements donne donc une première courbe de vitesse de phase pour la région qu'il faudra corriger après correction

des mesures aberrantes.

Phase itérative: un nouveau déroulage de la phase est effectué comme à la première étape, avec une vérification supplémentaire à partir de la courbe de dispersion moyenne obtenue précédemment:

- Pour chaque point en fréquence nous calculons la phase théorique correspondant à une onde plane arrivant depuis un back-azimut donné (celui du grand cercle entre la source et le centre du réseau de stations) à la vitesse *a priori* donnée par la courbe de dispersion.
- Nous ajoutons ou enlevons le nombre de cycles nécessaires pour obtenir la phase la plus proche de la valeur théorique.
- Une nouvelle courbe de dispersion moyenne est calculée, elle permet une nouvelle estimation des mesures de phase.

Ces étapes sont répétées jusqu'à ce que la nouvelle courbe de dispersion moyenne n'entraîne plus de modification sur les mesures de phase.

Sélections et moyennes: *a posteriori* nous selectionnons les points correspondants aux mesures de meilleure qualité afin de stabiliser les mesures.

- Pour chaque signal, les points en fréquence ayant un rapport signal sur bruit inférieur à 4 sont éliminés.
- Seuls sont pris en compte les délais pour lesquels la cohérence entre les deux signaux est supérieure à $0,95$ (équation (2.14)).
- 20 fréquence sont choisies pour échantillonner la partie résolue du spectre entre 10,5 et 190 secondes de période. La mesure de délai pour chacune de ces fréquences f0 est une moyenne pondérée des points situés dans un intervalle de plus ou moins 5% autour de f0 (figure 2.8).
- La procédure d'inversion des temps de propagation des ondes de surface que nous avons développée [chapitre 3 et Bruneton *et al.*, 2002] utilise en chaque station un temps calculé par rapport à une station

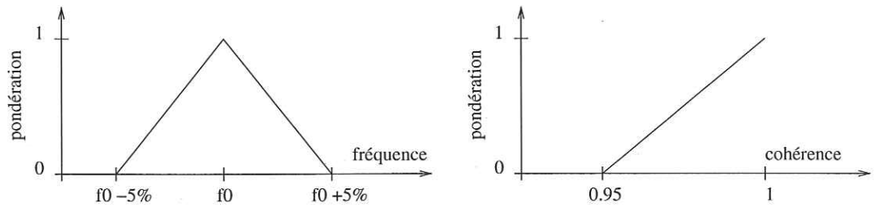

FIG. 2.8 – *Pondérations utilisées pour la moyenne donnant la mesure du délai pour une fréquence f0. La pondération de chaque point est le produit de la pondération fonction de la fréquence et de celle fonction de la cohérence.*

de référence. Pour ne pas dépendre trop fortement du choix de la station de référence R nous utilisons pour chaque mesure une moyenne de toutes les estimations possibles du temps de propagation entre la station de référence et la station S considérée. La première estimation est la mesure de délai en temps entre les stations R et S. Si n stations ont des mesures cohérentes pour le séisme et la fréquence considérés, $n-2$ autres estimations peuvent être faites en additionnant les délais mesurés entre la station R et une autre station S' (différente de S) et entre les stations S' et S. Sur les $n-1$ mesures obtenues nous en éliminons un quart par une procédure de comparaison avec la moyenne, élimination de la donnée la plus éloignée, nouvelle mesure de la moyenne, ... La mesure finale conservée est la moyenne des estimations restantes.

2.2.3 Inversion des courbes de dispersion

A partir des temps de phase mesurés sur les ondes de surface, nous pouvons obtenir des informations sur la courbe de dispersion du milieu dans lequel se propage l'onde. Le chapitre 3 décrit la méthode que nous avons développée pour calculer les vitesses de phase dans le réseau de stations. Cette information sur la dispersion des ondes de surface n'est qu'une étape vers la connaissance du milieu

en termes plus physiques: une inversion permet ensuite d'obtenir la valeur de la vitesse des ondes S en fonction de la profondeur.

Diverses méthodes existent pour réaliser l'inversion d'une courbe de dispersion (par exemple les méthodes linéarisées du type de celle utilisée dans le logiciel de Herrmann [1987], ou les inversions semi-globale non-linéaire de Shapiro *et al.* [1997] ou Yoshizawa & Kennett [2002]). Nous avons choisi de suivre une méthode linéarisée dont la paramétrisation permet de considérer à la fois des couches distinctes pour modéliser la croûte et un milieu continu dans le manteau. Cette méthode découle des travaux de Maupin & Cara [1992] et Lévêque *et al.* [1991].

Ce problème est largement sous-déterminé dans un cas réel. De nombreuses possibilités existent pour lever cette indétermination. Shapiro *et al.* [1997]) ont choisi de calculer un grand nombre de solutions puis de considérer un modèle moyen. Lomax & Snieder [1995] utilisent un algorithme génétique, Yoshizawa & Kennett [2002] une inversion semi-global («neighbourhood algorithm»). Le logiciel de Herrmann [1987] considère un modèle stratifié simple formé de peu de couches. Pour obtenir une image réaliste nous avons choisi de lisser le modèle de vitesse en fonction de la profondeur.

L'algorithme d'inversion est celui de Tarantola & Valette [1982], programmé pour minimiser les différences entre la courbe de dispersion théorique et celle obtenue à partir des données. A partir d'un modèle $\mathbf{m}_0$ de vitesse des ondes S en fonction de la profondeur, le modèle final $\mathbf{m}$ est obtenu par l'équation (2.15) en une itération. Des itérations supplémentaires n'amènent pas d'amélioration notable de la solution en terme de différences entre les courbes de dispersion.

$$\mathbf{m} = \mathbf{m}_0 + \mathbf{C}_{\mathbf{m}_0}\mathbf{A}^T(\mathbf{C}_{\mathbf{d}_0} + \mathbf{A}\mathbf{C}_{\mathbf{m}_0}\mathbf{A}^T)^{-1}[\mathbf{d}_0 - \mathbf{d}_\mathbf{m}] \tag{2.15}$$

$\mathbf{m}_0$ joue à la fois le rôle de modèle initial et de modèle *a priori*, $\mathbf{d}_0$ est le vecteur contenant la courbe de dispersion des données, $\mathbf{d}_0$ contient la dispersion théorique prédite par le modèle $\mathbf{m}_0$, la matrice $\mathbf{A}$ contient les dérivées partielles par rapport aux paramètres du modèle, et $\mathbf{C}_{\mathbf{d}_0}$ et $\mathbf{C}_{\mathbf{m}_0}$ contiennent les covariances *a priori*

respectivement des données et des paramètres du modèle. Pour le calcul de la courbe de dispersion et des dérivées partielles du modèle $\mathbf{m}_0$ les programmes de Saito [1988] sont utilisés.

La matrice de covariance des données est directement importée de l'étape précédente. Pour la matrice de covariance du modèle, suivant l'approche de Lévêque *et al.* [1991], nous considérons des fonctions de corrélation gaussiennes de largeur définie pour chaque inversion par une longueur de corrélation égale à la demi-largeur pour un intervalle de confiance de 60%. C'est-à-dire qu'il y aura un lissage de la solution avec la profondeur sur une distance liée à la longueur de corrélation. L'écart-type *a priori* du modèle en vitesse des ondes S est fixé à 4% de la vitesse. Il gouverne l'écart qui va être permis en chaque point entre $\mathbf{m}$ et $\mathbf{m}_0$. Les paramètres des différentes couches crustales sont découplés les uns des autres et des paramètres du manteau.

2.2.4 Prise en compte de l'atténuation

La Terre n'est pas un matériel parfaitement élastique, les contraintes et déformations subies par le milieu au passage d'une onde peuvent avoir des effets irréversibles sur la structure cristalline et les limites entre les grains. Ces effets anélastiques sont résumés dans un paramètre sans dimension, le facteur de qualité Q [voir par exemple les chapitres 5.5 et 7.3.4 de Aki & Richards, 2002].

En conséquence de cette anélasticité, la vitesse de propagation d'une onde dans un milieu donné va dépendre de son contenu fréquentiel. En particulier, un modèle de vitesse obtenu à partir d'ondes de surface de périodes comprises entre 10 et 190 secondes n'est pas directement comparable avec un modèle construit avec des ondes de volume de fréquence proche de 1 Hz.

Pour pouvoir comparer nos résultats avec, par exemple, des modèles de Terre standards nous devons les corriger de ce phénomène. Dans les équations élastodynamiques l'atténuation peut être prise en compte par un nombre d'onde k ou

une vitesse de phase c complexes. Nous disposons d'un programme d'inversion des courbes de dispersion pouvant à la demande prendre en compte cette atténuation [Herrmann, 1987], mais ce logiciel modélise les modèles de vitesse par des milieux stratifiés plans. Nous lui avons préféré un autre programme qui permet de considérer des milieux lisses mais qui ne tient pas compte de l'atténuation [Lévêque *et al.*, 1991; Maupin & Cara, 1992]. Les programmes de Herrmann [1987] nous ont permis d'estimer les différences introduites par l'atténuation (de l'ordre de 1% en vitesse des ondes S) et de montrer qu'une correction *a posteriori* est possible. En effet, pour des valeurs de Q élevées, les dérivées des vitesses de phase par rapport aux vitesses des ondes S dans chaque couche sont très peu modifiées par la partie complexe de la vitesse de phase.

Pour cette correction nous utilisons un modèle $Q(z)$ indépendant de la fréquence, simplifié d'après le modèle PREM [Dziewonski & Anderson, 1981]. Les vitesses d'onde S qui seront présentées dans cet ouvrage sont corrigées de l'atténuation pour une fréquence de référence de 1 Hz, suivant l'équation:

$$V_S^{1Hz}(z) = V_S(z) \left[1 + \frac{1}{\pi Q(z)} \ln\left(\frac{1}{\nu(z)}\right)\right] \tag{2.16}$$

Pour chaque profondeur z, nous devons chercher la fréquence représentative de la profondeur échantillonnée $\nu(z)$. La courbe de dispersion moyenne calculée pour la région est $c(\nu)$. On peut en déduire directement $\lambda(\nu)$ et $\nu(\lambda)$, λ étant la longueur d'onde. La meilleure correspondance entre le modèle avec atténuation et le modèle corrigé *a posteriori* issus des programmes de Herrmann [1987], est obtenue en posant ensuite $z = \lambda/4$ et donc $\nu(\lambda) = \nu(4z)$.

Bibliographie

Aki, K. & P. G. Richards, 2002. *Quantitative seismology*, second edition, University Science Books, Sausalito, California.

Baumont, D., 1999. *Caractérisation sismologique de la structure lithosphérique des Andes Centrales (17°-20°)*, thèse de doctorat, Université Joseph Fourier, Grenoble.

Bruneton, M., V. Farra, H. A. Pedersen & the SVEKALAPKO Seismic Tomography Working Group, 2002. Non-linear surface wave phase velocity inversion based on ray theory, *Geophys. J. Int.*, **151**, 583–596.

Coulomb J. & G. Jobert (eds.), 1972. *Traité de géophysique interne, tome 1: sismologie et pesanteur*, Masson & C^{ie}, Paris.

Dziewonski, A. M. & D. L. Anderson, 1981. Preliminary reference Earth model, *Phys. Earth Planet. Int.*, **25**, 297–356.

Herrin, E. & T. Goforth, 1977. Phase-matched filters: application to the study of Rayleigh waves, *Bull. Seism. Soc. Am.*, **67**, 1259–1275.

Herrmann, R. B., 1987. *Computer Programs in seismology, Volume IV: Surface waves inversion*, Saint Louis University, Missouri.

Keilis-Borok, V. I. (ed.), 1989. *Seismic surface waves in laterally inhomogeneous Earth*, Kluwer Academic Publishers, Dordrecht.

Lander, A. V. & A. L. Levshin, 1989. Recording, identification, and measurement of surface wave parameters, in *Seismic surface waves in laterally inhomogeneous Earth*, V. I. Keilis-Borok (ed.), Kluwer Academic Publishers, Dordrecht, 131–182.

Lévêque, J.-J., M. Cara & D. Rouland, 1991. Waveform inversion of surface wave data: test of a new tool for systematic investigation of upper mantle structures, *Geophys. J. Int.*, **104**, 565–581.

Lomax, A. & R. Snieder, 1995. The contrast in upper mantle shear-wave velocity between the East European Platform and Tectonic Europe obtained with genetic algorithm inversion of Rayleigh wave group dispersion, *Geophys. J. Int.*, **123**, 169–182.

Maupin, V. & M. Cara, 1992. Love-Rayleigh wave incompatibility and possible deep upper mantle anisotropy in Iberian Peninsula, *Pure app. Geophys.*, *138*, 429–444.

Olivier, J., 1962. A summary of observed seismic surface wave dispersion, *Bull. Seism. Soc. Am.*, **52**, 81–86.

Pedersen H. A., O. Coutant, A. Deschamps & M. Soulage, 2003. An improved algorithm for measuring surface wave phase velocities beneath a small broad-band array. Application to the French Alps, *Geophys. J. Int.*, sous presse.

Saito, M., 1988. Disper 80: a subroutine package for the calculation of seismic modes solutions, in *Seismological Algorithms*, D. J. Doornbos (ed.), Academic Press, New-York.

Shapiro, N. M., M. Campillo, A. Paul, S. K. Singh, D. Jongmans & F. J. Sánchez-Sesma, 1997. Surface-wave propagation across the Mexican Volcanic Belt and the origin of the long-period seismic-wave amplification in the valley of Mexico, *Geophys. J. Int.*, **128**, 151–166.

Tarantola, A. & B. Valette, 1982. Generalized nonlinear inverse problems solved using the least square criterion, *Rev. Geophys. Space Phys.*, **20**, 219–232.

Wiener, N., 1949. *Time series*, M.I.T. Press, Cambridge, Massachusetts.

Yoshizawa, K. & B. L. N. Kennett, 2002. Non-linear waveform inversion for surface waves with a neighbourhood algirithm – application to multimode dispersion measurements, *Geophys. J. Int.*, **149**, 118–133.

Chapitre 3

Tomographie en ondes de surface

Pour obtenir un modèle tridimensionnel en vitesse des ondes S à partir des sismogrammes de l'expérience SVEKALAPKO, nous avons choisi de suivre une procédure en deux temps. La première étape consiste à inverser les temps d'arrivées d'ondes de surface pour chaque mode (c'est à dire chaque type d'onde et chaque fréquence) de façon à obtenir des cartes de vitesse de phase. Pour cette inversion j'ai développé en collaboration avec Véronique Farra une technique basée sur le tracé de rais en deux dimensions. Dans un deuxième temps la superposition de ces cartes de vitesse de phase donne une courbe de dispersion pour chaque nœud de la grille. Chacune de ces courbes de dispersion est inversée pour obtenir un profil de vitesse des ondes S en fonction de la profondeur. Cette deuxième étape est effectuée par la méthode décrite au paragraphe 2.2.3. L'ensemble de ces profils forme alors notre modèle tridimensionnel. Dans ce chapitre nous verrons d'abord quelques généralités sur la théorie des rais qui est à la base de notre nouvelle méthode. Une deuxième partie décrit ensuite les détails de notre technique d'inversion.

3.1 Généralités sur la théorie des rais

La théorie des rais est une méthode locale et rapide qui explique en termes physiques simples une partie importante du signal sismique. De nombreux modèles classiques de Terre comme la table de Jeffreys & Bullen [1940] ont été obtenus essentiellement par la théorie des rais. Elle est aujourd'hui largement utilisée en sismologie dans les méthodes de tomographie en temps de parcours [voir par exemple, Aki *et al.*, 1977; Nolet, 1987], dans la localisation des séismes, la détermination des mécanismes au foyer, l'interprétation des données sismiques (base entre autre de l'exploration pétrolière [Nur, 1987]), ou dans l'interprétation des ondes de surface avec les rais de surface [Jobert & Jobert, 1987].

3.1.1 Théorie

Les équations de la théorie des rais correspondent à une solution asymptotique à haute fréquence de l'équation des ondes en milieu élastique. Elles décomposent le champ d'onde en contributions élémentaires qui se propagent le long des rais, chaque onde élémentaire est traitée indépendamment. Elle permet de calculer explicitement un certain nombre d'observables que l'on peut mesurer plus ou moins directement sur des données tels que le temps de trajet, la polarisation ou l'amplitude de l'onde. C'est donc un outil particulièrement adapté à l'interprétation et à l'inversion de données.

Une onde élémentaire est décrite par sa phase ωT, également appelée eikonal (ω étant la pulsation ou fréquence circulaire et T le temps de parcours) et par un vecteur amplitude complexe $\mathbf{A}$. Les solutions de l'équation des ondes sont recherchées sous la forme:

$$\mathbf{u}(\mathbf{x},\omega) = \mathbf{A}(\mathbf{x},\omega)\mathbf{e}^{\mathbf{i}\omega\mathbf{T}(\mathbf{x})} \tag{3.1}$$

où $\mathbf{u}$ est un déplacement et $\mathbf{x}$ est le vecteur position en trois dimensions. L'approximation asymptotique à haute fréquence consiste à chercher $\mathbf{A}(\mathbf{x},\omega)$ sous la

forme

$$\mathbf{A}(\mathbf{x},\omega) = \sum_{j=0}^{\infty} \frac{\mathbf{A}_j(\mathbf{x})}{(-i\omega)^j} \tag{3.2}$$

C'est-à-dire en séparant les variables d'espace et de fréquence.

En introduisant les équations 3.1-3.2 dans l'équation d'onde on obtient à l'ordre zéro en ω^{-1} l'équation eikonal:

$$(\nabla T)^2 = u^2(\mathbf{x}) \tag{3.3}$$

où u est la lenteur du milieu, égale à $1/\alpha$ pour une onde P et $1/\beta$ pour une onde S.

Cette équation appartient à la classe des équations non-linéaires aux dérivées partielles du premier ordre appelées équations d'Hamilton-Jacobi. Elle peut s'écrire sous la forme

$$H(\mathbf{x},\nabla T) = 0 \tag{3.4}$$

et être résolue par la méthode des caractéristiques [Courant & Hilbert, 1966]. En sismologie, les caractéristiques sont les rais, définis par leur vecteur canonique $(\mathbf{x}(\tau),\mathbf{p}(\tau))$. $\mathbf{x}(\tau)$ est la position, $\mathbf{p}(\tau) = \nabla T$ est le vecteur lenteur du rai à la position $\mathbf{x}(\tau)$ et τ est un paramètre d'avancement le long du rai. τ dépend de la forme choisie pour l'hamiltonien H, il peut être par exemple une abscisse curviligne ou un temps de trajet.

La formulation hamiltonienne de l'équation eikonal débouche sur le système des équations canoniques

$$\begin{aligned} \dot{\mathbf{x}} &= \frac{d\mathbf{x}}{d\tau} = \frac{\partial H}{\partial \mathbf{p}} \\ \dot{\mathbf{p}} &= \frac{d\mathbf{p}}{d\tau} = -\frac{\partial H}{\partial \mathbf{x}} \end{aligned} \tag{3.5}$$

Le temps de trajet s'obtient ensuite par:

$$T = \int_{rai} \mathbf{p}\cdot\dot{\mathbf{x}}\, d\tau \tag{3.6}$$

En ajoutant des conditions aux limites, ces équations peuvent être résolues numériquement par des méthodes de perturbation comme la méthode des rais paraxiaux [Farra & Madariaga, 1987; Deschamps, 1972].

3.1.2 Application aux ondes de surface

La théorie des rais peut également s'appliquer à des ondes de surface se propageant le long de la surface d'un milieu élastique stratifié présentant de faibles variations latérales. La principale différence entre les ondes de volume à haute fréquence et les ondes de surface est que la vitesse de phase des dernières dépend de la fréquence. Les rais des ondes de surface seront donc tracés pour une valeur de la fréquence ω donnée car les rais sont différents pour chaque fréquence.

Pour un mode particulier d'onde de surface, les solutions vont être cherchées sous une forme proche de l'équation (3.1), pour laquelle le vecteur amplitude $\mathbf{A}$ est décomposé en deux parties U et $\mathbf{A}$. U est la fonction propre verticale locale qui correspond à un milieu stratifié plan ayant la structure locale de la position (x, y) le long de la surface libre. $\mathbf{A}$ est une amplitude complexe dépendant de la fréquence et de la position sur la surface libre.

$$\mathbf{u}(x, y, z, \omega) = \mathbf{A}(x, y, \omega)U(x, y, z, \omega)e^{i\omega T} \tag{3.7}$$

T est le temps de parcours. De la même façon que pour les ondes de volume, $\mathbf{A}$ va être cherché sous la forme d'une série asymptotique. Cette fois le développement ne se fait pas en fonction de la pulsation mais d'un petit paramètre sans dimension ϵ, représentant le fort lissage des variations latérales par rapport aux variations verticales de la structure [Levshin, 1989].

On obtient alors à l'ordre zéro en ϵ l'équation eikonal avec la vitesse de phase de l'onde considérée [pour plus de détail voir par exemple Tromp & Dahlen, 1992, 1993].

$$(\nabla T)^2 = c^{-2}(\mathbf{x}, \omega) \tag{3.8}$$

L'approche des rais peut ensuite être utilisée pour intégrer cette équation.

3.1.3 Domaine d'application

La théorie des rais est utilisée en deux ou trois dimensions, dans des milieux élastiques stratifiés. Chaque couche peut être hétérogène et/ou anisotrope. Les

interfaces qui séparent les strates peuvent être de forme quelconque [voir par exemple Farra, 1993]. La configuration du dispositif de sources et de récepteurs est arbitraire.

Pour respecter l'hypothèse de haute fréquence la longueur d'onde λ des ondes considérées doit être considérablement plus petite que les autres dimensions caractéristiques du problème

$$\lambda \ll l_1, l_2, l_3, ...l_n \tag{3.9}$$

l_j pouvant être par exemple le rayon de courbure d'une interface, la taille d'une hétérogénéité, l'épaisseur d'une couche [Červený *et al.*, 1977]. Dans le cas des ondes de surfaces ce sont les hétérogénéités latérales qui doivent être lisses, les variations du milieu avec la profondeur peuvent être au contraire très variables. Toutefois l'étude d'un certain nombre d'exemples montre que la théorie des rais peut rester valide même dans des situations où la longueur d'onde est du même ordre de grandeur que les longueurs caractéristiques (voir tests synthétiques ci-desous).

Dans notre étude nous considérons des ondes de longueur d'onde variant entre 35 et 900 km. L'ouverture du réseau SVEKALAPKO est de 500 km environ, les distances entre stations sont de 100 km. Nous sommes donc à la limite du domaine d'application de la théorie des rais. En conséquence notre étude a débuté par une série de tests sur sismogrammes synthétiques pour valider l'utilisation de cette théorie (chapitre 3.2.2). Ces sismogrammes sont calculés par la méthode indirecte d'éléments frontière [IBEM, Pedersen *et al.*, 1996], qui calcule le champ d'onde complet dans un milieu stratifié en 2,5 dimensions (onde incidente oblique par rapport à une structure bidimensionnelle, voir figure 3.1). Le milieu utilisé pour les tests est un modèle simplifié du Moho dans la région du projet SVEKALAPKO, composé d'une couche homogène sur un demi-espace. Ce milieu présente au niveau du Moho un contraste d'impédance beaucoup plus important que dans la réalité, les phénomènes de diffusion et diffraction induits par notre structure

test sont donc exagérés. Les résultats (figures 3.2 et 3.3) montrent que ce milieu est suffisamment lisse pour que des structures du même ordre de grandeur que la longueur d'onde soient correctement imagées. Dans nos calculs nous avons donc induit un lissage proportionnel à la longueur d'onde pour chaque période considérée (nous ne pouvons donc obtenir que la vitesse moyenne pour les plus basses fréquences).

La théorie des rais ne prend pas en compte les phénomènes de diffusion des ondes, ni le couplage qui peut exister entre différents modes. Elle présente également des instabilités en présence de caustiques ou dans les zones d'ombre. Des méthodes hybrides couplant la théorie des rais avec d'autres types d'approximations permettent d'étendre son champ d'application, par exemple l'approximation de Born-Rytov, des couplages avec les différences finies ou la méthode de Thomson-Haskell.

3.2 Inversion non-linéaire des ondes de surface

Article paru dans *Geophysical Journal International* (**151**) 583–596 (2002)

Non-linear surface wave phase velocity inversion based on ray theory

M. Bruneton[1], V. Farra[2], H. A. Pedersen[1] and the SVEKALAPKO Seismic Tomography Working Group

[1]Laboratoire de Géophysique Interne et Tectonophysique, Observatoire des Sciences de l'Univers de Grenoble, France.

[2]Département de Sismologie, Institut de Physique du Globe de Paris, France.

Résumé

Avec les développements de réseaux temporaires et permanents de sismomètres large-bande le besoin de techniques modernes pour l'interprétation des ondes de surface devient important. Nous présentons ici une nouvelle méthode, basée sur la théorie des rais paraxiaux en deux dimensions, pour inverser les temps d'arrivées d'ondes de surfaces télésismiques et construire des cartes de vitesse de phase à une échelle régionale. Pour valider l'utilisation de la théorie des rais à cette échelle sur des structures lisses nous avons utilisé des mesures locales de vitesses de phase et de directions de propagation d'ondes de Rayleigh, prises sur des sismogrammes synthétiques (obtenus en modélisant le champ d'onde complet). Dans notre inversion la courbure des fronts d'onde due à des hétérogénéités à l'extérieur de la zone d'étude est prise en compte. En effet le modèle utilisé dans l'inversion comprend la vitesse de phase du milieu et la forme des fronts d'onde incidents. Dans le tracé de rai direct la courbure des fronts d'onde est introduite dans les conditions aux limites en écrivant l'égalité entre le vecteur lenteur du rai et le gradient du temps d'arrivée de l'onde sur le bord de la zone d'étude. Pour contraindre l'inversion nous appliquons des critères de lissage sur le modèle de vitesse et sur les fronts d'onde. Des tests sur données synthétiques (calculées avec le tracé de rai direct et par modélisation du champ d'onde complet) montrent que pour un

écartement moyen de 100 km entre stations la plus petite structure résolue a une taille de 150 km. Des hétérogénéités de même taille que la longueur d'onde sont correctement reconstruites par l'inversion avec toutefois des variations de vitesse de phase légèrement sous-estimées en raison du lissage introduit par le champ d'onde. Un rapport signal sur bruit minimum de 3,5 est nécessaire pour obtenir une image correcte du champ de vitesses de phases. L'inversion d'une partie des données du projet SVEKALAPKO pour le mode fondamental de Rayleigh à 60 s de périodes montre l'applicabilité de la méthode sur des données réelles.

The development of temporary and permanent broadband seismic arrays reinforces the need for advanced interpretation techniques in surface wave analysis. We present a new method based on 2-D paraxial ray theory of inverting teleseismic surface wave phase information and constructing phase velocity maps on a regional scale. Measurements of local phase velocities and propagation directions of Rayleigh waves taken from full waveform synthetic seismograms are used to validate the ray theory for smooth structures on a regional scale. Curved wavefronts created by heterogeneous structure outside the study area are taken into account through joint inversion for the phase velocity field and the shape of the incoming wavefronts. In the forward ray tracing procedure, the curved wavefronts are introduced through the boundary conditions by equating the slowness vector of the ray at the edge of the study region with the known gradient of the arrival time of the wave. To make the inverse problem non-singular we constrain the parameters in the inversion primarily by applying a smoothness criteria on the velocity field and on the incoming wave-field. Inversions of synthetic data sets computed by direct ray tracing and by full waveform modeling show that for 100 km spacing between stations the minimum size of structure that we can image is approximately 150 km. Heterogeneities with a size approximately equal to the wavelength are reconstructed by the ray-based inversion even though velocity variations are underestimated due to the wave-field smoothing of the structures. A minimum

signal to noise ratio of 3.5 is necessary in order to correctly retrieve the phase velocity field. Inversion of a subset of the SVEKALAPKO data for 60 s period demonstrates the applicability of the method on real data.

3.2.1 Introduction

Fundamental mode surface waves of 10 to 100 s period provide information on the shear-velocity of the upper 200 km of the Earth. Such studies are useful to complement lithospheric models obtained using body-wave tomography as these models are mostly based on P-wave travel time inversion and are therefore sensitive to the P-velocity structure. S-wave tomography is difficult to conduct as low velocity zones, which are more pronounced in S than P-wave velocity, introduce non-linearity into the inversion. Surface waves therefore provide a more reliable means to retrieve the S-wave structure. P and surface wave tomographies are also complementary in terms of resolution as the former has very good lateral resolution and the latter better vertical resolution.

To date, inversions for lithospheric structures using surface waves on a regional scale have mostly been based either on the classical two-station method [see, for example, Calcagnile, 1991], or on network analysis. One alternative approach is to measure local phase velocities by analyzing data from small aperture arrays [Cotte *et al.*, 2000]. Larger scale arrays have been used for regional studies using various methods such as the 2-D group velocity ray-based tomography of Yanovskaya *et al.* [1998]. Several inversion methods are based on waveform modeling, for example the path-average approximation with modal summations [Nolet, 1990; Zielhuis & Nolet, 1994; Simons *et al.*, 1999], linearized scattering [Snieder, 1988a,b], mode coupling [Maupin, 1988; Marquering & Snieder, 1996; Marquering *et al.*, 1996] and multiple scattering using Born's approximation [Friederich & Wielandt, 1995; Friederich, 1998; Pollitz, 1999]. The last three cited studies have the advantage that the shapes of the incoming wave-fields need not be pla-

nar, so reducing artifacts due to non-planar wavefronts incident upon the array. However, they use the acoustic approximation and can be applied only to the vertical component of the seismograms, that is to the Rayleigh wave [Friederich *et al.*, 1993]. As van der Lee [1998] shows, one should be cautious in interpreting the entire waveform of a seismogram in terms of heterogeneities along the propagation path. Amplitude anomalies of intermediate-period fundamental-mode Rayleigh waves are dominated by earthquake source parameters and heterogeneous structures near the source, unlike phase anomalies which mostly depend on the structure along the wave path. Yanovskaya [1996] proposes a tomographic method based on inversion of azimuthal anomalies measured from polarization analysis, while still remaining within the framework of geometrical ray theory.

The aim of the present study is to invert the data set recorded during the SVEKALAPKO deep seismic experiment [Bock & SVEKALAPKO Seismic Tomography W. G., 2001], to determine the lithospheric structure of the Baltic Shield and its lateral variations beneath Finland. Improved knowledge of this structure should advance our understanding of plate-tectonic processes in the early history of the Earth, as it contains traces of a 1.9 Ga collision [for a summary of the geology and tectonic features of the Fennoscandian Shield, see for example Korja *et al.*, 1993].

The lateral lithospheric heterogeneities in the Fennoscandian Shield are generally considered to be smooth. Several deep seismic sounding profiles have been carried out in the region [Luosto, 1997], revealing in particular an anomalously deep Moho at approximately 60 km depth under the eastern part of the Ladoga-Bothnian Bay zone, which is also associated with very high seismic velocities in the lower crust. The lithosphere has been shown to be at least 170 km thick beneath the area [Babuška *et al.*, 1988; Calcagnile, 1991].

To obtain 2-D phase velocity maps of the individual Rayleigh and Love modes, we adapted the paraxial ray tracing method developed by Farra [1990, 1993]. The use of ray theory limits us to smoothly varying structures as mode coupling is not

taken into account. We extend Farra's method to take into account non-planar incoming wave-fields and simultaneously invert for the phase velocity field and the shape of the incident wavefronts. In the first part of the paper, we demonstrate the validity of ray theory for surface wave propagation in smooth regional structures – local propagation directions and velocities are calculated from synthetic seismograms computed using the Indirect Boundary Element Method (IBEM) for multi-layered media [Pedersen *et al.*, 1996], and compared with the results expected from ray theory. We then define the ray tracing procedure and the inversion method we use to invert for the phase velocity field. Finally, we present numerical examples from inversion of synthetic data sets computed by ray tracing and IBEM, as well as a preliminary inversion of a subset of the SVEKALAPKO data.

3.2.2 Applicability of ray theory

A major drawback to the use of ray theory is that it derives from a high frequency approximation and therefore does not take into account heterogeneities smaller than the wavelength of the incident wave. In this section, we justify the use of ray theory to obtain 2-D velocity maps of structures of the type encountered beneath SVEKALAPKO through analysis of full waveform synthetic seismograms. To compute the synthetic seismograms, we use a 2-D structure composed of a single layer (the crust) over a half space (the mantle). The model shown in Fig. 3.1 is a simplified north-south cross-section of the Moho depth map obtained by Luosto [1990] from a compilation of seismic profiles in Fennoscandia. The thickness of the crust varies smoothly from 44 km to 60 km in the central part of the region, in an area 350 km wide. On each side of the trough, the crust thins out to 43 km over a distance of 100 km. In this model, we propagate a plane Rayleigh wave with a backazimuth of 60 degrees (that is, coming from approximately the north-east). Synthetic seismograms are computed using the Indirect Boundary

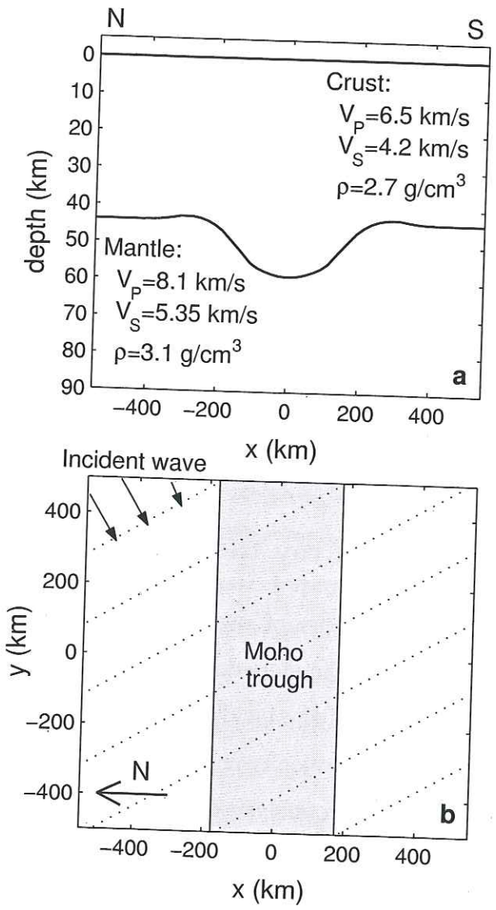

FIG. 3.1 – *Two-dimensional crustal model used to compute synthetic seismograms by the Indirect Boundary Elements Method. a) North-South cross section; b) map view of the propagating surface wave, black arrows give the initial direction of the wave, dotted lines are successive wavefronts.*

Element Method (IBEM) developed by Sánchez-Sesma & Campillo, and extended to 2.5-D multi-layered media [Pedersen *et al.*, 1996]. IBEM solves the full wave equation so multiple scattering and all coupling effects between waves are taken into account. Even though lateral variations in the model are smooth, they are distributed over distances comparable to a wavelength (varying between 40 and 460 km in the 10-100 s period interval).

Comparison of measured and predicted phase velocities

We compute seismograms for a receiver geometry similar to that of the SVEKALAPKO experiment, that is, a regular grid with 90 km between pairs of adjacent stations. The time delays between pairs of traces are computed in two steps. The first step consists of finding the best fitting dispersion curve for all the data from one event using the slant-stack method developed by McMechan & Yedlin [1981] by computing the image of the wave-fields in the (p, ω) plane, where p is the slowness and ω the frequency. The maximum amplitudes at each frequency define the best fitting phase velocity curve. We correct the synthetic seismograms for this dispersion, and then compute the remaining small time delays for each pair of traces using Wiener filtering. Only frequencies with high coherency (> 0.95) are considered. To obtain the total delay between the original seismograms we add the delays computed at each of the two steps. The phase velocity between each neighbouring station pair is calculated as the inverse of the gradient of the time delay.

Fig. 3.2 displays the phase velocity curves obtained for periods of 25 and 67 s (approximately 100 and 300 km wavelength) along different profiles perpendicular to the structure. They are compared to the theoretical phase velocities calculated assuming for every point a horizontally stratified medium with the properties of the model immediately below the point, using the software published by Herrmann [1985]. At 25 s period as well as at 67 s, the measured phase

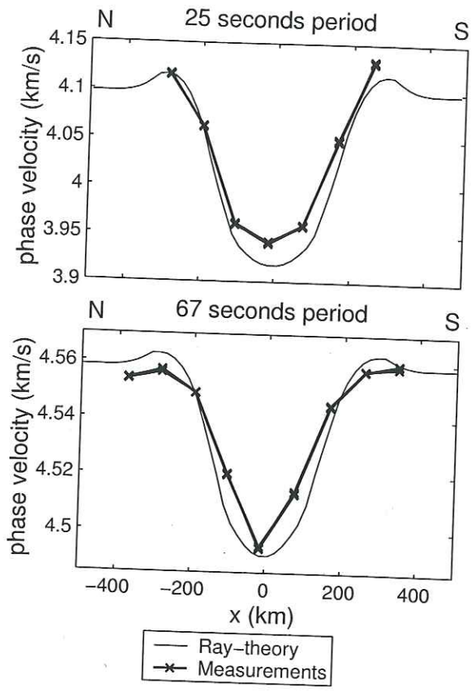

FIG. 3.2 – *Phase velocities obtained from synthetic seismograms computed with IBEM, on the structure of Fig. 3.1.*

velocities correctly display the geometry of the structure. However, the structure is smoothed: the minimum velocity is slightly larger than predicted by theory. For the longest wavelength (300 km), the structure is also simplified and the small bumps on either side of the trough are not resolved. At 25 s period, velocities slightly higher than theoretically predicted appear immediately down-stream the structure, possibly due to the interaction of the primary Rayleigh wave with Rayleigh-Love-Rayleigh converted waves.

Comparison of measured and predicted propagation directions

We also measured the propagation direction of the wave on the synthetic seismograms. The backazimuth angle is measured using the array analysis developed by Cotte *et al.* [2000] following the work of Barker *et al.* [1996] and Poupinet *et al.* [1984]. For each measurement, we use a dense array of 5 × 5 stations, with 3 km between neighbouring station pairs.

Fig. 3.3 displays the measured backazimuth in six frequency bands. On each graph, the propagation angles given by Snell's law for the lowest and highest predicted phase velocities within the frequency interval are also displayed.

The measured backazimuth is in close agreement with the theoretical deviation in all frequency bands. The largest difference between measured and theoretical values is half a degree and appears for the higher frequencies in waves that have crossed the heterogeneous structure. As expected, the structure is smoothed at long periods where the heterogeneity scale is small as compared to the wavelength.

The part of the structure where the Moho becomes shallower is detected at all frequencies, but displaced by a few kilometers from its real position, probably due to the interaction of the incoming waves with those reflected from this interface. Not withstanding these small differences, ray theory seems to provide a good approximation to the behaviour of Rayleigh waves propagating across a smooth structure, even though the variation takes place over distances of the order of the wavelength.

3.2.3 Ray tracing formulation

Our aim is to obtain the regional distribution of phase velocity as a function of frequency by inverting time delays of surface waves measured on a 2-D network of receivers, repeated for each wave mode. We first need a formulation of the forward problem: how to compute the arrival times of the wave at every receiver. We assume that we know the phase velocity at a given frequency throughout

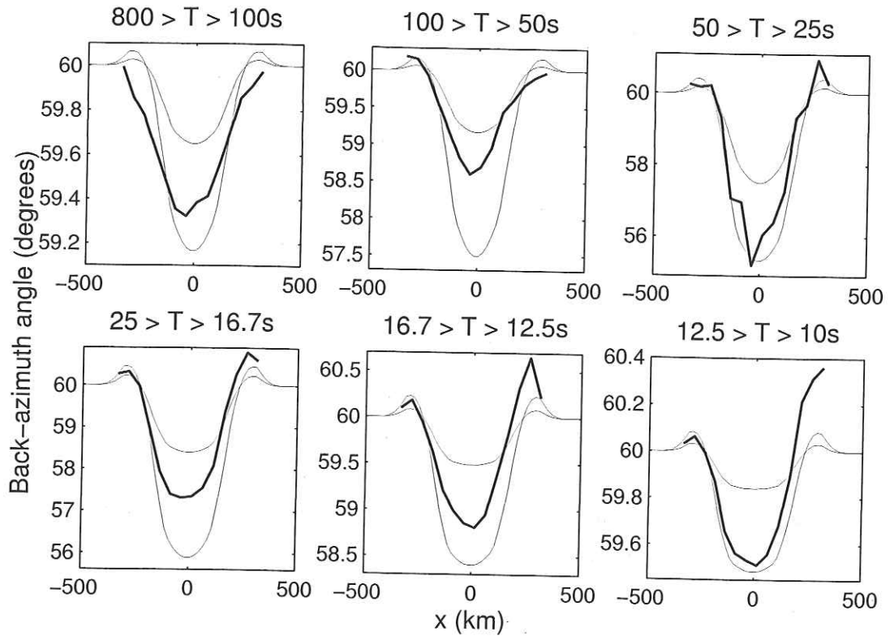

FIG. 3.3 – *Measured propagation angle on synthetic seismograms across the two-dimensional structure of Fig. 3.1. The period interval is given above each plot, thin lines are the extreme values within each period interval according to ray theory. Note that the backazimuth scale is different in each plot.*

a rectangular region containing the 2-D network of receivers. We then suppose that a surface wave is incident upon this region. Surface waves are known to be generally non-planar [Friederich *et al.*, 1994; Friederich, 1998], so we characterize the wavefront by its arrival time at the boundary of the model. The corresponding rays going from the edge of the box to every receiver have to be traced in order to compute the arrival times at the receivers.

The ray tracing method used here is derived from Farra & Madariaga [1987] and Farra [1990]. In section 3.2.3 we briefly present this method of paraxial ray tracing, and in section 3.2.3 we present the theory necessary for its extension

to the geometrical setup used here, that is, stations inside the study region and non-planar incoming waves.

Paraxial ray tracing

The high frequency approximation of the wave equation leads to the eikonal equation:

$$(\nabla_{\mathbf{x}} T)^2 = c^{-2} = u^2 \tag{3.10}$$

where T is the arrival time, c the phase velocity, u the slowness, and $\nabla_{\mathbf{x}}$ the gradient in the horizontal plane. Equation (3.10) belongs to the family of Hamilton-Jacobi equations $H(\mathbf{x}, \mathbf{p}, \tau) = 0$ [Červený, 1989]. The Hamiltonian H is a function of position $\mathbf{x}$, slowness vector $\mathbf{p} = \nabla_{\mathbf{x}} T$, and sampling parameter τ along the ray. As the problem is two-dimensional, $\mathbf{x} = (x_1, x_2)$ and $\mathbf{p} = (p_1, p_2)$. The Hamiltonian may take many different forms [Červený, 1989] and we choose here that used by Farra [1990]:

$$H(\mathbf{x}, \mathbf{p}, \tau) = \frac{1}{2}\left(\mathbf{p}^2 - u^2(\mathbf{x})\right) \tag{3.11}$$

The corresponding sampling parameter τ has units $\mathrm{km^2 s^{-1}}$ and is related to travel time by $dT = u^2 d\tau$. This parameter is chosen instead of the more commonly used travel time (in s) or arclength (in km) because the elements of the Hamiltonian are separated, depending on slowness and position, which simplifies the computation of the derivatives [Farra, 1993].

The Method of Characteristics [Courant & Hilbert, 1966] is used to solve the eikonal equation. The rays, described in terms of position $\mathbf{x}(\tau)$ and slowness vector $\mathbf{p}(\tau)$ satisfy the canonical equations:

$$\begin{aligned} \dot{\mathbf{x}} &= \nabla_{\mathbf{p}} H = \mathbf{p} \\ \dot{\mathbf{p}} &= -\nabla_{\mathbf{x}} H = \frac{1}{2}\nabla_{\mathbf{x}} u^2 \end{aligned} \tag{3.12}$$

where dot means derivative with respect to τ and $\nabla_{\mathbf{p}}$ is the gradient with respect to the slowness vector.

Suppose that a ray has been traced in the known medium using equation (3.12). Around this ray, called the central ray, we can obtain neighbouring rays by means of first order perturbation theory. Paraxial rays deviate from the reference ray by small perturbations in position ($\mathbf{x} = \mathbf{x_0} + \delta\mathbf{x}$) and slowness vector ($\mathbf{p} = \mathbf{p_0} + \delta\mathbf{p}$). The perturbations of position and slowness satisfy the paraxial ray tracing equations deduced from (3.12):

$$\begin{aligned} \delta\dot{\mathbf{x}} &= \nabla_{\mathbf{x}}\nabla_{\mathbf{p}}H\,\delta\mathbf{x} + \nabla_{\mathbf{p}}\nabla_{\mathbf{p}}H\,\delta\mathbf{p} = \delta\mathbf{p} \\ \delta\dot{\mathbf{p}} &= -\nabla_{\mathbf{x}}\nabla_{\mathbf{x}}H\,\delta\mathbf{x} - \nabla_{\mathbf{p}}\nabla_{\mathbf{x}}H\,\delta\mathbf{p} = \mathbf{U}\,\delta\mathbf{x} \end{aligned} \tag{3.13}$$

where $\mathbf{U}$ is a 2×2 matrix whose elements $\mathbf{U}_{ij} = \frac{1}{2}\frac{\partial^2 u^2}{\partial x_i\,\partial x_j}$ are calculated along the reference ray.

The paraxial propagator of system (3.13) is used to compute the evolution of $\delta\mathbf{x}$ and $\delta\mathbf{p}$ along the ray.

The rays that are solution of equation (3.13) also have to satisfy another relation derived from the perturbation of the eikonal equation (3.11):

$$\delta H(\tau) = \nabla_{\mathbf{p}}H \cdot \delta\mathbf{p} + \nabla_{\mathbf{x}}H \cdot \delta\mathbf{x} = 0 \tag{3.14}$$

where the partial derivatives of H are taken along the reference ray. As δH is invariant along any solution of system (3.13), equation (3.14) merely needs to be satisfied at $\tau = 0$.

Two-point ray tracing

Our aim is to compute the ray going from a curved wavefront, known on the edges of a rectangular region, through a medium of known velocity, to a given receiver, so as to compute the arrival time at the receiver. To simplify the computation, the rays are traced from $\tau = 0$ at the receiver back to the edge of the box.

The boundary conditions are as follows: first, the ray goes through the receiver position $\mathbf{x_r}$ at $\tau = 0$, that is

$$\mathbf{x}(0) = \mathbf{x_r} \tag{3.15}$$

Second, the projections of the slowness vector of the ray and of the arrival time gradient onto the edge of the model must be equal. The arrival time T_0 of the incident wave at the edge of the model is known, its definition along the edge allowing the wavefront to be non-planar. The slowness vector of a ray intersecting the edge of the model across a boundary parallel to the x_i axis satisfies the boundary condition:

$$p_i = -\frac{\partial T_0}{\partial x_i} \tag{3.16}$$

where we use the definition of the slowness vector $\mathbf{p} = \nabla_{\mathbf{x}}T$, and the negative sign comes from the fact that the ray is traced from the station to the edge of the model.

The reference ray with initial slowness vector $\mathbf{p_0}(0)$ in the direction given by the theoretical backazimuth of the wave is first traced from the receiver to the edge of the medium. All quantities on this central ray are identified by the subscript $_0$. This ray satisfies the boundary condition (3.15), but not necessarily (3.16) as four initial scalar conditions are needed to define the ray at $\tau = 0$ ($x_1(0)$, $x_2(0)$, $p_1(0)$ and $p_2(0)$), and we have chosen $\mathbf{p_0}(0)$ arbitrarily.

We therefore calculate the paraxial ray associated with this reference ray which satisfies both boundary conditions (3.15) and (3.16) to first order. The four required initial conditions of the paraxial ray may be obtained from the following boundary conditions:

1+2) The paraxial ray as well as the central ray goes through the receiver at $\tau = 0$ so that:

$$\delta x_1(0) = 0 \quad \text{and} \quad \delta x_2(0) = 0 \tag{3.17}$$

3) From equations (3.14) and (3.17) and taking into account the canonical equation (3.12), we obtain

$$\mathbf{p_0}(0) \cdot \delta\mathbf{p}(0) = 0 \tag{3.18}$$

4) The last expression is less straightforward. Let us denote by τ_i and τ_i' the τ-values of the reference ray and the paraxial ray at their respective intersection

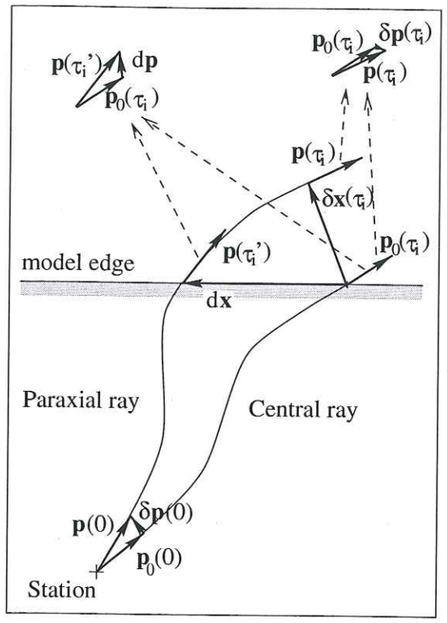

FIG. 3.4 – *Paraxial ray tracing.* $\mathbf{p}$*: slowness vector;* $\mathbf{x}$*: position vector;* τ*: sampling parameter; see main text for the definition of the other terms.*

points with the edge of the model (Fig. 3.4). From the values $\mathbf{x_0}(\tau_i)$ and $\mathbf{p_0}(\tau_i)$ of the central ray on the edge of the model, the values $\mathbf{x}(\tau_i')$ and $\mathbf{p}(\tau_i')$ of the paraxial ray at the same edge can be derived from a projection. Let $\mathbf{n}$ be the unit vector normal to the edge and let us define $\mathrm{d}\mathbf{x} = \mathbf{x}(\tau_i') - \mathbf{x_0}(\tau_i)$ and $\mathrm{d}\mathbf{p} = \mathbf{p}(\tau_i') - \mathbf{p_0}(\tau_i)$. To first order, the relation between $(\mathrm{d}\mathbf{x},\ \mathrm{d}\mathbf{p})$ and $(\delta\mathbf{x}(\tau_i),\ \delta\mathbf{p}(\tau_i))$ is [Farra, 1990]

$$\begin{aligned} \mathrm{d}\mathbf{x} &= \mathbf{\Pi_1}\delta\mathbf{x}(\tau_i) \\ \mathrm{d}\mathbf{p} &= \mathbf{\Pi_2}\delta\mathbf{x}(\tau_i) + \delta\mathbf{p}(\tau_i) \end{aligned} \tag{3.19}$$

where the projection matrices $\mathbf{\Pi_1}$ and $\mathbf{\Pi_2}$ are defined by:

$$\mathbf{\Pi_1} = \mathbf{I} - \frac{\nabla_\mathbf{p} H\ \mathbf{n}^T}{\nabla_\mathbf{p} H \cdot \mathbf{n}} \quad \text{and} \quad \mathbf{\Pi_2} = \frac{\nabla_\mathbf{x} H\ \mathbf{n}^T}{\nabla_\mathbf{p} H \cdot \mathbf{n}} \tag{3.20}$$

$\mathbf{I}$ is a 2×2 identity matrix; $\mathbf{n}^T$ is the transpose of vector $\mathbf{n}$ so that $(\nabla_\mathbf{p} H\ \mathbf{n}^T)_{ij} = (\nabla_\mathbf{p} H)_i\ \mathbf{n}_j$. All computations are made on the central ray at $(\mathbf{x_0}(\tau_i),\ \mathbf{p_0}(\tau_i))$. Replacing p_i by $p_{0_i} + \mathrm{d}p_i$ and $\frac{\partial T_0}{\partial x_i}(\mathbf{x})$ by $\frac{\partial T_0}{\partial x_i}(\mathbf{x_0} + \mathrm{d}\mathbf{x})$ in equation (3.16), and

expanding $\partial T_0/\partial x_i$ to first order, we obtain the final condition:

$$\frac{\partial^2 T_0(\mathbf{x_0})}{\partial x_i^2}\mathrm{d}x_i + \mathrm{d}p_i = -\frac{\partial T_0(\mathbf{x_0})}{\partial x_i} - p_{0i} \tag{3.21}$$

The two components of $\delta\mathbf{p}(0)$ may be obtained from relations (3.18) and (3.21), using the paraxial propagator of system (3.13) between τ_i and 0 and relation (3.19).

Due to the use of first order approximations, the two-point ray tracing procedure is iterative. We first trace the ray with initial slowness vector $\mathbf{p_0}(0)$, of which the direction is given by the theoretical backazimuth of the wave, to the edge of the model; then the paraxial propagator is computed. The initial conditions of the paraxial ray are determined to satisfy the boundary conditions (3.17), (3.18) and (3.21). Then, a fresh iteration starts with $\mathbf{p_0}(0) + \delta\mathbf{p}(0)$ as the revised initial slowness vector for the reference ray. The process stops when the central ray satisfies the boundary conditions (3.15) and (3.16) within predefined convergence criteria.

Finally, the travel time of the wave at the station is derived by integration along the ray:

$$T = \int_{ray} \mathbf{p}\cdot\dot{\mathbf{x}}\ \mathrm{d}\tau = \int_{ray} u^2(\mathbf{x}(\tau))\ \mathrm{d}\tau \tag{3.22}$$

3.2.4 Inverse problem

The data are the arrival times T_i^{obs} measured for each event at each receiver. We denote by T_i^c the travel times calculated with the ray tracing procedure explained above, using as input a 2-D velocity model and for each wavefront the arrival time T_0 at the edges of the study region. The inverse problem consists of estimating the model $\mathbf{m}$ that explains the observed travel times in a least-squares sense, that is, that minimizes the least-squares misfit function S defined as:

$$\begin{aligned} S(\mathbf{m}) &= [\mathbf{T}^{obs} - \mathbf{T}^c(\mathbf{m})]^T \mathbf{C}_T^{-1} [\mathbf{T}^{obs} - \mathbf{T}^c(\mathbf{m})] \\ &\quad + [\mathbf{F}_m - \mathbf{F}(\mathbf{m})]^T \mathbf{C}_F^{-1} [\mathbf{F}_m - \mathbf{F}(\mathbf{m})] \end{aligned} \tag{3.23}$$

where $\mathbf{T}^{obs}$ and $\mathbf{T}^c(\mathbf{m})$ are vectors containing the observed and calculated travel times respectively, $\mathbf{C}_T$ is the covariance matrix of observed travel time data and $\mathbf{m}$ is a vector containing the velocity model, or more precisely the square of the slowness in a grid covering the study area, and the arrival times T_0 of the incoming wavefront at the appropriate edges of the model. To constrain the solution, we introduce *a priori* values $\mathbf{F}_m$ of some parameter combinations $\mathbf{F}(\mathbf{m})$ (see section 3.2.4). The model covariance matrix $\mathbf{C}_F$ describes the uncertainties in the *a priori* values $\mathbf{F}_m$ [Farra & Madariaga, 1988].

The non-linear least-squares problem (3.23) can be solved iteratively by the Gauss-Newton method. The functions $\mathbf{T}^c(\mathbf{m})$ and $\mathbf{F}(\mathbf{m})$ in expression (3.23) are linearized around a current model $\mathbf{m_0}$ to obtain the quadratic approximation $E(\Delta\mathbf{m})$ of the least-squares misfit function S:

$$\begin{aligned} E(\Delta\mathbf{m}) &= [\Delta\mathbf{T} - \mathbf{A}_T\Delta\mathbf{m}]^T\mathbf{C}_T^{-1}[\Delta\mathbf{T} - \mathbf{A}_T\Delta\mathbf{m}] \\ &\quad +[\Delta\mathbf{F}_m - \mathbf{A}_F\Delta\mathbf{m}]^T\mathbf{C}_F^{-1}[\Delta\mathbf{F}_m - \mathbf{A}_F\Delta\mathbf{m}] \end{aligned} \tag{3.24}$$

where $\Delta\mathbf{T} = \mathbf{T}^{obs} - \mathbf{T}^c(\mathbf{m_0})$ contains the arrival time residuals, that is, the differences between the measured and the computed arrival times; $\Delta\mathbf{m}$ is the parameter perturbation; and $\mathbf{A}_T = \partial\mathbf{T}^c/\partial\mathbf{m}$ is a matrix containing the partial derivatives of the travel time with respect to the parameters, also known as Fréchet derivatives (see section 3.2.4). The vector $\Delta\mathbf{F}_m = \mathbf{F}_m - \mathbf{F}(\mathbf{m_0})$ and the matrix $\mathbf{A}_F = \partial\mathbf{F}/\partial\mathbf{m}$ describe additional constraints such as *a priori* information and regularization, which we describe in more detail in section 3.2.4. As the data are assumed to be uncorrelated, we set the non-diagonal terms of matrices $\mathbf{C}_T$ and $\mathbf{C}_F$ to zero. The diagonal terms are computed from uncertainties in the travel time measurements (see section 3.2.6 for estimation on real data) and *a priori* values of the combinations of the parameters $\mathbf{F}(\mathbf{m})$.

Let us introduce the diagonal matrices σ_T and σ_F defined as $\sigma_T^2 = \mathbf{C}_T$ and $\sigma_F^2 = \mathbf{C}_F$ and the matrix $\mathbf{D}$ as $\mathbf{D} = \begin{pmatrix} \sigma_T^{-1}\mathbf{A}_T \\ \sigma_F^{-1}\mathbf{A}_F \end{pmatrix}$. The least-squares solution of

the misfit function (3.24)

$$\Delta\mathbf{m} = (\mathbf{D}^T\mathbf{D})^{-1}\mathbf{D}^T \begin{pmatrix} \sigma_T^{-1}\Delta\mathbf{T} \\ \sigma_F^{-1}\Delta\mathbf{F}_m \end{pmatrix} \tag{3.25}$$

is obtained by singular value decomposition of matrix $\mathbf{D}$. As the problem is non-linear, the process is repeated until the residuals $\Delta\mathbf{T}$ drop to the level of measurement error. At each iteration the rays are traced using the procedure described in section 3.2.3.

An *a posteriori* error analysis is performed to evaluate a model confidence interval. This estimate is obtained by deriving the *a posteriori* covariance matrix $\mathbf{C}'_M$ [Tarantola, 1987]:

$$\mathbf{C}'_M = (\mathbf{A}_T^T\mathbf{C}_T^{-1}\mathbf{A}_T + \mathbf{A}_F^T\mathbf{C}_F^{-1}\mathbf{A}_F)^{-1} \tag{3.26}$$

The diagonal elements of $\mathbf{C}'_M$ are an estimate of the square of the uncertainty in the model obtained from the inversion. They depend on the array geometry and the number of data used in the inversion rather than on the model parameters.

Parameterization

Because of the form of the ray tracing equations, the parameters of the model $\mathbf{m}$ are the square of the slowness, and the arrival times of every incoming wavefront at the edge of the parameterized region. All these functions are modeled by B-splines [de Boor, 1978; Bartels *et al.*, 1988; Farra & Madariaga, 1988].

The square of the slowness is interpolated using third-order two-dimensional B-splines:

$$u^2(x_1, x_2) = \sum_{i=1}^{N_{x_1}} \sum_{j=1}^{N_{x_2}} u_{ij}^2 B_{u_{ij}}(x_1, x_2) \tag{3.27}$$

where u_{ij}^2, $i = 1, \ldots, N_{x_1}$, $j = 1, \ldots, N_{x_2}$ are the coefficients of B-spline interpolation and $B_{u_{ij}}$ are 2-D spline basis functions.

Each wavefront is described by its arrival time at the two edges of the model first encountered by the wave (Fig. 3.5). Along each edge, the arrival time is

modeled using fourth order B-spline interpolation:

$$T_0(x_k) = \sum_{i=1}^{N_{t_k}} T_{0_i} B_{t_i}(x_k) \tag{3.28}$$

where T_{0_i}, $i = 1, \ldots, N_{t_k}$, are the spline coefficients and B_{t_i} are the spline basis functions.

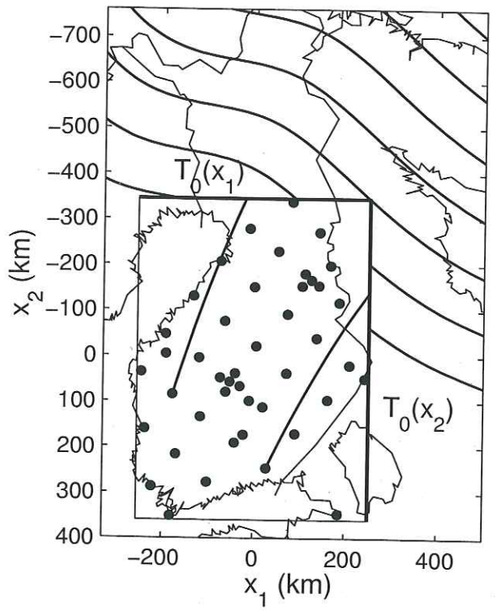

FIG. 3.5 – *Setting of the problem for the SVEKALAPKO deep seismic experiment. Position of the broadband receivers are the black dots, the rectangular box is the limit used in the computations. An example of a curved wavefront propagating from the north-east outside the model is shown together with two rays traced from the edge of the model to two stations. The shape of the wavefront is modeled by the arrival time of the wave on the box:* $T_0(x_1)$ *and* $T_0(x_2)$.

Fréchet derivatives of the arrival time

To solve the inverse problem, we need to compute the matrix $\mathbf{A}_T$ of equation (3.24) containing the partial derivatives of travel times. This requires us to compute the variation in arrival time due to velocity perturbations, and the variation in arrival time due to perturbation of the wavefronts, that is, the variation in the T_0 parameters.

Let us first calculate the Fréchet derivatives with respect to the square of the slowness. In the reference medium of slowness squared u^2_{ref} we denote by R_{ref} the ray between station S and point M on the edge of the model. If the square of the slowness is modified from u^2_{ref} to $u^2 = u^2_{ref} + \Delta u^2$, we can trace the new ray R joining S and M in the perturbed model. This new ray may not satisfy the boundary condition (3.16): coherence between the slowness vector of the ray and the gradient of T_0. We denote by R' the ray of the perturbed medium which satisfies the boundary conditions (3.15-3.16). This ray intersects the edge of the model at M'. Subscript ref indicates quantities obtained in the reference medium.

In the perturbed medium, the arrival time $T(S)$ is:

$$T(S) = T_0(M') + \int_{R'} u^2 \mathrm{d}\tau \tag{3.29}$$

$$= T_0(M') + \int_R u^2 \mathrm{d}\tau + \mathbf{p} \cdot \overrightarrow{MM'} \tag{3.30}$$

where $\mathbf{p} = -\nabla_{\mathbf{x}} T(M)$ is the slowness vector at the edge of the model (the negative sign is due to our convention of computing the ray from the station to the edge of the box).

Fermat's principle implies that:

$$\int_R u^2 \mathrm{d}\tau = \int_{R_{ref}} u^2_{ref} \mathrm{d}\tau + \int_{R_{ref}} \Delta u^2 \mathrm{d}\tau \tag{3.31}$$

To first order, we also know that $T_0(M') = T_0(M) + \nabla_{\mathbf{x}} T \cdot \overrightarrow{MM'}$. The relation between the arrival times at the station in the reference medium and in the

perturbed medium is:

$$T(S) = T_0(M) + \int_{R_{ref}} u_{ref}^2 \mathrm{d}\tau + \int_{R_{ref}} \Delta u^2 \mathrm{d}\tau \quad (3.32)$$

$$= T_{ref}(S) + \int_{R_{ref}} \Delta u^2 \mathrm{d}\tau \quad (3.33)$$

Therefore, using parameterization (3.27), we derive the Fréchet derivatives with respect to the square of the slowness parameters:

$$\frac{\partial T(S)}{\partial u_{ij}^2} = \int_{R_{ref}} B_{u_{ij}}(x_1, x_2)\mathrm{d}\tau \quad (3.34)$$

Let us now calculate the Fréchet derivatives with respect to the arrival time T_0 of the wave at the edge of the modeled region. For the reference arrival times T_{0ref} and the square of the slowness model u^2, we denote by R the ray between the station S and the point M on the edge of the model which satisfies the boundary condition (3.16). Let us consider a perturbation ΔT_0, so that $T_0 = T_{0ref} + \Delta T_0$, and the ray R' satisfying conditions (3.15-3.16) in the perturbed model. The ray R' is traced from the station S to the point M' on the edge of the study region. Starting from equation (3.30) and from $T_0(M') = T_{0ref}(M) + \Delta T_0(M) + \nabla_{\mathbf{x}} T \cdot \overrightarrow{MM'}$, we obtain

$$T(S) = T_{0ref}(M) + \Delta T_0(M) + \int_R u^2 \mathrm{d}\tau \quad (3.35)$$

$$= T_{ref}(S) + \Delta T_0(M) \quad (3.36)$$

Using parameterization (3.28), we obtain the Fréchet derivatives with respect to the T_0 parameters:

$$\frac{\partial T(S)}{\partial T_{0_i}} = B_{t_i}(x(M)) \quad (3.37)$$

A priori **information**

Additional *a priori* information is usually needed to make the inverse problem non-singular. To limit the roughness of the solution, we can minimize the value of the first and second order derivatives of the square of the slowness by introducing a function $\mathbf{F}(\mathbf{m})$ in equation (3.23). This function can be used to set the first and

second order derivatives equal to zero with given uncertainties, denoted by σ_{F_1} and σ_{F_2} respectively. In practice, the constraints are introduced through the first and second finite differences of the B-spline parameters u_{ij}^2.

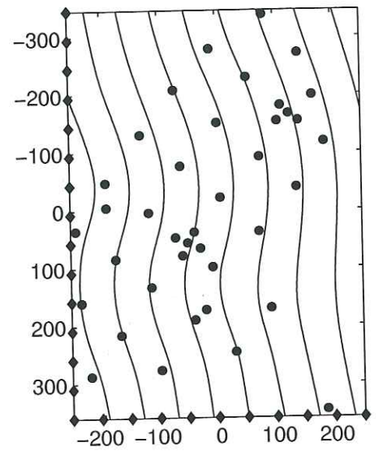

FIG. 3.6 – *Propagation of the curved wavefront with theoretical backazimuth* 260° *through the station network. Propagation time is interpolated from the arrival time at the receivers (dots) and at two edges of the study region (diamonds). Wavefronts 15 s apart are plotted as solid lines.*

We add two constraints on the shape of the wavefront. Each wavefront is modeled by the arrival time T_0 along two boundaries of the region, the two sets of arrival times being treated independently (Fig. 3.5). We therefore impose the condition that the values at the point shared by the two lines at the corner of the region are identical, to within σ_{F_3}, an amount equal to the data uncertainty. We also impose a certain degree of smoothness on the incoming wavefront. To obtain this, the derivative of the arrival time along the edge should not be very different from that given by the theoretical propagation angle ϕ:

$$\frac{\partial T_0}{\partial x_1} = -\frac{\sin\phi}{c} \quad \text{or} \quad \frac{\partial T_0}{\partial x_2} = \frac{\cos\phi}{c} \quad (3.38)$$

according to the edge considered. In (3.38), c is the wave speed at the point considered and ϕ is the theoretical backazimuth or a measured propagation direction. The x_1 and x_2 axes are oriented toward the East and South, respectively. We denote by σ_{F_4} the corresponding *a priori* uncertainty. σ_{F_4} therefore controls the upper limit of allowed variation in the local backazimuth of a wavefront, as compared to a plane wave. This upper limit depends strongly on the theoretical backazimuth of the incident wave. For $\sigma_{F_4} = 0.05$ s.km^{-1} used in the inversions presented here, the upper limit is at least 10°. An example of curved wavefronts is shown on Fig. 3.6 and discussed in more detail in section 3.2.5.

The strength of the constraints, related to σ_{F_1}, σ_{F_2}, σ_{F_3} and σ_{F_4}, is chosen as a compromise between stability of the inversion and data misfit.

3.2.5 Numerical examples

The inversion was applied to several synthetic examples. The station geometry is that of the SVEKALAPKO experiment (Fig. 3.5). This two-dimensional arrangement is significantly better than that usually used for 2-D body-wave tomography, as the receivers are distributed throughout the modeled area and not only along one edge. The sources are a set of 36 theoretical events evenly distributed in azimuth. We want to obtain the phase velocity structure in the rectangular region containing this network and shown in Fig. 3.5. In the first part of this section (3.2.5-3.2.5) we use arrival times at the stations calculated by ray tracing to study the behaviour of the inversion procedure in ideal conditions. In section 3.2.5 we use full waveform modeling with and without noise to approach more realistic conditions.

At every run of the inversion the data misfit $\|\mathbf{\Delta T}\|$ is computed, that is the root mean square of the time residuals. As we know the true velocity model, we also compute the model misfit Δc as the root mean square of the difference in phase velocity c. To take into account the lack of resolution in some areas, the

differences in velocity are weighted by the inverse of the *a posteriori* error in the velocity σ_c.

$$\Delta c(\mathbf{m}) = \sqrt{\frac{1}{\sum 1/\sigma_c^2} \sum \left(\frac{c_{true} - c(\mathbf{m})}{\sigma_c} \right)^2} \tag{3.39}$$

The *a posteriori* error in the velocity is obtained from that of the square of the slowness, σ_{u^2}, using the relation:

$$\sigma_c = c_{true}^3 \sigma_{u^2}/2 \tag{3.40}$$

σ_{u^2} is the square root of the diagonal elements of matrix C'_M given by (3.26) corresponding to the square of the slowness parameters. In (3.39), the summation is made with points regularly distributed every 5 km inside the box.

The parameters of the model being of two types with different orders of magnitude (0.1 s^2.km^{-2} for the square of the slowness and 100 s for the arrival times), we apply a normalization in all numerical examples and used as parameters in the inversion procedure the square of the slowness divided by 0.1 and the wavefront arrival times divided by 100.

Sensitivity test

The checker-board test cannot reasonably be applied to a ray tracing method as the condition of smooth structure is not respected. We therefore considered a 2-D phase velocity model of a B-spline interpolated checker-board. The cell width is 150 km and the maximum variation of the phase velocity is 5% between 4 and 4.2 km.s^{-1} (Fig. 3.7a). The synthetic data set consisted of the arrival times of 36 wavefronts at the receivers, computed using the ray tracing method described in section 3.2.3. In this example, the wavefronts incident upon the structure were plane.

The starting model of the inversion procedure is homogeneous with a velocity of 4.1 km.s^{-1}. The initial incoming wavefronts are plane. Rays are traced through this initial model and travel times computed; the root mean square of the arrival time residuals is $\|\mathbf{\Delta T}\| = 0.63$ s.

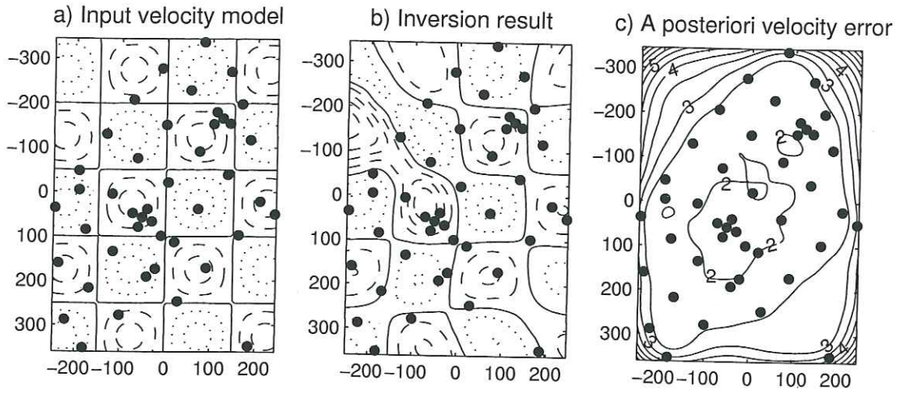

FIG. 3.7 – *Sensitivity test. a) true velocity model used to compute the arrival times. b) velocity model obtained after 2 iterations of the inversion. Contours are every 0.04 km.s^{-1}, solid line for 4.1 km.s^{-1}, dotted lines for lower velocities, dashed line for larger velocities. c) A posteriori velocity error as a percentage of the true velocity. Station positions are given by the black dots.*

The inverse problem consisted of evaluating the velocity field and the 36 wavefronts. The square of the slowness is represented by B-spline interpolation with 192 coefficients (12×16) corresponding to a regular mesh of grid points distributed every 50 km (about half of the mean distance between the stations). The arrival times T_0 of the 36 incident wavefronts are represented by B-spline interpolation with 11 and 15 coefficients (corresponding to grid points regularly distributed every 50 km), along the West-East and North-South edges of the box, that is 936 parameters. The model is then fully described by 1128 parameters. We assume an uncertainty of 1 s in the travel time data.

If we invert the times residuals without *a priori* constraints, the velocity model obtained shows very high amplitude anomalies in the corners with a weak station coverage. We therefore introduced *a priori* information as described in section 3.2.4, using the following values: $\sigma_{F_1} = 3 \times 10^{-4}$ s^2.km^{-3} (5% variation of the

velocity is allowed over a distance of 20 km), $\sigma_{F_2} = 6 \times 10^{-6}$ s^2.km^{-4} ($\sigma_{F_2} = \sigma_{F_1}/50$), $\sigma_{F_3} = 1$ s, and $\sigma_{F_4} = 5 \times 10^{-2}$ s.km^{-1} (at least 10° variation is allowed in the propagation direction). The inversion process is stopped when the travel time misfit no longer decreases.

Table 3.1 shows the number of data and parameters, and the initial and final values of the data and model misfits for comparison between all numerical examples. The final model (Fig. 3.7b) was obtained after 2 iterations, with final data misfit $\|\mathbf{\Delta T}\| = 0.34$ s. The model misfit defined by equation (3.39) is 0.02 km.s^{-1} (0.5% of the velocity). The *a posteriori* error in the velocity model σ_c, estimated by equation (3.40), shown in Fig. 3.7c has a mean of 2.6% of the true velocity. It is almost constant in the central part of the box where the stations are located, with a value of approximately 2%.

When the cell size of the input model is smaller than 150 km, the data misfit hardly decreases. For 100 km cell size the checker-board is reconstructed but with smaller velocity variations than in the input model. For models with cell size larger than 150 km, the inversion result is closer to the true velocity model than in the case with 150 km cell size presented above.

The sensitivity tests tell us that structures smaller than approximately 150 km cannot really be imaged with the SVEKALAPKO experiment, even with a perfect set of recorded events. This is related to the inter-station distance in the SVEKALAPKO array, which is approximately 100 km. The north-western and south-eastern corners of the box are poorly constrained due to the lack of receivers in these regions.

Non-planar incoming wavefronts

In the following example the incident wavefronts were randomly, but smoothly, distorted. We are not expecting backazimuth anomalies larger than 5° in Fennoscandia, considering that the region is relatively homogeneous and taking into

	N	M	P	data misfit initial	data misfit final	model misfit initial	model misfit final	I
				s		$\times 10^{-2}$ km.s^{-1}		
cb	1573	3161	1128	0.63	0.34	5.38	2.04	2
npwf	1434	3022	1128	3.18	0.29	0	3.96	3
moho	1582	3170	1128	0.75	0.02	7.50	0.36	2
IBEM_25s	1320	2758	972	1.35	0.11	7.91	0.75	3
IBEM_33s	1320	2758	972	1.51	0.20	8.90	2.40	3*
IBEM_50s	1320	2758	972	0.88	0.25	4.90	0.90	3*
IBEM_az_33s	1320	2758	972	1.63	0.16	8.90	2.52	2
IBEM_n_25s	1320	2758	972	1.42	0.39	7.91	1.36	2
IBEM_n_33s	1320	2758	972	1.59	0.55	8.90	2.13	3*
IBEM_n_50s	1320	2758	972	1.38	1.06	4.90	7.62	3*
SVEKA_60s	1390	2942	1104	3.04	1.21	-	-	4*

TAB. 3.1 – *Numerical values that characterize the inversions. N: number of time residuals; M: total number of lines in the inversion matrix (data and constraints); P: number of parameters. For definitions of data and model misfits see main text. I: number of iterations; (*) regularization constraints used in the first iteration(s). For values of the assumed error in the data and of the constraints see main text. cb: checker-board test; npwf: homogeneous velocity model with non-planar incoming wavefronts; moho: input velocity model computed from the Moho-depth map of Luosto [1990] for a 35 s fundamental-mode Rayleigh wave; IBEM_XXs: no-noise IBEM synthetic seismograms at XX seconds, IBEM_az_XXs: no-noise IBEM synthetic data set with a bad azimuthal coverage, IBEM_n_XXs: IBEM seismograms with noise; SVEKA_60s: real seismograms of the SVEKALAPKO seismic tomography experiment at 60 s period.*

account the azimuth anomalies measured by Levshin & Berteussen [1979] over the Barents Sea. We therefore modified the backazimuth of our 36 wavefronts with a random rotation of 5° maximum. Friederich *et al.* [1994] also observed a local curvature of the wave-fields propagating over Germany. Onto the constant rotation we superimposed random small scale variations of 30° maximum within 100 km along the wavefront. The input velocity model was homogeneous with a value of 4.0 km.s^{-1}. The number of data inverted is 1434 (Table 3.1), which should be compared with the maximum possible of 1584 corresponding to 36 events × 44 receivers. The missing data correspond to rays that the ray tracing procedure was not able to compute because of the perturbation of the wavefront.

The starting velocity model for the inversion was homogeneous with a velocity of 4.0 km.s^{-1}. The initial wavefronts are plane and incident from the theoretical backazimuth, that is, without the constant rotation. Rotation of the wavefronts as compared to the theoretical backazimuth used in the starting model leads to systematic bias of the time residuals. To obtain a minimal initial estimate of the data misfit for Table 3.1 we computed the root mean square of the residuals by adding a constant to every arrival time of each wavefront, so that the data misfit is minimal: $\|\mathbf{\Delta T}\| = 3.18$ s. The parameterization used is the same as in the previous example, so the total number of parameters is 1128. The assumed data error is 1 s. The constraints used in the inversion are $\sigma_{F_1} = 3 \times 10^{-4}$ s^2.km^{-3}, $\sigma_{F_2} = 6 \times 10^{-6}$ s^2.km^{-4}, $\sigma_{F_3} = 1$ s, and $\sigma_{F_4} = 5 \times 10^{-2}$ s.km^{-1}.

After 3 iterations, the final model was obtained. The data misfit is $\|\mathbf{\Delta T}\| =$ 0.29 s. The model misfit is 0.040 km.s^{-1}, 1% of the input phase velocity. The misfit is concentrated in the unresolved areas; if we compute the model misfit on a restricted area containing the network, it falls below 0.6%. The *a posteriori* error has the same shape as in the preceding example, with a mean value of 2.6%.

Four examples of a wavefront are shown in Fig. 3.8. The disagreement between input and reconstructed wavefronts can be large but such misfit generally occurs in poorly resolved areas, such as the north-western corner showing a 10 s difference

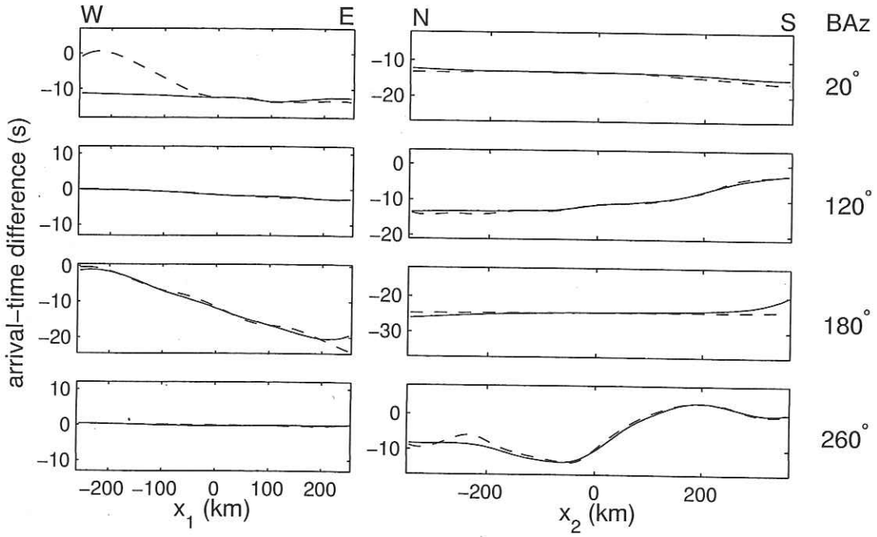

FIG. 3.8 – *Four examples of non-planar wavefronts. Arrival time differences between the curved waves (input wavefront with a dashed line and inversion result with a solid line) and the plane wave coming from the theoretical backazimuth. Left panels: edge parallel to the x_1 axis; Right panels: edge parallel to the x_2 axis*

in the first panel of Fig. 3.8 for the backazimuth of 20°. Fig. 3.6 gives an example of a curved wavefront propagating across the station network, interpolated from the inversion result.

The mean of the *a posteriori* error on the arrival time of the wavefronts T_0 is 2.2 s. The maximum estimated error for one wavefront occurs either at the corner where the station coverage is weak, or for an edge almost parallel to the propagation direction at the end where the wavefront leaves the study region.

The wavefront smoothness imposed in the inversion was stronger than the actual smoothness of the input wavefronts. We therefore compared the results using different values for σ_{F_4}. As a general trend, with weakening constraint on the wavefront smoothness, the data misfit increases but the model misfit decreases. For example with $\sigma_{F_4} = 0.13$ s.km^{-1} (30° variation in the backazimuth angle), the data misfit is $\|\mathbf{\Delta T}\| = 0.46$ s, and the model misfit is 0.020 km.s^{-1} for the whole study region and 0.016 km.s^{-1} in the well resolved area (0.4%). On the other hand, increasing roughness of the input wavefront (small scale variations up to 40° over 100 km) deteriorates the inversion result. With $\sigma_{F_4} = 5 \times 10^{-2}$, the data misfit is 0.75 s, the model misfit is 0.053 km.s^{-1}, and 0.042 km.s^{-1} below the stations. Increasing σ_{F_4} does not improve the result. The curvature of 40° over 100 km is the maximum that our inversion technique is able to manage.

In real cases, the measurement of the real propagation direction in small arrays at two different locations in the network may allow us to evaluate the global rotation of the wavefront and to eliminate events with excessively perturbed wavefronts.

Variable Moho depths model

In this example, we use a more realistic velocity model derived from the Moho depth map of Luosto [1990]. The physical model is composed of a single layer (the crust) over a half space (the mantle). The crust is defined by P- and S-velocities

$\alpha_1 = 6.5$ km.s^{-1}, $\beta_1 = 4.2$ km.s^{-1} and density $\rho_1 = 2700$ kg.m^{-3}, and the mantle by $\alpha_2 = 8.1$ km.s^{-1}, $\beta_2 = 5.35$ km.s^{-1} and $\rho_2 = 3100$ kg.m^{-3}. The thickness of the crust varies from 41.7 km to 60.6 km, as derived from the interpolated Moho-depth map of Luosto [1990]. At each grid point of the surface, the phase velocity dispersion curve is computed using the software edited by Herrmann [1985] with the 1-D model corresponding to the structure immediately below the location under consideration. We can therefore calculate a phase velocity map for each frequency. These maps can be used as the input velocity field to compute travel times with our ray tracing method. As an example we used the phase velocity map corresponding to the fundamental-mode Rayleigh wave of 35 seconds period (Fig. 3.9a). At this period the phase velocity varies between 4.15 and 4.38 km.s^{-1}. In reality the expected variations are lower, as the very thick crust is associated with high shear-velocities and densities in the lower crust. The sources considered were again 36 plane waves evenly distributed in azimuth.

The starting velocity model for the inversion process is homogeneous with a velocity of 4.26 km.s^{-1}. The initial incoming wavefronts are plane waves. The root mean square of the travel time residuals is $\|\mathbf{\Delta T}\| = 0.75$ s and the assumed error in the data is 1 s.

The parameters of the inverse problem are the 192 squares of the slowness parameters and the 936 arrival time parameters. The constraints are $\sigma_{F_1} = 3 \times 10^{-4}$ s^2.km^{-3}, $\sigma_{F_2} = 6 \times 10^{-6}$ s^2.km^{-4}, $\sigma_{F_3} = 1$ s, and $\sigma_{F_4} = 5 \times 10^{-2}$ s.km^{-1}. Fig. 3.9b shows the velocity model generated after 2 iterations of the inversion process. The characteristics of the inversion can be found in Table 3.1. The final root mean square of the time residuals is $\|\mathbf{\Delta T}\| = 0.02$ s. The model misfit is 0.004 km.s^{-1} (0.08% of the input velocity). The *a posteriori* error on the velocity field has an average of 2.8%.

The results obtained with this velocity model are particularly good and encouraging for the future interpretation of the SVEKALAPKO data.

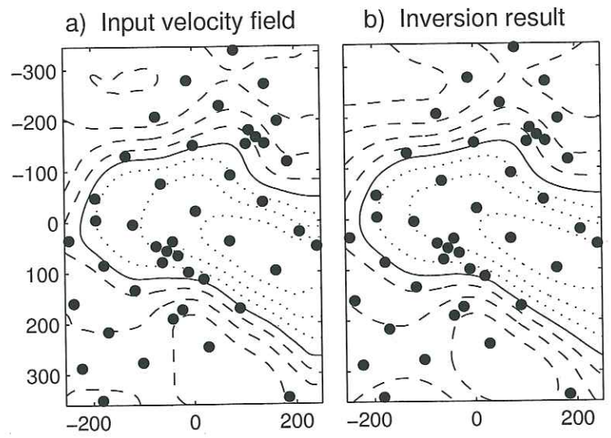

FIG. 3.9 – *Inversion based on the phase velocity model derived from Luosto [1990] Moho depth map, for the Rayleigh fundamental-mode at 35 s period. a) true velocity field. b) inversion result after 2 iterations. Contours are every 0.03 km.s^{-1}, solid line for 4.26 km.s^{-1}, dotted lines for lower velocities, dashed line for larger velocities. Station positions are given by the black dots.*

Data computed with Indirect Boundary Element Method

Up to now all the examples were carried out using arrival times computed with the ray tracing method that is also used in the inversion. To study the performance of the inversion using more realistic input data, we computed synthetic seismograms using the Indirect Boundary Element Method [Pedersen *et al.*, 1996]. This method computes the complete wave-field caused by a plane surface wave obliquely incident upon a 2-D structure. The incident wave can have any backazimuth, but the computation becomes unstable when the propagation direction is close to the axis of the structure [Pedersen *et al.*, 1994]. We therefore kept only 30 events, eliminating three azimuths around 90° and three around 270°. The modeled source is a fundamental-mode Rayleigh wave, with a Ricker wavelet source function centered on 0.04 Hz frequency. The structure is the sim-

plified cross section of the Moho-depth map from Luosto [1990] described in the beginning of section 3.2.2 and shown in Fig. 3.1. As the model does not take into account the high velocity at the base of the thickened crust, the sharp velocity contrast will produce stronger diffractions than we expect in a more realistic model of the area.

For each event, we measured on the synthetic seismograms the time delays between a reference station, chosen as the first station reached by the wave, and all the other receivers. Time delays were found through the two-step algorithm described in section 3.2.2. The assumed data uncertainty is 1 s.

Fig. 3.10a, d and g display the theoretical phase velocity models obtained for three selected periods (25, 33 and 50 seconds). This theoretical velocity is the phase velocity of the fundamental local mode, computed using the same procedure as in section 3.2.2. However, because IBEM uses the physical 2-D model of Fig. 3.1 as input, and the theoretical phase velocity maps shown in Fig. 3.10a, d and g are not used in the calculation of the synthetic data set, it should not be considered as the true velocity. The average theoretical phase velocity is 4.05, 4.25 and 4.46 km.s^{-1} for 25, 33 and 50 s periods respectively, resulting in wavelengths of approximately 100, 140 and 225 km.

The starting velocity models are homogeneous with velocity 4.02, 4.23 and 4.44 km.s^{-1} respectively. The initial root mean square of the arrival time residuals is between 0.88 and 1.51 s. The inverse problem consists of evaluating the 192 spline coefficients for the velocity model, and the 780 T_0 parameters describing the 30 wavefronts, that is a total of 972 parameters. The data and model misfits are given in Table 3.1. The final values of the constraints are $\sigma_{F_1} = 3 \times 10^{-4}$ s^2.km^{-3}, $\sigma_{F_2} = 6 \times 10^{-6}$ s^2.km^{-4}, $\sigma_{F_3} = 1$ s, and $\sigma_{F_4} = 5 \times 10^{-2}$ s.km^{-1}. However, with the data set obtained for 33 and 50 s period, the inversion did not converge toward a model giving a lower data misfit. We therefore used regularization constraints for the first two iterations of the inversion process, that is, the smoothness criteria on the velocity field (for both periods) and on the wavefront (for the 50 s period

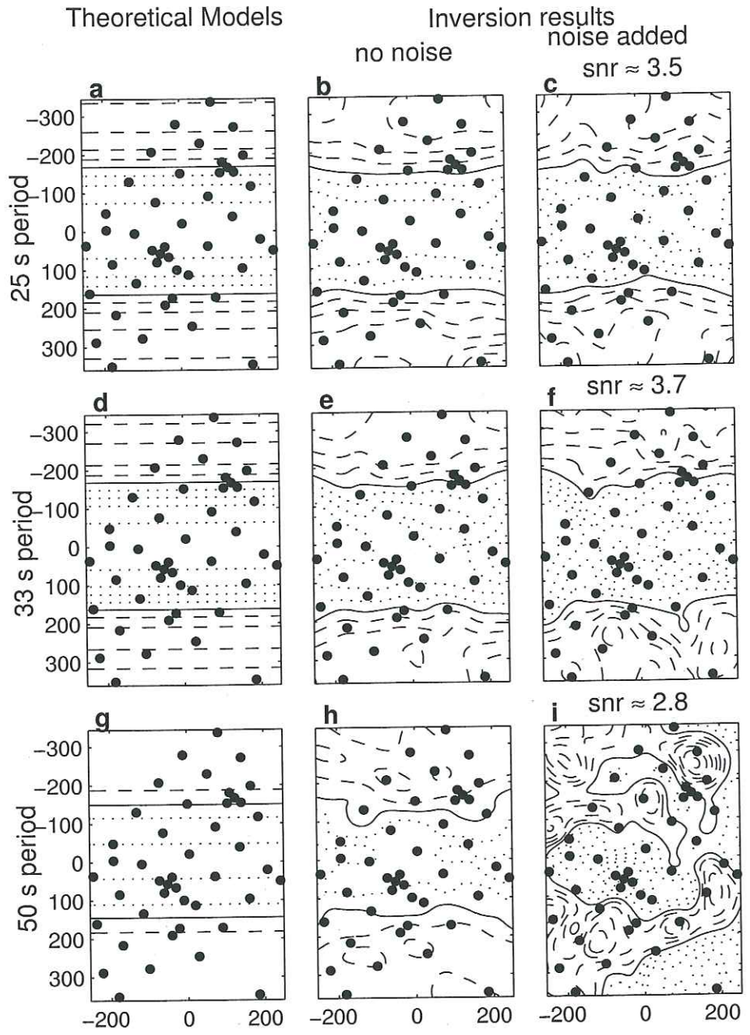

FIG. 3.10 – *Inversion of time delays measured on IBEM synthetic seismograms. On each plot the contours are every 0.03 km.s^{-1}, dotted lines are for lower velocities, dashed line for larger velocities. a) b) c) model for 25 s period, solid line for 4.02 km.s^{-1}. d) e) f) 33 s period, solid line for 4.23 km.s^{-1}. g) h) i) 50 s period, solid line for 4.44 km.s^{-1}. a) d) g) theoretical local phase velocities. b) e) h) models obtained from inversion of signals without noise. c) f) i) models obtained from inversion of the noisy signals; snr: signal to noise ratio. Black dots give the station locations.*

data set only) were very strong in the first two iterations and relaxed for the third.

The results of the inversions are shown in Fig. 3.10b, e and h. For the three frequencies, the low velocity area is reconstructed by the inversion. However, the minimum value obtained is larger than the theoretical value for the three periods selected. This is the result of the smoothing of the structure which can be expected due to the wavelength (see section 3.2.2). The final model misfits lie between 0.008 and 0.024 km.s^{-1}, the largest difference in velocity occurs either in the low velocity area where the smoothing has the strongest effect, or in the area with no stations. The average *a posteriori* error on the velocity field is 2.7, 3.0, and 3.2% of the theoretical velocity respectively for 25, 33 and 50 s period.

Another problem associated with a real data set would be the azimuthal coverage. We used a data set composed of arrival times for 22 wavefronts out of the 30 wavefronts computed, for the 33 s period model. The 22 wavefronts chosen are based on the azimuthal coverage obtained by Friederich [1998] in Germany.

The starting model has a homogeneous phase velocity of 4.23 km.s^{-1}. The initial data misfit is $\|\mathbf{\Delta T}\| = 1.6$ s. The final model is obtained after two iterations. The final data misfit is 0.16 s, the final model misfit is 0.025 km.s^{-1} (0.6% of the input velocity). The average *a posteriori* velocity error is 3.1%.

The inversion result is not really disturbed by the lack of data from the south. This is a consequence of the good station coverage of the SVEKALAPKO network.

We then added random noise to the synthetic seismograms. The measured signal to noise ratios are approximately 3.5, 3.7, and 2.8 for 25, 33 and 50 s period. Fig. 3.10c, f and i display the inversion results obtained with the data set measured on the noisy signals. Values of the misfits are given in Table 3.1. Regularization constraints on the velocity smoothness and on the wavefront smoothness were used for inversion of the data set obtained with 33 and 50 s period.

With a signal to noise ratio larger than 3.5, the inversion converges toward a solution équivalent to that obtained without noise. With a signal to noise ratio

smaller than 3, the true velocity field is not recovered.

The tests using IBEM-computed synthetic seismograms ratify both the technique of time delay measurement on the seismograms and the inversion method. In the case of simple and relatively smooth structures, ray theory can succeed in imaging heterogeneities of scale close to the wavelength even though velocity variations may be underestimated. Due to the good station coverage, the lack of data incident from some backazimuths is not a problem for the inversion. The minimum signal to noise ratio allowed in data is approximately 3.5.

3.2.6 Preliminary inversion of the SVEKALAPKO data

Finally we tested our method on real data. This section does not aim to solve the lithospheric structure of eastern Fennoscandia, but rather to demonstrate that the method can be applied successfully to real seismograms. For this preliminary inversion we use a subset of 48 high quality events (see Fig. 3.11), carrying out the analysis on the fundamental-mode Rayleigh wave at 60 seconds period. The azimuthal distribution is not as regular as in the synthetic tests but the corresponding *a posteriori* error is not very different from that obtained in the synthetic tests.

The vertical component seismograms were first filtered in the time-frequency domain using the apparent group velocity curves [Lander & Levshin, 1989]. For each station couple we measured the time delay using Wiener filtering on the filtered signals. Then we chose a reference station for each event, the first station encountered by the wave, unless its record was too noisy. For each station i we measured the time delay to the reference station as the median of $N-1$ time delays, N being the number of coherent records. One delay was measured directly between the reference station and station i. The $N-2$ others were obtained by the sum (or subtraction) of the time delay between the reference station and station j, and the time delay between station j and station i. The average standard

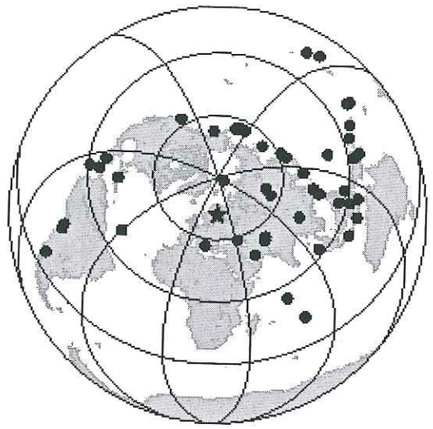

FIG. 3.11 – *Distribution of the 48 events used in the inversion. Black dots: epicenters; black star: center of the network of stations.*

deviation of approximately 2 seconds was used as data uncertainty. The number of time measurements kept for the inversion was 1390, that is 29 data per event on average.

As the number of data per event was somewhat lower than in the numerical tests, we decreased the number of spline coefficients representing the wave fronts to 8 and 11 for the West-East and North-South edges respectively (points distributed every 70 km). The number of coefficients representing the velocity model was kept to 192. The model is fully described by 1104 parameters.

The initial model for the inversion has a homogeneous velocity of 4.13 km.s^{-1}. This value was obtained by fitting one dispersion curve to all the observed time delays. The sources considered were 48 plane waves coming from the backazimuths computed for a radially symmetric Earth. In the initial model the origin time for each event is situated at the corner of the study area, whereas in the real data it is located at the reference stations. This constant time shift, which can be as high as 30 s, makes the inversion unstable. We therefore used strong regularization

constraints on the first iteration of the inversion process, so that the velocity model stays constant and the wavefronts remains plane but are shifted in time. In the second iteration the constraints were lowered to $\sigma_{F_1} = 3 \times 10^{-4}$ s^2.km^{-3}, $\sigma_{F_2} = 6 \times 10^{-6}$ s^2.km^{-4}, $\sigma_{F_3} = 2$ s, and $\sigma_{F_4} = 5 \times 10^{-2}$ s.km^{-1}.

The time shift also influences the estimation of the initial data misfit, which we addressed by adding a constant time to each event so that the root mean square of the time residual is minimum: $\|\mathbf{\Delta T}\| = 3.04$ s.

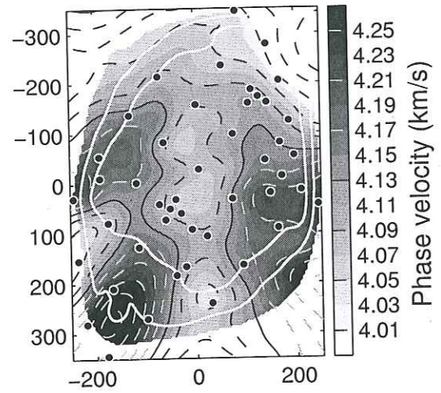

FIG. 3.12 – *Phase velocity of the fundamental-mode Rayleigh wave at 60 s period, as retrieved from inversion of the time residuals measured on real seismograms from the SVEKALAPKO seismic tomography experiment. Gray levels are inside the limit of a posteriori error on the velocity $\sigma_c = 4\%$; the thick white contours corresponds to $\sigma_c = 3.5\%$ and $\sigma_c = 3\%$.*

The final model was obtained after 4 iterations, with a final data misfit of 1.21 s (data uncertainty 2 s). Fig. 3.12 shows the phase velocity model obtained. The average *a posteriori* error in the velocity model is 3.4%, and if we consider only the part of the model inside the 3.5% contour then the mean *a posteriori* error decreases to 2.9%. This is most likely an overestimate of the real error. We will use a boot-strap approach to estimate the error on the velocity field obtained

from the real data set for further interpretation.

The sampling depth of the 60 s fundamental-mode Rayleigh wave is around 80 km. As the crustal thickness reaches 60 km in some areas, this phase velocity map is therefore influenced by the crustal structure. Comparing our map to the compilation of known Moho depths presented by Luosto [1997], shows that the deep crust to the west is associated with relatively low velocities, while the deep crust to the east is associated with velocities larger than the mean. However, this is also the place where the high velocity layer in the lower crust defined in Luosto [1997] is the thickest. A full interpretation of the data recorded during the deep seismic SVEKALAPKO experiment is our next planned investigation.

Even though we need to refine our inversion of real data, in particular for a better estimate of the actual error in the velocity model, our method is reliable when applied to real seismograms.

3.2.7 Conclusion

We present a method for tomographic inversion of teleseismic surface wave phase information based on 2-D ray theory. The inversion of the time delays is only the first step of a longer process as the dispersion curves obtained at each grid point must subsequently be inverted to obtain a 3-dimensional shear-velocity model. Ray-based tomography was used to take into account the non-planarity of incoming wavefronts, and to stabilize the inversion we used *a priori* constraints on the smoothness of the velocity field and of the wavefronts.

The method is very robust in determining phase velocity maps in all synthetic examples. This robustness may be a consequence of using only the phase information of the signals, information which is more stable than the amplitudes of the seismograms. The numerical examples presented show that structures larger than 150 km can be obtained from phase information in the region containing the SVEKALAPKO receivers. Perturbations of the velocity model introduced by distorted wavefronts is weak. A 5° rotation of propagation direction superimposed on variations less than 30° over 100 km along the wavefront produces almost no artifact on the inverted velocity field inside the station network. The examples carried out using IBEM-computed seismograms allowed us to test both the process of time delay measurement and the inversion method. The quality of the result – even with a structure of a similar size to the wavelength – is very encouraging for their application on the SVEKALAPKO data set. The solution remains coherent with a signal to noise ratio down to 3.5, imposing objective preselection criteria for the inversion of the SVEKALAPKO data set. The inversion procedure remains stable when applied to real data, as demonstrated for the 60 s period fundamental-mode Rayleigh wave, using a subset of 48 events.

The ray tracing formulation has some major advantages. First, we can model both Rayleigh and Love waves. Second, we can easily implement discontinuities in the phase velocity model, which could be useful for imaging regional sharp structures such as the Tornquist Zone. Third, the mini-arrays of five and four stations in the middle of the SVEKALAPKO deep seismic experiment network can be used to measure locally the true propagation direction of the wavefronts, which subsequently can be used to constrain the inversion. The phase velocity beneath the mini-arrays can also be measured precisely and used as a further constraint. The lower limit of resolution depends on the inter station distance and on the wavelength. However, it results in a smoothing which is at least qualitatively predictable and can therefore be taken somewhat into account in the interpretation.

acknowledgments

We thank Tellervo Hyvönen for her help during the field work, as well as the numerous people who took part in it. The French participation received financial support from the 'Interieur de la Terre' program of INSU and used Litho-

scope and RLBM seismic stations. David Baumont provided the code used in the time-frequency filtering. Discussions with Guust Nolet and Michel Bouchon contributed to improving this paper, and two anonymous referees gave constructive comments to the original manuscript. The Editor provided a particularly careful correction of the English. The European Science Foundation financed the workshops of the SVEKALAPKO groups in Lammi, Finland. Most of the computations presented in this paper were performed at the Service Commun de Calcul Intensif de l'Observatoire de Grenoble (SCCI). We used SAC for the treatment of synthetic and real seismograms. Some figures where drawn using GMT and Xfig.

Bibliographie

Aki, K., A. Christoffersson & E. S. Husebye, 1977. Determination of 3-dimensional seismic structure of lithosphere, *J. Geophys. Res.*, **82**, 277–296.

Babuška, V., J. Plomerová & P. Pajdušák, 1988. Seismologically determined deep lithosphere structure in Fennoscandia, Proceedings in *Geologiska Föreningens i Stockholm Förhandlingar*, **110**, 380–382.

Barker, J. S., M. Campillo, F. J. Sánchez-Sesma, D. Jongmans & S. K. Singh, 1996. Analysis of wave propagation in the valley of Mexico from a dense array of seismometers, *Bull. Seism. Soc. Am.*, **86**, 1667–1680.

Bartels, R. H., J. C. Beatty & B. A. Barsky, 1988. *B-splines*, Hermès, Paris.

Bock, G. & the SVEKALAPKO Seismic Tomography Working Group, 2001. Seismic probing of Fennoscandian lithosphere, *EOS, Trans. Am. Geophys. Un.*, **82**, 621, 628–629.

Calcagnile, G., 1991. Deep structure of Fennoscandia from fundamental and higher mode dispersion of Rayleigh waves, *Tectonophysics*, **195**, 139–149.

Červený, V., 1989. Ray tracing in factorized anisotropic inhomogeneous media, *Geophys. J. Int.*, **99**, 91–100.

Červený, V., I. A. Molotov & I. Pšenčik, 1977. *Ray method in seismology*, Univerzita Karlova, Praha.

Cotte, N., H. A. Pedersen, M. Campillo, V. Farra & Y. Cansi, 2000. Off-great circle propagation of intermediate period surface waves as observed on a dense array in the French Alps, *Geophys. J. Int.*, **142**, 825–840.

Courant, R. & D. Hilbert, 1966. *Methods of mathematical physics*, Intersciences Publishers, Inc., New-York.

de Boor, C., 1978. *A practical guide to splines*, Springer-Verlag, New-York.

Deschamps, G. A., 1972. Ray techniques in electromagnetics, *Proc. IEEE*, **60**, 1022–1035.

Farra, V., 1990. Amplitude computation in heterogeneous media by ray perturbation theory: a finite element approach, *Geophys. J. Int.*, **103**, 341–354.

Farra, V., 1993. Ray tracing in complex media, *J. appl. Geophys.*, **30**, 55–73.

Farra, V. & R. Madariaga, 1987. Seismic waveform modeling in heterogeneous media by ray perturbation theory, *J. Geophys. Res.*, **92**, 2697–2712.

Farra, V. & R. Madariaga, 1988. Non-linear reflection tomography, *Geophys. J.*, **95**, 135–147.

Friederich, W., 1998. Wave-theoretical inversion of teleseismic surface waves in a regional network: phase-velocity maps and a three-dimensional upper-mantle shear-wave-velocity model for southern Germany, *Geophys. J. Int.*, **132**, 203–225.

Friederich, W. & E. Wielandt, 1995. Interpretation of seismic surface waves in regional networks: joint estimation of wave-field geometry and local phase velocity; Method and numerical tests, *Geophys. J. Int.*, **120**, 731–744.

Friederich, W., E. Wielandt & S. Stange, 1993. Multiple forward scattering of surface waves: comparison with an exact solution and Born single-scattering methods, *Geophys. J. Int.*, **112**, 264–275.

Friederich, W., E. Wielandt & S. Stange, 1994. Non-plane geometries of seismic surface wavefields and their implications for regional surface-wave tomography, *Geophys. J. Int.*, **119**, 931–948.

Herrmann, R. B., 1985. *Computer Programs in seismology, Volume III: Surface waves in plane layers*, Saint Louis University, Missouri.

Jeffreys, H & K. E. Bullen, 1940. Seismological Tables, *British Association for the Advancement of Science*, Gray Milne Trust (reprinted 1970).

Jobert, N. & G. Jobert, 1987. Ray tracing for surface waves, in *Seismic tomography with applications in global seismology and exploration geophysics*, G. Nolet (ed.), D. Reidel publishing company, Dordrecht, 275–300.

Korja, A., T. Korja, U. Luosto & P. Heikkinen, 1993. Seismic and geoelectric evidence for collisional and extensional events in the Fennoscandian Shield - implications for Precambrian crustal evolution, *Tectonophysics*, **219**, 129–152.

Lander, A. V. & A. L. Levshin, 1989. Recording, identification, and measurement of surface wave parameters, in *Seismic surface waves in laterally inhomogeneous Earth*, V. I. Keilis-Borok (ed.), Kluwer Academic Publishers, Dordrecht, 131–182.

Levshin, A. L., 1989. Surface waves in media with weak lateral inhomogeneity, in *Seismic surface waves in a laterally inhomogeneous Earth*, V. I. Keilis-Borok (ed.), Kluwer Academic Publishers, Dordrecht, 35–69.

Levshin, A. L. & K.-A. Berteussen, 1979. Anomalous propagation of surface waves in the Barents Sea as inferred from NORSAR recordings, *Geophys. J. R. astr. Soc.*, **56**, 97–118.

Luosto, U., 1990. Seismic data from the northern segment of the EGT and from the nearby profiles, in *The European Geotransverse (EGT) Project, data compilations and synoptic interpretation*, R. Freeman & St. Mueller (eds.), 53–63.

Luosto, U., 1997. Structure of the Earth's crust in Fennoscandia as revealed from refraction and wide-angle reflection studies, *Geophysica*, **33**, 3–16.

Marquering, H. & R. Snieder, 1996. Shear-wave velocity structure beneath Europe, the northeastern Atlantic and western Asia from waveform inversions including surface-wave mode coupling, *Geophys. J. Int.*, **127**, 283–304.

Marquering, H., R. Snieder & G. Nolet, 1996. Waveform inversions and the significance of surface-wave mode coupling, *Geophys. J. Int.*, **124**, 258–278.

Maupin, V., 1988. Surface waves across 2D structures: a method based on coupled local modes, *Geophys. J.*, **93**, 173–185.

McMechan, G. A. & M. J. Yedlin, 1981. Analysis of dispersive waves by wave field transformation, *Geophysics*, **46**, 869–874.

Nolet, G., 1987. Seismic wave propagation and seismic tomography, in *Seismic tomography with applications in global seismology and exploration geophysics*, D. Reidel publishing company, Dordrecht.

Nolet, G., 1990. Partitioned waveform inversion and two-dimensional structure under the Network of Autonomously Recording Seismographs, *J. Geophys. Res.*, **95**, 8499–8512.

Nur, A. 1987. Seismic rock properties for reservoir descriptions and monitoring, in *Seismic tomography with applications in global seismology and exploration geophysics*, G. Nolet (ed.), D. Reidel publishing company, Dordrecht, 203–237.

Pedersen, H. A., F. J. Sánchez-Sesma & M. Campillo, 1994. Three-dimensional scattering by two-dimensional topographies, *Bull. Seism. Soc. Am.*, **84**, 1169–1183.

Pedersen, H. A., V. Maupin & M. Campillo, 1996. Wave diffraction in multi-layered media with the Indirect Boundary Element Method: application to 3-D diffraction of long-period surface waves by 2-D lithospheric structures, *Geophys. J. Int.*, **125**, 545–558.

Pollitz, F. F., 1999. Regional velocity structure in northern California from inversion of scattered seismic surface waves, *J. Geophys. Res.*, **104**, 15043–15072.

Poupinet, G., W. L. Ellsworth & J. Fréchet, 1984. Monitoring velocity variations in the crust using earthquake doublets: an application to the Calaveras fault, California, *J. Geophys. Res.*, **89**, 5719–5731.

Simons, F. J., A. Zielhuis & R. D. van der Hilst, 1999. The deep structure of the Australian continent from surface wave tomography, *Lithos.*, **48**, 17–43.

Snieder, R., 1988a. Large-scale waveform inversion of surface waves for lateral heterogeneity, 1. Theory and numerical examples, *J. Geophys. Res.*, **93**, 12055–12065.

Snieder, R., 1988b. Large-scale waveform inversion of surface waves for lateral heterogeneity, 2. Application to surface waves in Europe and the Mediterranean, *J. Geophys. Res.*, **93**, 12067–12080.

Tarantola, A., 1987. *Inverse problem theory: methods for data fitting and parameter estimation*, Elsevier, Amsterdam.

Tromp, J. & F. A. Dahlen, 1992. Variational principles for surface wave propagation on a laterally heterogeneous Earth – II. frequency-domain JWKB theory, *Geophys. J. Int.*, **109**, 599–619.

Tromp, J. & F. A. Dahlen, 1993. Surface wave propagation in a slowly varying anisotropic waveguide, *Geophys. J. Int.*, **113**, 239–249.

van der Lee, S., 1998. Observations and origin of Rayleigh-wave amplitude anomalies, *Geophys. J. Int.*, **135**, 691–699.

Yanovskaya, T. B., 1996. Ray tomography based on azimuthal anomalies, *Pure appl. Geophys.*, **148**, 319–336.

Yanovskaya, T. B., E. S. Kizima & L. M. Antonova, 1998. Structure of the crust in the Black Sea and adjoining regions from surface wave data, *J. Seismology*, **2**, 303–316.

Zielhuis, A. & G. Nolet, 1994. Shear-wave velocity variations in the upper mantle beneath central Europe, *Geophys. J. Int.*, **117**, 695–715.

Chapitre 4

Structure lithosphérique moyenne

Soumis à *Earth and planetary Science Letters*

Layered lithospheric mantle in the central Baltic Shield from surface wave and xenolith analysis

M. Bruneton[1], H. A. Pedersen[1], P. Vacher[2], I. T. Kukkonen[3], N. T. Arndt[4], S. Funke[5], W. Friederich[5], V. Farra[6] and the SVEKALAPKO Seismic Tomography Working Group

[1]Laboratoire de Géophysique Interne et Tectonophysique, Obsevatoire des Sciences de l'Univers de Grenoble, France.

[2]Laboratoire Géophysique et Planétologie, Université de Nantes, France

[3]Geological Survey of Finland.

[4]Laboratoire de Géodynamique des Chaînes Alpines, Obsevatoire des Sciences de l'Univers de Grenoble, France.

[5]Institut für Geophysik der Stuttgart, Germany

[6]Département de Sismologie, Institut de Physique du Globe de Paris, France.

Résumé

Les études sismologiques régionales permettent d'obtenir des informations sur la structure du manteau supérieur. Les xénolites apportent des informations directes mais ells ne sont pas forcément représentatives de l'ensemble de la zone d'étude. Nous avons inversé les données large-bande de l'expérience de sismologie passive du projet SVEKALAPKO – Bouclier Balte – pour obtenir un modèle moyen de vitesse des ondes S avec la profondeur. Ce modèle est très bien contraint, excepté pour la croûte où nos données ne sont pas discriminantes. Les vitesses obtenues sont 4% plus rapides que des modèles moyens de Terre pour le manteau supérieur jusqu'à 250 km de profondeur. Nous n'observons pas de zone à moindre vitesse. Ce modèle d'origine sismologique est ensuite comparé à des profils de vitesse théoriques calculés à partir de compositions de xénolites. L'accord est très bon entre 150 et 300 km de profondeur pour les compositions de lherzolites et harzburgites provenant de kimberlites de Finlande. Pour des profondeurs plus

superficielles notre modèle d'origine sismologique donne des vitesses trop lentes par rapport aux modèles pétrologiques. Nous observons également un gradient de vitesse positif avec la profondeur, alors qu'une composition homogène sur tout le manteau lithosphérique entraîne un fort gradient négatif. Nos données peuvent être expliquées par une stratification chimique de la lithosphère: une composition donnant des vitesses lentes sous le Moho, remplacée progressivement par un manteau de composition normale de péridotite continentale. Plusieurs compositions semblent possibles pour le manteau superficiel: des péridotites métasomatisées, des éclogites, des résidus de formation des granitoïdes par fusion partielle de la croûte, ou des cumulats issus de la différentiation d'un magma picritique.

Regional seismic studies provide indirect information on the structure of the upper mantle, xenoliths on the other side give direct information but on a small portion of the study region only. The whole broadband data set of the deep-seismic experiment of the SVEKALAPKO project – in the central Baltic shield – is inverted to get a regional average shear-wave velocity model with depth. This model is very well constrained except for the crust where our dataset is not discriminative. The obtained model is approximately 4% faster than standard Earth models for the upper mantle down to 250 km depth. It does not show a clear low velocity zone that could define the base of the lithosphere. We compare our seismically derived shear-wave velocities to models derived from the composition of several mantle xenoliths. The agreement is good for depths between 150 and 300 km and for the compositions of lherzolite and harzburgite samples found in Finnish kimberlites, especially for the depth of origin of the xenoliths between 160 and 240 km. For shallower depths our seismically derived velocities are too slow compared to the petrological models, and they exhibit a positive gradient in this interval where a homogeneous composition should lead to a definite negative gradient. Our data could be explained by a chemical layering of the lithospheric mantle, with a composition giving slower velocities at the top, gradually replaced

by a more normal composition of continental peridotite toward tho bottom of the lithosphere. Possible candidates for the slow composition of the shallower mantle are metasomatized peridotite, eclogitic material, restite of granitoid formation from intracrustal melting or cumulate of picritic magma differentiation.

4.1 Introduction

Understanding the growth and stabilization of the earliest continents remains a challenge in Earth sciences. The development of thick lithospheric keels seems to have protected the continental crust against recycling in the mantle, but the mechanism and the timing of the stabilization of these continental roots remains largely unknown. To answer these questions, a more complete knowledge of the structure and composition of the cratonic lithosphere is required. Seismic studies can provide information on the present structure of the mantle in terms of seismic velocities and lateral variations [see for example in South Africa, James *et al.*, 2001]. Studies of mantle xenoliths are a good complement as they can provide a direct sampling of the mantle at the time the xenoliths were at their original location [Boyd, 1989; Pearson *et al.*, 2002]. The combination of the two approaches helps understanding the history and evolution of continents. However, the seismic models are rarely sufficiently well constrained to provide reliable constraints on mantle composition. The SVEKALAPKO seismic experiment in the Baltic shield is an exceptional opportunity to obtain well-constrained absolute seismic velocities in a shield area.

The Baltic shield consists of an Archean nucleus – the Karelian province – flanked to the north-east and south-west by late Archean to Proterozoic mobile belts – respectively the Lapland-Kola and Svecofennian domains [Gorbatschev & Bogdanova, 1993]. Its formation started some 3.5 Ga ago and continued through the Archean and Proterozoic with several orogenies, continental extensions and accretions. The last recorded thermic events are the intrusion of the Rapakivi

granitoids [1.65-1.54 Ga Korja *et al.*, 1993]. This composite craton, uncovered by sediments and without noticeable reworking since Proterozoic times, was chosen as one of the investigations of the EUROPROBE program [Gee & Zeyen, 1996]: the SVEKALAPKO project [Hjelt & Daly, 1996].

As part of this large European project, a two-dimensional seismic network was installed in southern Finland, which is located in the central part of the Baltic Shield [Bock & SVEKALAPKO Seismic Tomography W. G., 2001]. It operated for 8 months between summer 1998 and spring 1999. The network was composed of 144 seismic stations, 46 equipped with broadband sensors (43 CMG3 and STS2 with cut-off periods of 90 and 100 s, and 3 CMG40 with cut-off periods of 40 and 60 s, see figure 4.1). The concentration of 46 broadband seismic stations on a 500×800 km^2 area in the center of a shield provides a unique opportunity to obtain a very well constrained model of the local average shear-wave velocity with depth.

We interpret the arrival time of teleseismic fundamental mode Rayleigh wave recorded by the 46 broadband stations. Using a newly developed surface wave tomography [Bruneton *et al.*, 2002] we obtain a 1D average shear-wave velocity model with depth for the central Baltic shield. The presence of kimberlite pipes containing mantle xenoliths in the same area [Kukkonen & Peltonen, 1999] makes it possible to compare petrologically and seismically derived velocities as the xenoliths provide constraints on the compositions for the lithospheric mantle in the area.

4.2 Average dispersion curve

We invert the broadband data of the SVEKALAPKO deep seismic experiment for an average phase velocity dispersion curve using the procedure of Bruneton *et al.* [2002]. This method is based on 2-dimensional paraxial ray tracing and aims at calculating the phase velocities that best explain the arrival time of the surface

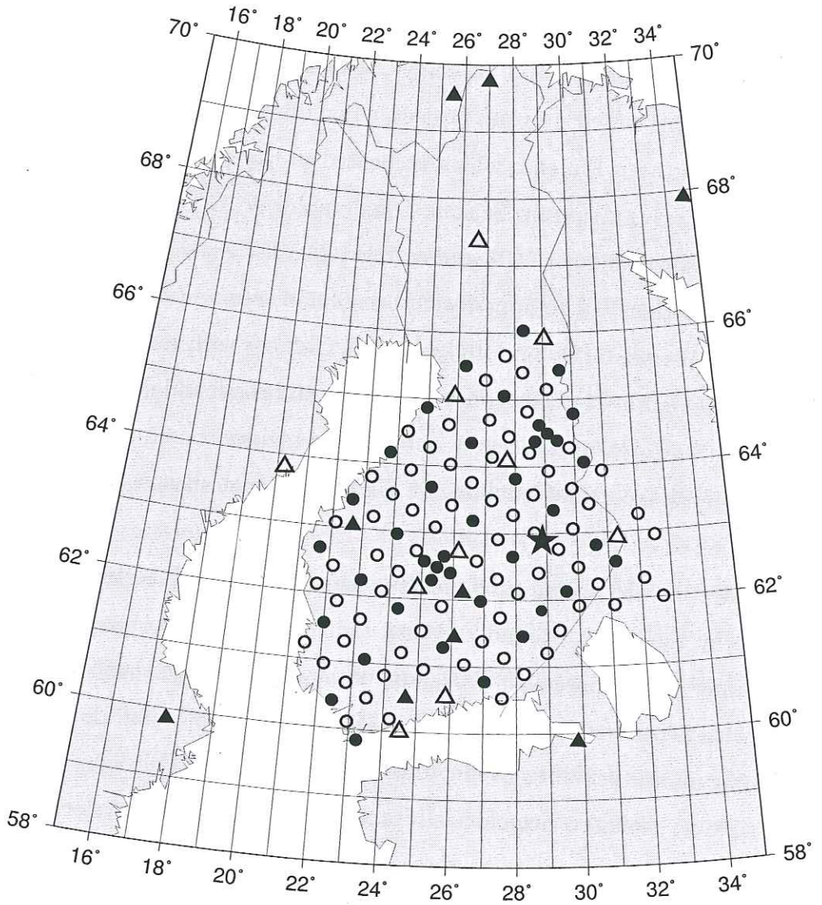

FIG. 4.1 – *Network of seismic stations of the deep seismic experiment of the SVEKALAPKO project; circles: temporary stations; triangles: permanent stations; black signs: broadband sensors; open signs: short periods (including 3 CMG40 40-60 s that were used in the present study); the black star gives the position of the Eastern Finland Kimberlites where mantle xenoliths were sampled.*

waves at all the stations in the array. We use only very high quality data, and we restrict our analysis to the fundamental mode Rayleigh waves. The novelty of the method is that we take into account the non planarity of incoming wavefronts. As the phase velocity depends on the frequency, one inversion per frequency is necessary. This method was developed to invert for lateral variations of phase velocity under a broadband array. To obtain the average velocity beneath the array we impose a constant velocity over the whole area for each frequency, but we still allow for non-plane incoming waves as nearby heterogeneities may distort the wavefronts.

Although the cut-off period of most of the seismic stations is 90-100 s, it is possible to interpret the data for the period range 10.5–190 s. A severe selection procedure of the data allow to retrieve reliable information from the less sensitive part of the seismogramms. For example we interpret only the part of each seismogram having a signal to noise ratio larger than 4. The number of data inverted is maximum for 22.5 s period with 1856 arrival times and falls to 557 at 190 s. At shorter periods the noise level increases and only 478 data times have a sufficient quality at 10.5 s period. The dispersion curve obtained from this data set is presented in figure 4.2 with its error bars. The computed error bars are proportional to the mathematical *a posteriori* covariance and conversely proportional to the number of data used for each period.

4.3 Inversion for shear-wave velocity

We then invert the average dispersion curve to obtain an average model of the shear-wave velocity with depth. This inversion follows a linearized method that allows to consider independent layers each filled by a continuous medium [Maupin & Cara, 1992]. We use the program package developed by Saito [1988] for the direct modeling and computation of the partial derivatives. The inversion algorithm is that of Tarantola & Valette [1982], minimizing the square of the

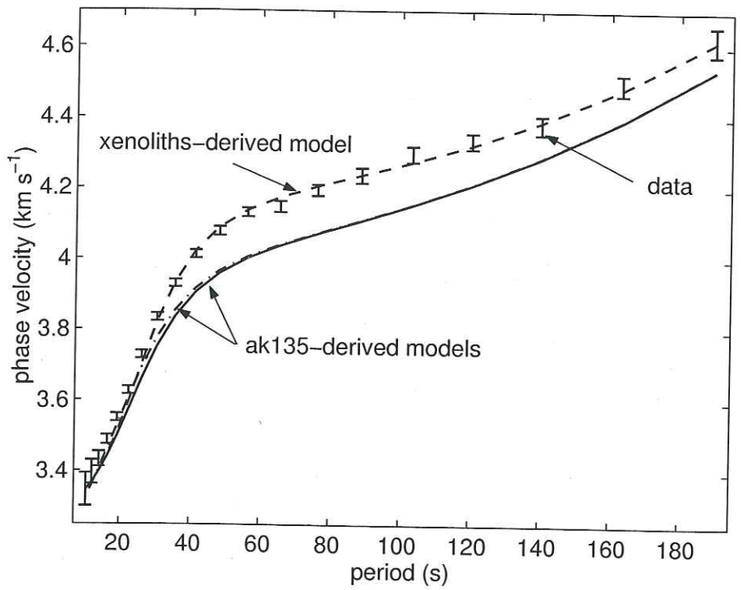

FIG. 4.2 – *Regional average dispersion curve (error bars), together with the dispersion curves of three different initial models for the inversion (solid line: ak135-derived model with 3-layer crust; dash-dotted line ak135-derived model with 4-layer crust; dashed line: xenoliths-derived model).*

difference between the predicted and observed phase velocities. The inversion model contains the shear-wave velocities only, P-wave velocities, densities and depths of the interfaces are kept unchanged during the inversion. The variation with depth of the P-wave velocities and densities are set to that of the initial model.

The variations in the continuous part of the model are governed by the definition of a correlation function. As in Lévêque *et al.* [1991] we use a Gaussian function whose width can be varied to choose the smoothness within each continuous part of the model. The correlation length is defined as the half width of the Gaussian for the 60% confidence interval. To reduce the non-uniqueness of the problem we choose a large correlation length of 100 km. The *a priori* error in the initial velocity model is set to 4%, allowing large variations from the initial model. These two parameters control the smoothness of the result and the width of the error bars. Our inversion is not capable of resolving steps in the continuous part of the velocity model.

Our shear-wave velocity model is constructed from surface waves of wavelengths between 40 and 900 km. Because of anelasticity in the Earth the seismic velocities depend on the frequency and a correction is necessary to compare with velocities obtained using different methods. The correction is made according to equation (5.81) of Aki & Richards [2002], using a reference frequency of 1 Hz:

$$V(z)_{\omega_1} = V(z)_{\omega_2}\left[1 + \frac{1}{\pi Q(z)} ln\left(\frac{\omega_1}{\omega_2(z)}\right)\right] \tag{4.1}$$

where $\omega_1 = 1$ Hz and $\omega_2(z)$ is a period representative of the surface waves that sample the medium at the depth z. The thickness of the lithosphere in the Baltic Shield is thought to be at least 250 km Kukkonen *et al.* [2003]. We therefore considered a two-layers Q model, following the standard Earth model ak135-f [Montagner & Kennett, 1996]: Q=600 for the crust and Q=400 for the lithosphere assumed to extend as deep as 300 km.

4.3.1 Resulting shear-wave velocity model

The initial shear-wave velocity model we use for the inversion derives from the standard Earth model ak135 [Kennett *et al.*, 1995] for the mantle part. The crustal structure is based on the work by Sandoval *et al.* [2003]. By a new interpretation of controlled source seismic profiles data, they obtain a 3D model of the P-wave velocity crustal structure, whose main feature is the Moho depth which vary between 38 and 64 km in the area of the SVEKALAPKO array. The thickest part of the crust exhibits a high-velocity lower crustal layer. We use here an average crustal thickness of 51.2 km for the region under the array and put the top of the high velocity lower crust at 35 km depth. The crust above 35 km is arbitrarily separated in two equally thick layers.

This initial model is plotted in figure 4.3, its associated dispersion curve is plotted in figure 4.2 and in the insert of figure 4.3. The phase velocities are 0.1 km.s^{-1} lower than the data for most periods, which is a reliable indication that the mantle has higher shear-wave velocities than ak135.

The model obtained after inversion is plotted in figure 4.3, it will be referred to as model 1. The fit to the dispersion curve is shown in the insert of figure 4.3. The obtained phase velocities are compatible with the observed dispersion curve for all periods. The root mean square fit to the data dispersion curve equals 0.0095 km.s^{-1}.

The shear-wave velocity model presents velocities 4% higher than standard Earth model ak135 [Kennett *et al.*, 1995] or PREM [Dziewonski & Anderson, 1981] for the mantle down to 250 km. There is no resolvable low velocity zone, so the base of the lithosphere is not clearly defined in this shear-wave velocity model.

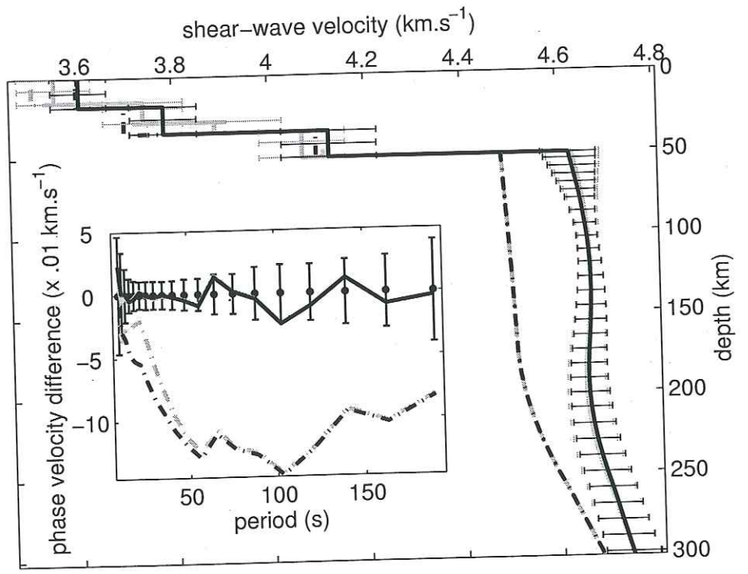

FIG. 4.3 – *Shear-wave velocity models: influence of the crustal structure. Dashed lines: initial models for the inversions; solid lines: final models; black: 3-layer crust; grey: 4-layer crust. Insert: phase velocity dispersion curves with respect to the data. Error bars: data; dashed lines: initial models; solid lines final models; black: 3-layer crust; grey: 4-layer crust.*

4.3.2 Influence of the input parameters

To test the influence of the input parameters for the inversion (correlation length and *a priori* error in the velocity model) we run a second inversion step varying the correlation length between 100 and 20 km, and the *a priori* error between 2 and 4%.

The difference in rms fit to the data dispersion curve for these inversions is insignificant as it varies between 0.0089 and 0.0095 km.s^{-1}. The average discrepancy in shear-wave velocity compared to the result of the first trial is less than 0.5% for all models.

Increasing the *a priori* error or decreasing the correlation length leads to larger variations in shear-wave velocity and larger *a posteriori* error bars. Reducing the smoothing of the model also results in an upward translation of the 'S' shape of the velocities in the mantle. As the velocity variations remain small, this translation does not alter the overall aspect of the model.

We choose a value of 4% for the *a priori* error in the velocity model and 100 km for the correlation length as a good compromise between having reasonable error bars and not being too closely influenced by the initial model.

The final error bars obtained on the shear-wave velocity model (figure 4.3) may seem quite large, but a model composed of the higher velocities for each depth would not fit the data: high velocities for one particular depth should be compensated by low velocities for adjacent depths.

4.3.3 Influence of the crustal structure

An interpretation that combines seismic and gravity data in the same region led Kozlovskaya *et al.* [submitted] to define a 4-layered crust. Based on their results, we inverte the data using a different initial model composed of the same ak135-based mantle structure and of four crustal layers of the following thicknesses (from top to bottom): 15, 13, 7 and 16.2 km.

The result (model 2) is plotted in figure 4.3. The rms fit to the data is only slightly better than for model 1 (0.0085 km.s^{-1}). The crustal velocities are noticeably modified following the number and thickness of the layers but the final mantle structure is unchanged. We conclude that our data can not resolve the structure of the crust. However the definition of different crustal layers does not alter the result obtained for the mantle structure.

The inversion procedure we use does not invert for the depth of the interfaces. The fixed Moho depth is quite a strong constraint on the shear-wave velocity model. We tested the effect of an increase of the Moho depth by 3 km. It results in an increase of the velocity of the lower crustal layer of 0.75%, and an increase of the mantle velocities of 0.5% immediately below the Moho and lowering gradualy to be zero around 100-120 km. Such a small variation in the shallow mantle does not influence the overall shape of the velocity profile, and a larger variation of the Moho depth would not lead to a reasonable physical model.

4.3.4 Influence of the initial mantle structure

We also change the mantle structure of the initial model keeping a 3-layered crust. The second initial mantle model is based on the study of eastern Finland mantle xenoliths by Kukkonen *et al.* [2003]. The computations are based on the average mineralogical composition of the xenoliths and on a local model for the geotherm.

The resulting model 3 is shown in figure 4.4. The dispersion curve of this initial model (figure 4.2 and insert of figure 4.4) is very close to the data for all the measured interval. After inversion the rms fit to the phase velocity data is 0.0093 km.s^{-1}.

The final models 1 and 3 are quite similar in particular at the depths of the origin of the xenoliths. However, there are differences at 50-80 km depth where higher velocities of model 3 as compared to model 1 are compensated by lower

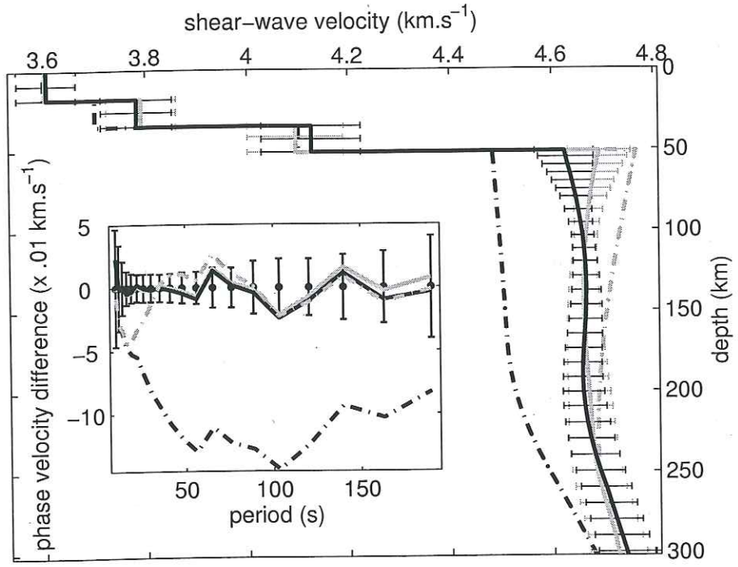

FIG. 4.4 – *Shear-wave velocity models: influence of the initial mantle structure. Dashed lines: initial models for the inversions; solid lines: final models; black: mantle model based on ak135 [Kennett et al., 1995]; grey: mantle model based on xenoliths [Kukkonen et al., 2003]. The insert shows the corresponding phase velocity dispersion curve in km.s^{-1} with respect to the data.*

velocities in the lowermost crust. It is not obvious to choose between the two models as the velocity variations are so small that they are not resolved by other seismic data.

Even though the shallowest mantle velocities are slightly dependent on the initial model, they can still not exceed approximately 4.7 km.s^{-1} immediately below the Moho. The mantle velocities from 100 to 300 km are particularly robust. Conversely the crustal structure is not well resolved by our data set.

4.4 Comparison with xenoliths-derived velocities

Interpretation of seismic velocities in terms of the petrology and chemistry of the mantle is one of the current challenges in earth sciences. We pointed out in the previous section that our data dispersion curve is almost compatible with xenolith-based computations by Kukkonen *et al.* [2003] (figure 4.4). To get a more precise comparison between the observed seismic velocities and the computations based on the petrology, we use the original description of the samples [Kukkonen & Peltonen, 1999].

The seismic velocities depend on the density and elastic parameters, which in turn depend on the rock composition, the orientation of minerals and temperature and pressure conditions. Reference values for the elastic parameters of the major minerals as well as their pressure and temperature derivatives are known from laboratory experiment [see Table A1 of Goes *et al.*, 2000]. The geotherm used is that of Kukkonen *et al.* [2003], it is calculated from a two-dimensional conductive model along a seismic profile in the kimberlite province [Kukkonen & Jõeleht, 1996; Kukkonen & Peltonen, 1999]. The boundary condition used in the mantle for this geotherm is a constant heat flow density of 12 mW.m^{-2} at 250 km depth. It is in satisfactory agreement with the thermobarometry of the xenolith samples

(less than 100°C discrepancy except for three samples). The overall velocity of the rock is calculated using the Voigt-Reuss-Hill average, which gives the same average values as the more accurate Hashin-Shtrikman averaging but is easier to compute [Vacher *et al.*, 1996]. We also improve the method to compute seismic velocity from the rock compositions by taking into account anharmonicity and anelasticity following Goes *et al.* [2000].

4.4.1 Fit for composition of normal lithospheric mantle

The compositions 1 to 3 (table 4.1) correspond to mantle xenoliths sampled in the eastern Finland kimberlite cluster [Kukkonen & Peltonen, 1999]. Compositions 1 and 2 (harzburgites) are good candidates for highly depleted Archean lithosphere; composition 3 (lherzolite) is less depleted and may correspond to Proterozoic lithosphere. figure 4.5 shows the Vs profiles obtained from these compositions with the possible variations induced by uncertainties in the elastic parameters, togeather with our seismic model 1 corrected with different values of the quality factor Q.

A good agreement exists between our surface-wave derived models and all three compositions for depths between 150 and 300 km. Above 100 km the agreement disappears: all composition-based shear-wave velocity profiles present systematically higher velocities. Moreover, the computed velocities present a negative gradient with depth for the lithosphere, whereas the profiles derived from surface waves present a zero or slightly positive gradient, negative only for the shallower 50 km of the mantle for one of the two the initial models. The high velocities of the theoretical composition-based profiles of normal mantle rock compositions for the shallower 50-80 km of the mantle are incompatible with our data. To reconcile the seismic observations with the petrology using the attenuation factor, we would need a Q model increasing with depth which corresponds neither to seismological observations, nor to interpretation of the physical origin of the

	rock type	ol	opx	cpx	gt	sp	amph	phl	referen ce
1	gt sp harzburgite	70.0	25.2	0.9	2.7	-	-	-	Kukkonen & Peltonen [1999] , sample L48
2	gt harzburgite	86.1	10.4	1.0	2.5	-	-	-	Kukkonen & Peltonen [1999], s ample L29
3	gt lherzolite	64.2	26.4	8.1	1.2	-	-	-	Kukkonen & Peltonen [1999], sa mple L66
4	gt ol websterite	14.3	77.3	7.3	1.0	-	-	-	Kukkonen & Peltonen [1999], sample L29
5	gt wehrlite	75.6	1.5	18.2	4.7	-	-	-	Kukkonen & Peltonen [1999], samp le L44
6	amph peridotite	59.0	21.0	15.0	-	2.0	3.7	-	Ionov *et al.* [1992]
7	amph peridotite	50.0	17.0	21.0	-	1.5	10.0	-	Nielson *et al.* [1 993]
8	phl peridotite	53.0	-	32.0	-	1.0	-	13.0	Edgar *et al.* [1989]
10	granitoid magma restite	30.0	-	60.0	10.0	-	-	-	Arndt & Goldstein [1989]
		cpx		gt	ms	jd	qz	ky	
9	eclogite	32.0		36.0	6.0	17.0	3.0	6.0	Bousquet *et al.* [1997]

TAB. 4.1 – *Different composition used to compute the shear-wave velocities presented in figure 4.7, % in volume. ol: olivine; opx: orthopyroxene; cpx: clinopyroxene; gt: garnet; sp: spinel; amph: amphibole; phl: phlogopite; ms: muscovite; jd: jadeite; qz: quartz; ky: kyanite. Compositions 1 to 5 correspond to mantle xenoliths from the Fennoscandian shield; compositions 6 to 8 are various extremely hydrated peridotites; composition 9 is an eclogite from the lower crust; and composition 10 is the hypothetical residue of granitoid formation.*

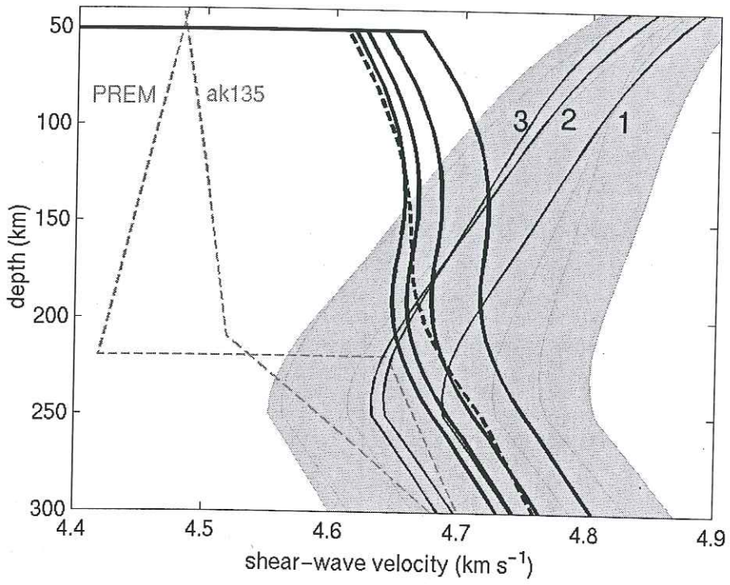

FIG. 4.5 – *Comparison between shear-wave velocity models obtained from surface wave (model 1) and from compositions of normal lithospheric rocks. Bold solid lines: models derived from the surface waves with different values of the quality factor for the upper mantle: from left to right Q=1000, 400, 200, 100; bold dashed line: model derived from surface waves corrected using the same Q(z) model as the composition-based calculations [model Q1 of Goes et al., 2000]; thin lines with associated shaded area: computations based on the rock composition 1 to 3 (see table 4.1). The grey dashed lines show two different standard Earth models: PREM [Dziewonski & Anderson, 1981], and ak135 [Kennett et al., 1995].*

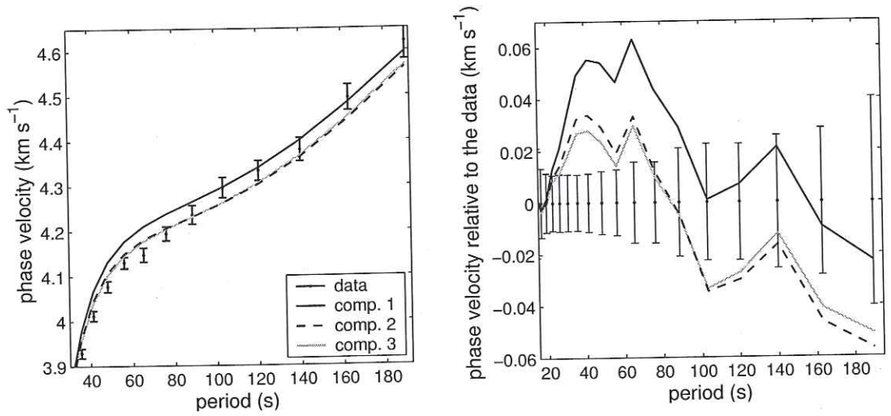

FIG. 4.6 – *Comparison between data phase velocities and computations based on rock compositions 1 to 3 (see Table 4.1).*

attenuation. In particular, values of Q lower than 100 for the shallowmost mantle are unlikely.

figure 4.6 shows the dispersion curves produced by the models of compositions 1 to 3, and the difference with our data dispersion curve. The petrologic models provide systematically too high phase velocities for the period range 30-70 s.

Only a small portion of the xenolith samples of eastern Finland originate from depths between 100 and 150 km and none comes from shallower than 100 km [Kukkonen & Peltonen, 1999]. All of the xenoliths from the 100-150 km interval are highly depleted, whereas the deeper samples are less depleted. This led Kukkonen & Peltonen [1999] to propose a stratification of the lithosphere with an upper part composed of depleted Archean lithosphere, and a lower part composed of Proterozoic underplated or subducted lithosphere not depleted since Proterozoic times.

The differences in velocities derived from the observed lherzolite and harzburgite compositions is not systematic and can not be resolved by a seismic study. Moreover, the observation that the degree of depletion increases toward the surface of the Earth can be explained by an increase in the percentage of partial melting in a rising column of mantle. It does not necessarily require layering of Archean and Proterozoic mantles.

4.4.2 Fit for exotic compositions

Figure 4.7 presents the shear-wave velocity models obtained from ten different rock compositions compared to our surface wave derived models 1 and 3. Compositions 4 and 5 are pyroxene-rich mantellic rocks sampled in eastern Finland and compositions 6 to 10 represent different rocks known to have slow seismic velocities.

The velocity computed from composition 4 (websterite) are comparable to those of compositions 1-3, they can not explain the slow upper layer. The presence

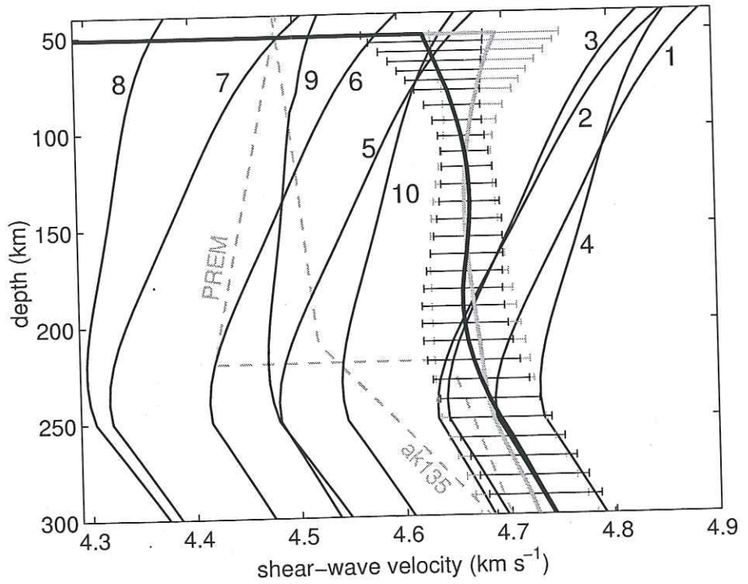

FIG. 4.7 – *Comparison between surface-wave derived mantle velocities (model 1: black thick lines, model 3: grey thick line), and computations based on rock composition (color lines, see table 4.1 for the compositions): 1 to 5: selected xenoliths from Eastern Finland [Kukkonen & Peltonen, 1999], 6 to 8: various hydrated peridotites [Ionov et al., 1992; Nielson et al., 1993; Edgar et al., 1989], 9: eclogite [Bousquet et al., 1997] and 10: residue of granitoid formation [Arndt & Goldstein, 1989]. The black dashed lines show two different standard Earth models: PREM [Dziewonski & Anderson, 1981], and ak135 [Kennett et al., 1995].*

of a certain amount of wehrlite (composition 5) could lower the velocity of the mantle, but large accumulations of such a rock of uncertain origin are unlikely.

Compositions 6 to 8 are strongly hydrated peridotites chosen to represent metasomitized rocks extreme [Ionov *et al.*, 1992; Nielson *et al.*, 1993; Edgar *et al.*, 1989]. They correspond to mantle material metasomatized to different degrees and by different fluids. All three compositions give too low velocities compared to our seismic model (figure 4.7). However composition 8 [phlogopite peridotite Edgar *et al.*, 1989], is interesting in that it produces a smaller negative gradient. If metasomatized peridotites reside in the uppermost mantle beneath southern Finland, the degree of metasomatization must be less than that in the samples we choose in the litterature.

We also plotted in figure 4.7 the shear-wave velocity of an eclogitic sample [composition 9, Bousquet *et al.*, 1997]. This profile is also slower than the observed velocities. But it is closer to our velocities than the hydrous peridotite and provides a smaller gradient than most other rocks. However, large proportion of peridotite material in the shallower mantle are unlikely.

Finally, we tested a composition (10) proposed by Arndt & Goldstein [1989]. It corresponds to the virtual restite of lower crust melting to form granitoid magmas. Following these authors, such a restite should sink down into the mantle due to a higher density than the surrounding crust, perhaps forming a layer at the top of the lithospheric mantle. This composition produces the shear-wave velocity profile which is the closest to our seismic model for depths shallower than 100 km, even if it is again too slow. A composition with slightly more garnet or less clinopyroxene would match the data.

4.5 Discussion and conclusions

We interpret the phase information of fundamental mode Rayleigh wave data of the SVEKALAPKO deep seismic experiment in terms of a regional average shear-

wave velocity model with depth. This model presents 4% higher velocities than standard Earth model ak135 [Kennett *et al.*, 1995] in the upper 200 km of the mantle. It does not show a clear low velocity zone that could allow us to define the base of the lithosphere.

By testing different initial models we conclude that the crustal structure is not resolved by our data. The velocity of the mantle down to 80 km depth is also somewhat uncertain as it may shift by 1.5% with different initial models. Independent knowledge of a well-constrained shear-wave velocity model for the crust would improve the resolution in the uppermost mantle.

The comparison of the seismically derived shear-wave velocity models with models computed from petrology leads to a good agreement for depths between 150 and 300 km. In particular, the fit with the velocity model computed from lherzolite and harzburgite xenoliths from eastern Finland kimberlite clusters is excellent for the depth of origin of the samples (160-240 km).

For shallower depths, the agreement between seismically and petrologically derived velocities is poor. The velocities seen by the surface waves above 100 km are too slow to be compatible with an hypothesis of homogeneous composition of the lithosphere with depth. Moreover their gradient with depth is slightly positive or negative, whereas it would be noticeably negative with a constant composition.

Most of the xenoliths come from 160-240 km depth: two of them are from 100-150 km, but none from shallower depths. The lack of direct sampling of the shallower mantle is wide-spread in cratonic areas (Ionov, personal communication). This uneven vertical sampling of the lithosphere by the kimberlite magmas may be due either to weak material or different ascent mechanism of the Kimberlite magma within the shallowmost mantle as compared to the underlying layers.

To explain our observations we need a layered lithospheric mantle composed of normal cratonic peridotite under a zone of anomalous and slow material. At least two mechanisms would make it possible to build such a layered lithosphere

based on metasomatism or crust-mantle interaction.

4.5.1 Model with metasomatism

A combined analysis by Pearson *et al.* [2002] of platinum group element and Re-Os isotope of mantle peridotites from South Africa provided some ideas on the timing of the stabilization of the craton. These authors suggest that the formation of the lithosphere started at the same time as the most ancient crustal rocks, but large-scale preservation of Archean continental masses was effective only in Neoarchean times, 500 Ma to 1 Ga later. The final stabilization was caused by the formation of a substantial, buoyant, rigid lithospheric keel, associated with voluminous mafic magmatism. Large-scale modifications of the lithospheric mantle are also reported in the North China craton Gao *et al.* [2002].

Concerning the Baltic Shield, Brueckner *et al.* [2002] observe different geochronologic ages recorded in peridotites of the Norwegian Caledonides. Re-Os isotops measurements lead to an Archean age for the original depletion event that formed the lithospheric mantle, followed by an important metamorphic event during mid-Proterozoic, and further perturbations during the Caledonian orogeny. The primary Archean lithospheric mantle could have become highly metasomatized in late Archean or early Proterozoic. New interpretation of the geology of the Baltic shield yields a complex history for the formation of the Svecofennian domain [Nironen *et al.*, 2002] where two thirds of our seismic array were installed. A succession of subductions, collisions, accretions of island-arcs, terrains and micro-continents could have introduced the fluids necessary to metasomatize the mantle. Such a tectonic history could also add some eclogitic material to the mantle. Afterward, the stabilization of the craton would have been associated with the formation of a thick lithosphere preserving both the crust and the metasomatized primary mantle in the mid-Proterozoic.

However this scenario probably would produce two distinct layers: an upper

part composed of metasomatized peridotites mixed with eclogite, and a lower part of secondary lithospheric mantle having noticeably higher velocities. This is not consistent with our observation of continuous variation of velocity, but the smoothness of the obtained model is partly conditioned by the inversion parameters.

4.5.2 Model with crust-mantle interaction

An alternative explanation is proposed by Arndt & Goldstein [1989]: two processes may produce ultramafic restites or cumulates at the top of the lithospheric mantle. First, dense picritic magmas may be trapped at the base of the crust, where they differentiate to form layered sills with gabbroic upper parts and olivine + pyroxene cumulate lower parts. The gabbroic layers are integrated into the crust while the cumulates return to the mantle due to their high density. Second, granitoid magmas formed during intracrustal melting leave dense residues which may also return to the mantle. These processes yield an anomalous upper lithosphere layer more fertile than normal cratonic lithosphere, and which is likely to have a continuous transition with the underlying lithospheric mantle.

As an example we computed the relative quantity of material of compositions 2 (harzburgite) and 10 (granitoid residues) needed to obtain a velocity model averaged from our surface waves derived models 1 and 3. The proportion of granitoid residues present immediately underneath the Moho would be larger than 90%, and would decrease to approximately 35% at 150 km depth. The proportions are identical whether we average the velocities or the inverse of the velocities.

This scenario could also explain the anomalous crust of central Finland which reaches 65 km thickness at places with a very high velocity lower crust but without topographic and gravity variations [Sandoval *et al.*, 2003; Kozlovskaya *et al.*, submitted]. If the lithospheric mantle was frozen before the complete separation

of the mantle residues from the crust, the high-velocity lower crust could be formed by layered sills of alternating crustal and mantle materials.

To further improve these models, it is necessary to constrain the absolute P-wave velocities in the mantle, as P- and S-wave velocities behave quite differently to compositional variations.

acknowledgments

We thank Tellervo Hyvönen for her help during the field work, as well as the numerous people who took part in it. The French participation received financial support from the Intérieur de la Terre program of INSU and used Lithoscope and RLBM seismic stations. We thank Valérie Maupin and Jean-Jacques Lévêque for the dispersion-curve inversion code and Senen Sandoval for the Moho depth model. The European Science Foundation financed most of the workshops of the SVEKALAPKO project. Most of the computations presented in this paper were performed at the Service Commun de Calcul Intensif de l'Observatoire de Grenoble (SCCI). We used SAC for the treatment of the seismograms; figure 4.1 was drawn using GMT.

Bibliographie

Aki, K. & P.G. Richards, 2002. *Quantitative Seismology*, second edition, University Science Books, Sausalito, California.

Arndt, N. T. & S. L. Goldstein, 1989. An open boundary between lower continental crust and mantle: its role in crust formation and crustal recycling, *Tectonophysics*, **161**, 201–212.

Bock, G. & the SVEKALAPKO Seismic Tomography Working Group, 2001. Seismic Probing of the Fennoscandian lithosphere, *EOS, Trans. Am. Geophys. Un.*, **82**, 621, 628–629.

Bousquet R., B. Goffé, P. Henry, X. Le Pichon & C. Chopin, 1997. Kinematic, thermal and petrological model of the Central Alps: Lepontine metamorphism in the upper crust and eclogitisation of the lower crust, *Tectonophysics*, **273**, 105–127.

Boyd, F. R., 1989. Compositional distinction between oceanic and cratonic lithosphere, *Earth Plant. Sci. Lett.*, **96**, 15–26.

Brueckner, H. K., D. A. Carswell, W. L. Griffin, 2002. Paleozoic diamonds within a Precambrian peridotite lens in UHP gneisses of Norwegian Caledonides, *Earth Planet. Sci. Lett.*, **203**, 805–816.

Bruneton, M., V. Farra, H. A. Pedersen & the SVEKALAPKO Seismic Tomography Working Group, 2002. Non-linear surface wave phase velocity inversion based on ray theory, *Geophys. J. Int.*, **151**, 583–596.

Dziewonski, A. M., & D. L. Anderson, 1981. Preliminary Reference Earth Model, *Phys. Earth Planet. Int.*, **25**, 297–356.

Edgard, A. D., F. E. Lloyd, D. M. Forsyth & L. R. Barnett, 1989. Origin of glass in upper mantle xenoliths from Quaternary volcanics of Gees, West Eifel, Germany, *Contrib. Mineral. Petrol.*, **103**, 277–286.

Gao, S., R. L. Rudnick, R. W. Carlson, W. F. McDonough & Y.-S. Liu, 2002. Re-Os evidence for replacement of ancient mantle lithosphere beneath the North China craton, *Earth Planet. Sci. Lett.*, **198**, 307–322.

Gee, D. G. & H. J. Zeyen (eds.), 1996. *EUROPROBE 1996 – lithosphere dynamics: origin and evolution of continents*, EUROPROBE secretariat, Uppsala University, Uppsala, Sweden.

Goes, S., R. Govers & P. Vacher, 2000. Shallow mantle temperatures under Europe from P and S wave tomography *J. Geophys. Res.*, **105**, 11153–11169.

Gorbatschev, R. & S. Bogdanova, 1993. Frontiers in the Baltic Shield., *Precambrian Res.*, **64**, 3-21.

Hjelt, S.-E. & J. S. Daly, 1996. SVEKALAPKO, evolution of Paleoproterozoic and Archean lithosphere, in *EUROPROBE 1996 – lithosphere dynamics: origin and evolution of continents*, D. G. Gee and H. J. Zeyen (eds.), EUROPROBE secretariat, Uppsala University, Uppsala, Sweden.

Ionov, D. A., U. Kramm & H. G. Stosch, 1992. Evolution of the upper mantle beneath the southern Baikal rift zone; an Sr-Nd isotope study of xenoliths from the Bartoy volcanoes, *Contrib. Mineral. Petrol.*, **111**, 235–247.

James, D. E., M. J. Fouch, J. C. VanDecar, S. van der Lee & the Kaapvaal Seismic Group, 2001. Tectospheric structure beneath southern Africa, *Geophys. Res. Lett.*, **28**, 2485–2488.

Kennett, B. L. N., E. R. Engdhal & R. Buland, 1995. Constraints on seismic velocities in the Earth from traveltimes, *Geophys. J. Int.*, **122**, 108–124.

Korja, A., T. Korja, U. Luosto & P. Heikkinen, 1993. Seismic and geoelectric evidence for collisional and extensional events in the Fennoscandian Shield – implications for

Precambrian crustal evolution, *Tectonophysics*, **219**, 129–152.

Kozlovskaya, E., S. Elo, S.-E. Hjelt, J. Yliniemi, M. Pirttijärvi & the SVEKALAPKO Seismic Tomography Working Group, submitted. 3D density model of the crust of southern and central Finland obtained from joint interpretation of SVEKALAPKO crustal P-wave velocity model and gravity data, *Geophys. J. Int.*.

Kukkonen, I. T. & A. Jõeleht, 1996. Geothermal modelling of the lithosphere in the central Baltic shield and its southern slope, *Tectonophysics*, **255**, 24–45.

Kukkonen, I. T. & P. Peltonen, 1999. Xenolith-controlled geotherm for the central Fennoscandian Shield: implications for lithospheric-asthenospheric relations, *Tectonophysics*, **304**, 301–315.

Kukkonen, I. T., K. Kinnunen & P. Peltonen, 2003. Mantle xenoliths and thick lithosphere in the Fennoscandian Shield, *Physics and Chemistry of the Earth*, **28**, 349–360.

Lévêque, J.-J., M. Cara & D. Rouland, 1991. Waveform inversion of surface wave data: test of a new tool for systematic investigation of upper mantle structures, *Geophys. J. Int.*, **104**, 565–581.

Maupin, V. & M. Cara, 1992. Love-Rayleigh wave incompatibility and possible deep upper mantle anisotropy in the Iberian peninsula, *Pure appl. Geophys.*, **138**, 429–444.

Montagner, J. P. & B. L. N. Kennett, 1996. How to reconcile body-wave and normal-mode reference Earth model? *Geophys. J. Int.*, **125**, 229–248.

Nielson, J. E., J. R. Budahn, D. M. Unruh & H. G. Wilshire, 1993 Actualistic models of mantle metasomatism documented in a composite xenolith from Dish Hill, California, *Geochim. Cosmochim. Acta*, **57**, 105–121.

Nironen, M., R. Lahtinen & A. Korja, 2002. Paleoproterozoic tectonic evolution of the Fennoscandian shield – comparison to modern analogues, in *Lithosphere 2002 – second symposium on the structure, composition and evolution of the lithosphere in Finland. Programme and extended abstracts, Espoo, Finland*, R. Lahtinen, A. Korja, K. Arhe, O. Eklund, S.-E. Hjelt and L. J. Pesonen (eds.), Institute of Seismology, University of Helsinki, report S-42, 95–97.

Pearson, D. G., G. J. Irvine, R. W. Carlson, M. G. Kopylova & D. A. Ionov, 2002. The development of lithospheric keels beneath the earliest continents: time constraints using PGE and Re-Os isotope systematics, in *The early Earth: physical, chemical and biological development*, C. M. R.Fowler, C. J. Ebinger & C. J. Hawkesworth (eds.), Geologycal Society, London, Special Publication, **199**, 65–90.

Saito, M., 1988. Disper 80: a subroutine package for the calculation of seismic modes solutions, in *Seismological Algorithms*, D. J. Doornbos (ed.), Academic Press, New-York.

Sandoval, S., E. Kissling, J. Ansorge & the SVEKALAPKO Seismic Tomography Working Group, 2003. High-resolution body wave tomography beneath the SVEKALAPKO array: I. a priori 3D crustal model and associated traveltime effects on teleseismic wavefronts, *Geophys. J. Int.*, **153**, 75–87.

Tarantola, A. & B. Valette, 1982. Generalized nonlinear inverse problems solved using the least square criterion, *Rev. Geophys. Space Phys.*, **20**, 219–232.

Vacher, P., A. Mocquet & C. Sotin, 1996. Comparison between tomographic structures and models of convection in the upper mantle, *Geophys. J. Int.*, **124**, 45–56.

Chapitre 5

Modèle lithosphérique tridimensionnel

Soumis à *Journal of Geophysical Research*

Complex lithospheric structure under the central Baltic Shield from surface wave tomography

M. Bruneton[1], H. A. Pedersen[1], V. Farra[2], N. T. Arndt[3], P. Vacher[4] and the SVEKALAPKO Seismic Tomography Working Group

[1]Laboratoire de Géophysique Interne et Tectonophysique, Obsevatoire des Sciences de l'Univers de Grenoble, BP 53, 38041 Grenoble cedex 09, France.

[2]Département de Sismologie, Institut de Physique du Globe de Paris, 4 Place Jussieu, 75252 Paris cedex 05, France.

[3]Laboratoire de Géodynamique des Chaînes Alpines, Obsevatoire des Sciences de l'Univers de Grenoble, BP 53, 38041 Grenoble cedex 09, France.

[4]Laboratoire Géophysique et Planétologie, Université de Nantes, France.

Résumé

La tomographie sismique à l'échelle régionale permet d'obtenir des informations importantes sur la structure des boucliers, et par suite, sur la formation et la stabilisation des continents anciens. La Fennoscandie – mieux connue sous le nom de bouclier Balte pour sa partie exposée – est un craton n'ayant pas subi d'événement tectonique depuis 1,6 Ga (intrusion des granitoïdes de Rapakivi). Il est composé de plusieurs domaines d'âge variant entre l'Archéen et le Protérozoïque. Le projet européen SVEKALAPKO comprend une expérience de sismologie de grande ampleur, prévue pour étudier le manteau supérieur du Bouclier Balte, en particulier la frontière entre l'Archéen et le Protérozoïque. Nous inversons les données télésismiques large-bande de cette expérience pour obtenir un modèle 3D en vitesse des ondes S jusqu'à 150 km de profondeur. Nous utilisons une méthode basée sur le tracé de rais et prenant en compte la courbure des fronts d'onde incidents. Nous observons des variations de vitesses de ± 3%. Les variations thermiques sous la Finlande sont faibles, il est donc nécessaire de faire intervenir des variations de composition des roches. Des vitesses rapides pour la croûte inférieure et le manteau superficiel sont associées à la région où le Moho est anormalement profond. Les lithosphères des domaines Archéen et Protérozoïque n'apparaissent pas différentes dans les cartes de vitesse des ondes S. Mais une classification des profils de vitesse en fonction de la profondeur permet de définir quatre familles principales et cinq intermédiaires que l'on peut corréler avec la géologie de surface. La comparaison de ces profils avec des vitesses calculées à partir de composition de xénolites implique à la fois des variations latérales et verticales de la minéralogie.

Regional seismic tomography provides valuable information on the structure of shields, thereby gaining insight to the formation and stabilisation of old continents. Fennoscandia (known as the Baltic Shield for its exposed part) is a composite craton for which the last recorded tectonic event is the intrusion of the Rapakivi granitoids around 1.6 Ga. A deep seismic experiment carried out as part of the European project SVEKALAPKO was designed to study the upper mantle of the Finnish part of the Baltic Shield, especially the boundary between Archean and Proterozoic domains. We invert the teleseismic broadband data using a ray-based method accounting for the curvature of wavefronts to obtain a 3D shear-wave velocity model. Our resolution allows an evaluation of lateral variations in velocities down to 150 km depth. The obtained model exhibits variations of up to ± 3% in S-wave velocities. As the thermal variations beneath Finland are small, these lateral variations are caused by different rock compositions. The most prominent feature of our 3D S-wave velocity model is high velocities in the lower crust and shallow mantle associated to the anomalously deep Moho in central Finland. The lithospheres beneath the Archean and Proterozoic domains are not noticeably different in the S-wave velocity maps. A classification of the velocity profiles with depth yields four main families and five intermediate regions that can be correlated with surface features. The comparison of these profiles with composition-based shear-wave velocities implies both lateral and vertical

variations of the mineralogy.

5.1 Introduction

The formation and evolution of the earliest continents remain an enigma in Earth sciences. The development of thick lithospheric keels seems to have protected the continental crust from recycling into the mantle. The vertical and lateral extent of these keels and the timing of the stabilization remain unknown. To understand these problems further requires a more complete understanding of the structure of the cratonic lithosphere and the relationship between the crust and upper mantle. Studies of mantle xenoliths can provide insight into the composition and age of the mantle, while seismic studies provide information on the lateral extension of the heterogeneities. For example James *et al.* [2001] show beneath the Kaapvaal and Zimbabwe cratons in South Africa that thick roots are confined to the Archean cratons with no evidence of similar structures beneath the adjacent Proterozoic mobile belts. This is in good agreement with the age distribution of mantle xenoliths proposed by Pearson *et al.* [2002].

The Fennoscandian Shield is the north-western crustal segment of the East-European Craton. It is formed by an Archean nucleus, the Karelian province, flanked to the north-east by the late Archean-Paleoproterozoic Lapland-Kola mobile belt, and to the south-west by the Proterozoic Svecofennian domain [Gorbatschev & Bogdanova, 1993]. The formation of the granite-greenstone Karelian province started some 3.5 Ga ago and continued through the Archean with orogenic maxima around 2.9 and 2.7 Ga [Gorbatschev & Bogdanova, 1993]. The continental crust growth continued with the accretion of several lithospheric blocks over a very long time span through the late Archean and Proterozoic. The formation of the Svecofennian domain was first thought to be very simple and homogeneous, but recently Nironen *et al.* [2002] proposed a succession of five orogenies between 1.92 and 1.79 Ga alternating with continental extensions. The last recorded tectonic events are extensional with the intrusion of the Rapakivi granitoids (1.65 – 1.54 Ga), and the sedimentation of the Subjotnian sandstone formation (1.2 Ga) [Korja *et al.*, 1993]. Since that time the central part of the shield has remained stable.

This composite craton, uncovered by sediments, without noticeable reworking since 1.2 Ga is an ideal place to test the differences between Archean and Proterozoic lithospheres. This area was therefore chosen for one of the investigations of the EUROPROBE program [Gee & Zeyen, 1996], namely the SVEKALAPKO project [Hjelt & Daly, 1996]. Part of the SVEKALAPKO project was a deep teleseismic experiment covering the Finnish part of the Svecofennian domain and southern Karelian province [Bock & SVEKALAPKO Seismic Tomography W. G., 2001]. This array was designed to study the lithosphere-asthenosphere system of the central Baltic Shield and especially the boundary between the Proterozoic Svecofennian domain and the Archean Karelia.

Previous seismic studies of the Baltic Shield have yielded very different estimates of the lithospheric thickness, varying between 160 and 350 km [Sacks *et al.*, 1979; Husebye & Hovland, 1982; Calcagnile, 1982; Babuška *et al.*, 1988; Calcagnile, 1991]. These studies base their conclusions on different concepts – low-velocity zone, wave conversion, lack of lateral heterogeneities – that do not refer to the same physical interpretation of the lithosphere-asthenosphere boundary so they are not necessarily compatible.

The SVEKALAPKO deep seismic tomography experiment is a unique opportunity to obtain the absolute shear-wave velocities in the upper mantle in Fennoscandia through surface-wave analysis. We use a new tomography technique, developed by Bruneton *et al.* [2002]. This method is based on 2-dimensional ray tracing and takes into account the non-planarity of incoming wavefronts. Travel times are inverted to obtain phase velocity maps of the area. One advantage of this surface-wave tomography is that the receivers are located within the tomographic model and not at the model edge as is the case in body-wave tomography,

which allows an efficient modelling of the shape of incoming wavefronts in terms of arrival time on the edge of the study area.

5.2 Data selection and processing

Between August 1998 and May 1999 more than 140 seismic stations operated in the framework of the SVEKALAPKO project [Bock & SVEKALAPKO Seismic Tomography W. G., 2001]. The network was deployed on a 2-dimensional grid covering the central part of the Fennoscandian Shield in southern Finland. Out of these stations, 46 were equipped with broadband sensors (CMG3 and STS2: cut-off frequency 90-100 s, CMG40: cut-off frequency 40-60 s). Very good recording conditions in the shield made it possible to analyse surface waves with periods up to 190 seconds. Figure 5.1 shows the location of the broadband stations as well as the Proterozoic-Archean boundary.

For the present study we use the fundamental mode Rayleigh wave recorded on the vertical component of the sensors. Due to the large number of different sensors and recorders, the data are first corrected from the instrument response. Then we use a phase-matched filter [Herrin & Goforth, 1977; Lander & Levshin, 1989] to extract the fundamental mode Rayleigh wave from the signal.

Out of all the recorded earthquakes of magnitude higher than 5.5 and epicentral distance larger than 30 degrees, we selecte 69 events showing a high quality signal at most of the stations. The geographic distribution of these events is shown in figure 5.2. On the filtered signals we measure time delays between pairs of stations versus frequency using the phase of the Wiener filter [Wiener, 1949; Hwang & Mitchell, 1986; Cotte *et al.*, 1999]. For each station couple we eliminate frequency points with a coherency lower than 0.95 or a signal to noise ratio lower than 4.

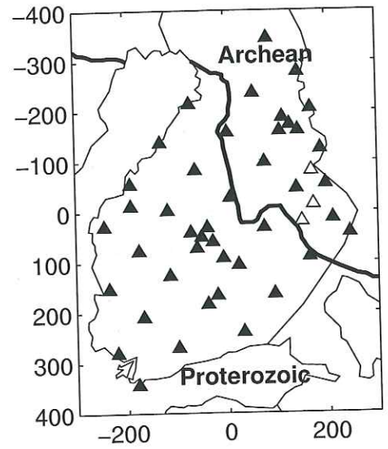

FIG. 5.1 – *Map of the broadband stations of the SVEKALAPKO array (CMG3 and STS2, cut-off frequency 90-100 s: filled triangles, CMG40, cut-off frequency 40-60 s: open triangles). The thick line gives the boundary between the Archean Karelian province in the north-east and the Proterozoic Svecofennian domain in the south-west.*

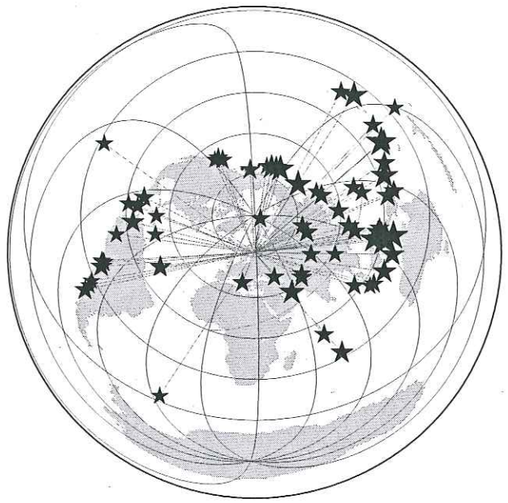

FIG. 5.2 – *Distribution of the 69 events selected for this study, the size of each star is proportional to the magnitude of the event.*

5.3 Methodology

The final aim of this study is to obtain a 3-dimensional model in shear-wave velocity for the region underneath the array, we adopt a two-step method. The first step consists in inverting propagation times of the fundamental mode Rayleigh wave to compute phase velocity maps at each frequency. The combination of the different maps obtained for different frequencies gives a dispersion curve at each location on the map. The second step is an inversion of the dispersion curves to obtain shear-wave velocity versus depth mapping at each grid node and consequently a 3D shear-wave velocity model. This approach therefore assumes that the phase velocity maps yield the structural velocity as defined by Wielandt [1993]. The structural velocity corresponds to the phase velocity in hypothetical flat-layered models with the same elastic parameters as the medium immediately below the considered point. This hypothesis is based on the use of a good azimuthal distribution of the events (figure 5.2).

5.3.1 Travel times inversion

To invert the travel times obtained at a given frequency for a phase velocity map we use the method recently developed by Bruneton *et al.* [2002]. Here we only recall the main characteristics of the method, for a more detailed description we refer to this article.

Bruneton *et al.* [2002] followed the observation that the wavefronts of surface waves at a regional scale are not planar [Tryggvason, 1961; Friederich *et al.*, 1994]. In the inversion scheme the model parameters describe both the phase velocity map and the arrival time of the incoming wavefronts on the border of the studied region.

Forward problem and boundary conditions

The calculation of the travel times is based on the eikonal equation

$$(\nabla T)^2 = c^{-2} = u^2 \tag{5.1}$$

where T is the arrival time of the wave, ∇ the horizontal gradient, c the phase velocity and u the slowness of the medium.

The search for the ray that obeys the boundary conditions is done following a first order perturbation technique known as paraxial ray theory [Farra & Madariaga, 1987; Deschamps, 1972].

The boundary conditions used in the forward problem derive from two hypothesis: (1) the ray should go through the receiver position $\mathbf{x}_r$, and (2) as the wavefronts are known through arrival times $T_0(x_i)$ of the wave along the edge of the studied region, the projection of the slowness vector $\mathbf{p}$ of the ray on the edge x_i should be equal to the derivative of the arrival times $\partial T_0/\partial x_i$.

Once the ray following all boundary conditions is traced, the arrival time of the wave at the receiver is computed by integration along the ray. The derivatives of the arrival time with respect to the model parameters (squared slowness of the medium and wavefront arrival times) are also computed [Bruneton *et al.*, 2002].

Inverse problem

Following Bruneton *et al.* [2002] the inverse problem consists of the linearization of a least-square misfit function S. The minimized quantity is the time residuals between observed $\mathbf{T}^{obs}$ and calculated $\mathbf{T}^{c}$ arrival times. To minimize the non-uniqueness of the solution *a priori* information is introduced in the misfit function:

$$\begin{aligned} S(\mathbf{m}) &= [\mathbf{T}^{obs} - \mathbf{T}^{c}(\mathbf{m})]^T \mathbf{C}_T^{-1} [\mathbf{T}^{obs} - \mathbf{T}^{c}(\mathbf{m})] \\ &\quad + [\mathbf{F}_m - \mathbf{F}(\mathbf{m})]^T \mathbf{C}_F^{-1} [\mathbf{F}_m - \mathbf{F}(\mathbf{m})] \end{aligned} \tag{5.2}$$

where $\mathbf{F}_m$ is the *a priori* value of some parameter combination $\mathbf{F}(\mathbf{m})$.

$\mathbf{C}_T$ and $\mathbf{C}_F$ are the covariance matrices respectively of the travel time data and of the *a priori* conditions. As data are assumed to be uncorrelated the non-diagonal terms of the covariance matrices are set to zero. The diagonal terms of $\mathbf{C}_T$ contain the variance of each data element (see section 5.3.3 for error estimation), and the diagonal terms of $\mathbf{C}_F$ contain the *a priori* uncertainty on the *a priori* values.

We use five types of *a priori* conditions, each of them is represented by an equation and should be followed by the parameters within a given uncertainty depending on the constraint. We first enumerate here the constraints, the following paragraph discusses the relative importance of each uncertainty. (1) The absolute value of the velocity is assumed to be close to an *a priori* value for each period within an uncertainty $\sigma_{F_{u^2}}$ expressed in $s^2.km^{-2}$ as the model parameters representing the velocity are slowness squared. The velocity model is supposed to be relatively smooth, therefore (2) the first and (3) the second derivatives of the slowness squared with regard to the horizontal coordinates are assumed to be zero within respective uncertainties $\sigma_{F_{du^2}}$ and $\sigma_{F_{d^2u^2}}$. (4) The wavefronts are modelled by arrival times on the two edges of the studied region first encountered by the wave, the two edges being treated independently. The times T_0 corresponding to the same point on the two edges are forced to be identical within the uncertainty σ_{F_T}. (5) A smoothness criterion for the wavefronts is added by identifying

the derivative of the arrival time T_0 along the boundary to that of a plane wave arriving from the theoretical back-azimuth ϕ within the uncertainty $\sigma_{F_{dT}}$.

$$\frac{\partial T_0}{\partial x_1} = -\frac{\sin\phi}{c} \quad \text{or} \quad \frac{\partial T_0}{\partial x_2} = \frac{\cos\phi}{c} \tag{5.3}$$

where the axes x_1 and x_2 are oriented respectively toward the east and south. In this study, the angle ϕ is determined by fitting a plane wave to the arrival times of the given wavefront at all stations for each frequency.

The chosen value for each uncertainty gives the strength of the constraint and depends on how tightly we want it to be followed by the model. For example the arrival time at the point shared by two edges has to be single valued, therefore the uncertainty σ_{F_T} has to be very small. On the other side we force the shape of the wavefronts to be smooth, but we want to allow for curved wavefronts, so the fifth constraint should be weak *i.e.* $\sigma_{F_{dT}}$ relatively large. Constraints on the smoothness and absolute value of the velocity field are also rather weak.

As in Bruneton *et al.* [2002] the inversion is solved using a singular value decomposition algorithm.

The model of the inversion contains two types of parameters. The phase-velocity field is modelled by slowness squared, parameterized using third order 2-dimensional B-spline functions [de Boor, 1978] with coefficients distributed on grid nodes every 40 km in x_1 and x_2. Each wavefront is described by its arrival time at the two edges of the studied region first encountered by the wave. Along each one of the two edges the arrival time is modelled using fourth order B-spline interpolation with grid nods every 40 km.

5.3.2 Inversion of the dispersion curves

As output of the previous inversion we obtain phase velocity maps for a series of periods. At every location in the studied region this is equivalent to a phase velocity dispersion curve. We therefore invert independently all the dispersion curves for shear-wave velocity versus depth.

This inversion follows a linearized method that allows the consideration of both independent layers and continuous media between the interfaces [Maupin & Cara, 1992]. For the direct modelling and computation of the partial derivatives we use the program package developed by Saito [1988]. The inversion algorithm is that of Tarantola & Valette [1982], minimizing the square of the phase velocity discrepancy. The P-wave velocities and densities are kept fixed during the inversion.

In the algorithm of Tarantola & Valette [1982] the model covariance matrix makes it possible to quantify the smoothness of the shear-wave velocity with depth. The shape of the correlation functions is chosen to be Gaussian as in Lévêque *et al.* [1991]. The correlation length is defined as the half width of the Gaussian for the 60% confidence interval.

In the inversion of dispersion curves a trade-off exists between adjacent layers, in particular between the crustal structure and the shallow mantle. In the region of the SVEKALAPKO array, the crustal structure is particularly well known, due to numerous deep seismic sounding profiles. A compilation of all refraction and reflection data for the region was recently performed by Sandoval *et al.* [2003] to compute a 3D crustal model in P-wave velocity. To constrain our dispersion curve inversions we set the depth of the Moho discontinuity at every location following the Sandoval *et al.* [2003] Moho depth model. We also test the influence of the Moho depth on the obtained model.

The result of our second inversion step is an absolute shear-wave velocity model constructed from surface waves of wavelengths between 40 and 900 km. Because of anelasticity in the Earth such a model cannot be directly compared with velocities obtained from other techniques, short-period body wave tomography in particular. The velocity model we present here is corrected for anelasticity using a simple $Q(z)$ model derived from PREM [Dziewonski & Anderson, 1981] (adapted for each Moho depth) and a reference frequency of 1 Hz, so as to facilitate the discussion of our results. The correction is made according to equation

(5.81) of [Aki & Richards, 2002]:

$$V(z)_{\omega_1} = V(z)_{\omega_2}\left[1 + \frac{1}{\pi Q(z)} ln\left(\frac{\omega_1}{\omega_2(z)}\right)\right] \tag{5.4}$$

where $\omega_1 = 1$ Hz and $\omega_2(z)$ is a period representative of the periods of the surface waves that sample the medium at depth z.

5.3.3 Resolution assessments

The interpretation of any tomographic result requires careful estimation of the error bars associated with the obtained images. In the present study the combination of different methods renders this analysis more complicated. We analyse first the uncertainty in the wave arrival times, then the phase velocity maps, and finally the shear-wave velocity model.

Arrival time uncertainty

The estimation of the data time uncertainty derives from the estimation of the arrival time value itself. As explained in section 5.2 we measure delay times between pairs of stations. The input of the inversion has to be the arrival time of the wave at a given station. The simplest way to convert our delay times in arrival times is to set the origin time to be the arrival time at one station chosen as the reference and to use arrival times relative to this particular station.

For each event, the reference station is chosen as one with a very high quality signal out of the first stations encountered by the wave. As a stabilisation procedure we consider as arrival time for a given station the mean of all available time-delay measurements with the reference station using an intermediate third station.

As uncertainty in the measurement we use twice the standard deviation of these time delays. This rather pessimistic value is used because the different measurements are not independent, so we consider the standard deviation to be too optimistic as an error estimate. For a better consistency of the data set

we use a minimum value of 1 s for the uncertainty. We assume the data to be uncorrelated and consequently the data covariance matrix is a diagonal matrix containing the squared uncertainties.

Variance of the phase velocity model

In the inversion for phase velocity maps the *a posteriori* covariance matrix of the model is computed following Tarantola [1987] [see also equation 17 of Bruneton *et al.*, 2002]. This error estimate varies as a function of several factors: the experiment's geometry and the volume of data, the covariance matrix of the travel time data (see previous section) and the *a priori* uncertainty chosen for the *a priori* constraints.

The strength of the *a priori* constraints is chosen from physical considerations. Bruneton *et al.* [2002] showed from synthetic tests that the smallest structure that could be correctly imaged by the SVEKALAPKO array is 150 km large. The use of the coherent part of the signal and of the ray theory also restrains us to structures of size not smaller than the wavelength for each period. From these considerations the appropriate uncertainties in the constraints are taken as:

$$\sigma_{F_{u^2}} = 5\ 10^{-3}\ \mathrm{s}^2.\mathrm{km}^{-2} \tag{5.5}$$

$$10^{-5} \leq \sigma_{F_{du^2}} \leq 5\ 10^{-4}\ \mathrm{s}^2.\mathrm{km}^{-3} \tag{5.6}$$

$$10^{-7} \leq \sigma_{F_{d^2u^2}} \leq 2\ 10^{-6}\ \mathrm{s}^2.\mathrm{km}^{-4} \tag{5.7}$$

$$\sigma_{F_T} = 0.1\ \mathrm{s} \tag{5.8}$$

$$\sigma_{F_{dT}} = 5\ 10^{-2}\ \mathrm{s.km}^{-1} \tag{5.9}$$

where the values of $\sigma_{F_{du^2}}$ and $\sigma_{F_{d^2u^2}}$ decrease with increasing wavelength.

The inversion gives us the *a posteriori* variance of the slowness squared. It can be converted into the variance of the phase velocity by derivation of $u^2 = c^{-2}$:

$$\sigma_c = c^3 \sigma_{u^2}/2 \tag{5.10}$$

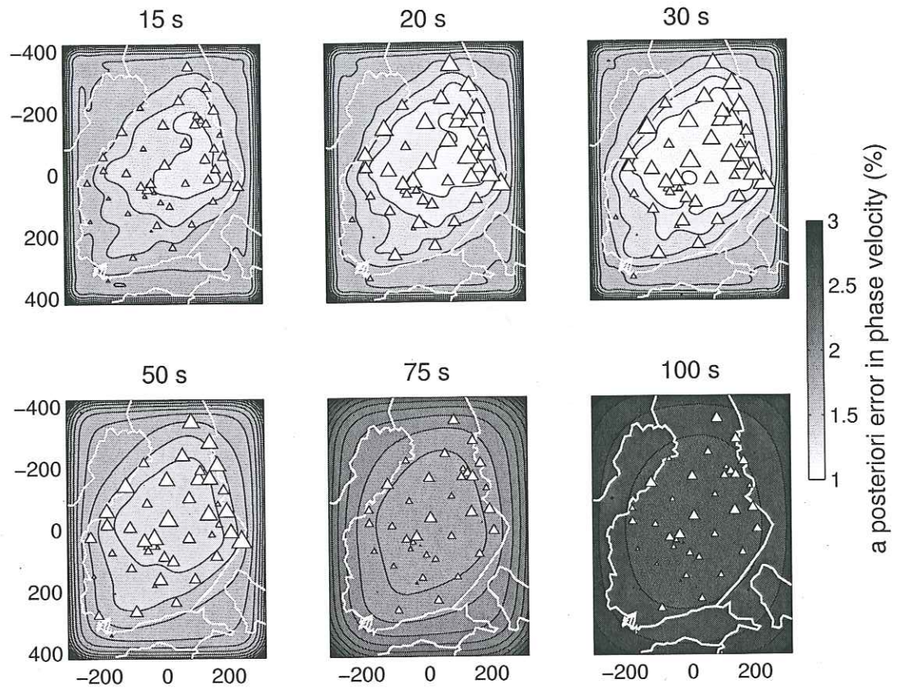

FIG. 5.3 – *A posteriori error in the phase velocity for different periods. White triangles represent the station position, their size is proportional to the volume of data recorded for the given station and period.*

To be able to compare the phase velocity uncertainties for different frequencies we use a constant reference phase velocity $c = 4\ \mathrm{km.s}^{-1}$ in equation (5.10).

The increase with period of the constraints on the lateral variations corresponds to a smaller number of independent parameters. The velocity values are therefore well resolved at long periods which corresponds to small *a posteriori* errors. However, these small errors at long periods do not reflect reality: even though the velocities are well resolved in a mathematical sense, there may still be significant lateral variations of structural velocities at long periods. To obtain more realistic error measurements we add a constant uncertainty to the velocity

errors so that the maximum uncertainty is the same for all periods. The reference period for this normalization is taken as 20 s. Figure 5.3 shows the *a posteriori* error in the phase velocity obtained for periods between 15 and 100 seconds.

Shear-wave velocity uncertainty

The dispersion curve inversion algorithm we use allows us to compute both the model *a posteriori* error bars and the resolution. These values depend on the input uncertainties in the phase velocities explained above and on the *a priori* covariance of the model.

The later derive from an *a priori* error in shear-wave velocity with respect to a reference model and a correlation length parameter. The *a priori* error in S-wave velocity defines to what extent the final model can vary from the initial one. We choose a value of 4%. Considering that the initial model is an average model for the region, this value is relatively large. The correlation length defines the smoothness of the shear-wave velocity model with depth. We choose a value of 20 km. An inversion with a smaller correlation length gives similar results (maximum discrepancy 0.2%) and confirms that our data do not contain information concerning the fine structure of the mantle.

Figure 5.4 presents the obtained *a posteriori* error in shear-wave velocity versus depth for three different locations. The error is larger for the points close to the interfaces: because of the use of a Gaussian correlation function, these points are correlated to a smaller number of points. With depth the error increases due to the larger error in the phase velocities for larger periods. For the lower-most crustal layer and the shallower mantle the high uncertainty values reflect the trade-off between lower crust and shallower mantle, however as the Moho depth is well constrained our obtained velocities are reliable.

An estimation of the resolution of the lateral variations with depth can be computed from the penetration depth of the seismic wave used. We measure

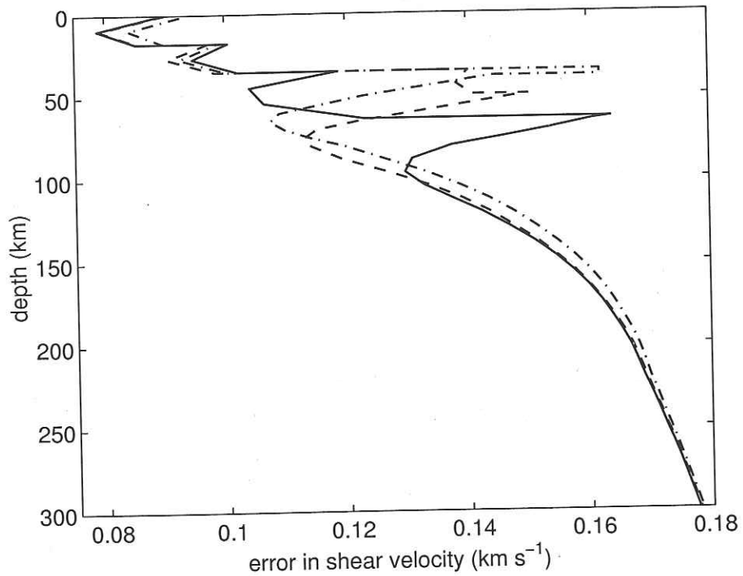

FIG. 5.4 – *A posteriori error in shear-wave velocity for three different Moho depths: solid line 63.5 km, dashed line 49.5 km dash-dotted line 38.5 km.*

arrival times for periods between 10.5 and 190 s, which means that the wavelength varies between 35 and 900 km approximately. If the wavelength is larger than the aperture of the array the lateral variations are not resolved. The deepest lateral variations that we can image are those recorded by the 100 s period Rayleigh wave of roughly 430 km wavelength. We therefore do not have any resolution in the lateral variations deeper than 150 km.

5.4 Phase velocity maps

Figure 5.5 presents the phase velocity maps obtained for periods between 15 and 100 seconds. The most prominent feature is a slow structure in the center of the array for the higher frequencies. Its position and shape correspond roughly with the deep Moho structure imaged by Sandoval *et al.* [2003].

The final model is obtained after two iterations for every period. The reduction of the misfit function is always important and is mainly due to the curvature of the wave-fronts. For the higher and lower frequencies the final misfit function is larger than 1, indicating that the theory used does not completely explain the data within the error bars. This may be due to a high noise level at some stations or to phenomena we do not take into account in our modellization, for example anisotropy.

The azimuth distribution of our data is far from perfect, a majority of events coming from the north-eastern quarter. To test the influence of the azimuth distribution we remove some events of our data set to obtain a maximum of 2 events per 15 degrees sector in the north-eastern quarter and 3 elsewhere. The events selected are those with the best fit to a plane wave as this ensure that only highest-quality events are selected: a bad fit to the plane wave could correspond to questionable measurements or to an anomalous wavefront that we cannot model using ray theory.

Figure 5.6 shows an example for the period of 40 seconds, the azimuth dis-

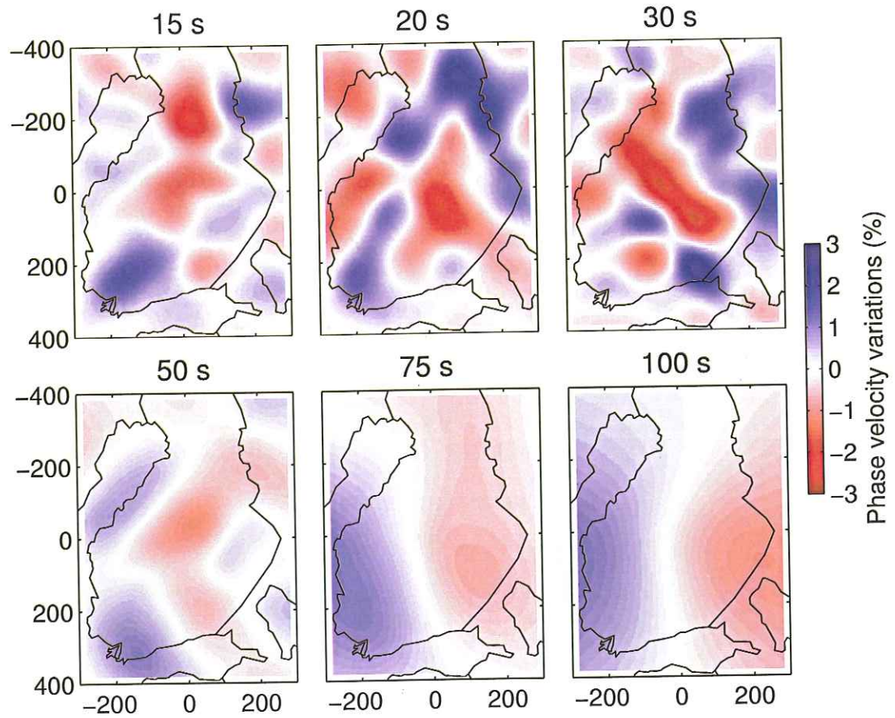

FIG. 5.5 – *Lateral variations of the phase velocity for selected periods (title of each panel) of the fundamental mode Rayleigh wave. Triangles mark the stations location.*

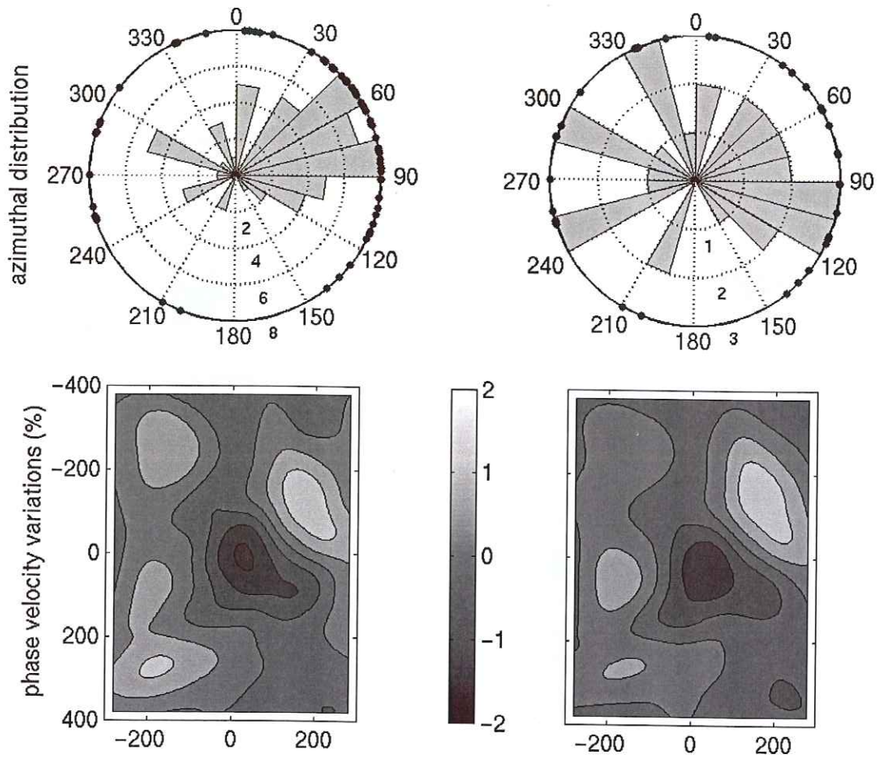

FIG. 5.6 – *Influence of the azimuth distribution on the phase velocity map, example for 40 seconds period; left panels: complete data set, right panels: selected data set.*

tribution of the complete and selected data sets are plotted in the upper panels, the associated phase velocity map in the bottom panels. The two phase velocity maps are similar. The position and shape of the heterogeneities are not modified with a better azimuth distribution except for an effect of smoothing, their amplitude is also slightly reduced. Both reduction and smoothing are explained by the fact that the values of the constraints are identical for the two inversions. As the volume of data is reduced in the second data set the relative importance of the smoothing constraints is larger.

The same conclusion is drawn for all the periods used in this study. As was already noticed by Bruneton *et al.* [2002] the azimuth distribution does not have an important effect on the inversion result.

5.5 3D shear-wave velocity model

All the phase-velocity maps together give a dispersion curve for each grid node. These dispersion curves are inverted to obtain the 3D shear-wave velocity model. The Moho depth is fixed at every location following the well constrained 3D crustal model by Sandoval *et al.* [2003]. The initial shear-wave velocities derive from a regional-average model computed from the same data set (see section 4). P-wave velocities, densities and the depths of interfaces between layers are kept fixed during the inversion. We first discuss the final 3D shear-wave velocity model, followed by tests to estimate the influence of the initial model and of the Moho depth.

Shear-wave velocity versus depth profiles (figure 5.7) show that the region is characterized by, on average, a lithospheric mantle 4% faster than standard Earth models. The reference velocity does not exhibit a low velocity zone (LVZ), while most of the individual profiles have a LVZ between 140 and 240 km. The lateral heterogeneity persists across the resolved part of the mantle, we therefore interpret these variations as lateral variations in the composition of the lithosphere

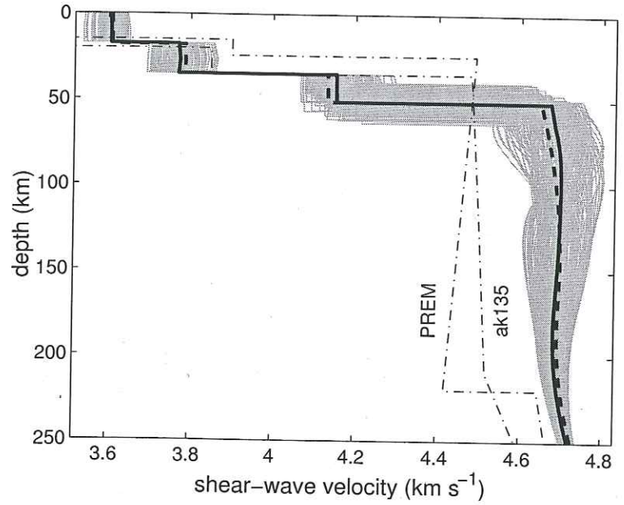

FIG. 5.7 – *Shear-wave velocity model with depth, each individual profile for a grid node is a grey line; solid black line: average model used as reference in figures 5.8 and 5.9; dashed black line: initial model; thin dash-dotted lines: standard Earth models PREM [Dziewonski & Anderson, 1981] and ak135 [Kennett et al., 1995].*

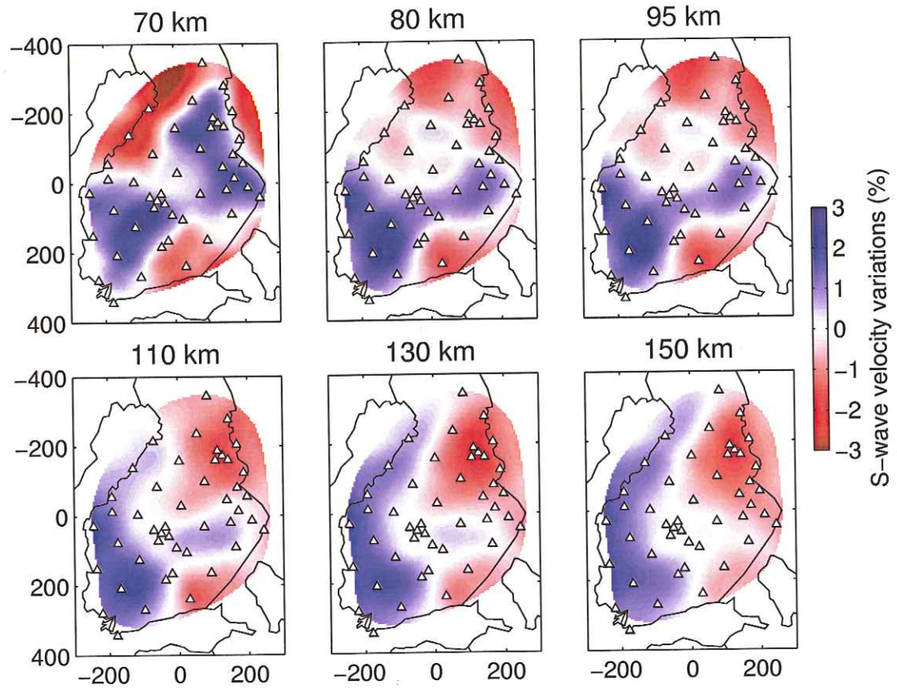

FIG. 5.8 – *Horizontal sections at different depths in our 3D shear-wave velocity model, lateral velocity variations are given in percentage with respect to the average of the layer; triangle mark the station positions.*

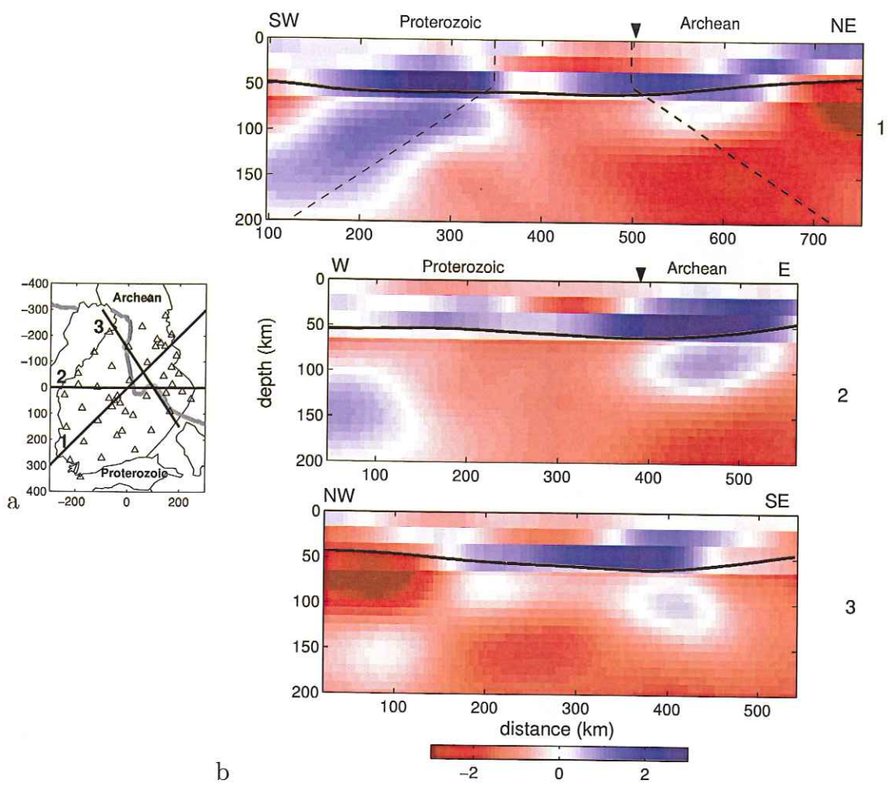

FIG. 5.9 – *Vertical cross-sections across the 3D shear-wave velocity model; a) map showing the location of the cross-sections (thick black lines) numbered from 1 to 3, and the tectonic limit between Archean in the north-east and Proterozoic in the south-west (thick grey line); b) cross-sections 1 to 3. Velocity variations are in percentage with respect to the average value for each depth, in sections 1 and 2 a black triangle indicates the approximate location of the tectonic Archean-Proterozoic boundary (section three approximately follows this boundary), the black line in the cross-sections represents the Moho depth; the dashed lines of section 1 show the lateral resolution considered.*

and not as variations of the depth of the lithosphere-asthenosphere boundary.

The depth slices (figure 5.8) show that the Moho trough in the center of the array is generally associated with high velocities in the lower crust and shallower mantle to 100 km depth. At further depths, a small spot of higher velocities persists down to almost 150 km in the center of the array, while velocities are generally high in the south-west and low in the north-east and south-east. The Archean-Proterozoic boundary is not associated with a clear pattern in the upper 150 km of the mantle. Below 100 km the Archean domain seems to be mainly associated with relative low velocities whereas the Proterozoic domain mainly has high velocities, however this is not consistant with the classical sketch of a highly depleted Archean mantle and a less depleted Proterozoic mantle, as depletion produces higher velocities [Jordan, 1979].

Figure 5.9 displays the obtained shear-wave velocity along three cross-sections of the study area. Cross-section 1 is perpendicular to the Archean-Proterozoic boundary. Cross-section 2 coincides with that of Sandoval [2002]; Sandoval *et al.* [submitted]. Cross-section 3 is slightly displaced as compared to Sandoval [2002]; Sandoval *et al.* [submitted], to better assess whether features at depth can be followed along the Archean-Proterozoic boundary. It is rather difficult to compare the two sets of results, as the variation is calculated to obtain a zero average over the study area. The study area of Sandoval *et al.* [submitted] is significantly larger than ours due to their use of a body-wave tomography approach. Additionally, their background model is poorly constrained.

We obtain amplitudes variations of $\pm$ 3%, which is compatible with P-wave velocity variations of $\pm$ 2% obtained by Sandoval *et al.* [submitted] as shear-wave velocities are generally more sensitive to temperature and compositional variations. Similarly to the P-wave tomography model we do not see any clear relation between the velocity pattern in the mantle and surface geology, in particular the Archean and Proterozoic domains do not exhibit significantly different velocities. Both velocity models have a relative high velocity structure in the center of the

study area, but ours disappears around 100 km whereas that of Sandoval *et al.* [submitted] gets weaker at 150 km but continues down to 300 km.

Some features are clearly different between the two models. The south-western corner of our study region is characterized by relatively high velocities, while Sandoval *et al.* [submitted] obtain relatively low velocities. The north eastern part of the model is part of high velocity body of the P-wave tomography model whereas it becomes a low velocity region below 100 km in ours. These discrepancies can be attributed to the differences of method and data sets. Our lateral resolution is poor especially at larger depth (see figure 5.9) while P-wave tomography may have some vertical leakage. We estimate our lateral resolution as equal to one wavelength, for a depth corresponding to a third of the wavelength with an additional restriction to minimum 150 km due to the spacing between stations (see section 5.3.3). This estimate is of the same order as the influence zone used by Kennett & Yoshizawa [2002], or the resolution computed by Friederich [2003] in regional surface wave tomographies. An alternative interpretation is that P- and S- wave velocities have different behaviours in relation to compositional variations.

5.5.1 Influence of the initial model

The initial model used for the 3D inversion is obtained by inversion of an average dispersion curve for the whole modelled area. The average dispersion curve derives from the procedure described in section 5.3.1, using a unique cell covering the stations array and strong smoothing constraints for the velocity, but enabling curved wavefronts. The inversion for shear-wave velocity of this average dispersion curve is done using a large correlation length so as to obtain a reasonable model from an arbitrary initial model [model ak135, Kennett *et al.*, 1995, which we have smoothed and in which we includ a realistic crustal thickness of 51 km].

To test the influence of the initial model on the recovered 3D shear-wave

velocity, we use another initial model. This model derives from the computations by Kukkonen *et al.* [2003] based on xenolith compositions and the associated geotherm. The two initial models are similar except for the lower crustal layer where the velocity of the xenolith-derived model is lower by 1.5% and for the mantle above 90 km depth where the velocity is 1% higher. The change in the initial shear-wave velocity does not influence the recovered lateral variations while the absolute values of the shear-wave velocities are shifted by approximately the same amount as the initial model.

5.5.2 Influence of the Moho depth

The procedure of inversion of the dispersion curve does not invert for the depths of interfaces in the crust and mantle. The fixed Moho depth is a very strong constraint on the shear-wave velocity model. We therefore have to test the effects of a reasonable modification of the Moho depth model.

The 3D crustal model used [Sandoval *et al.*, 2003] has been tested by forward modelling of multiple P and S wave arrivals of local events. A joint inversion of seismic and gravity data recently confirmed this crustal structure and supplemented it with density values [Kozlovskaya *et al.*, submitted]. The shape and depth of the Moho in the region of the SVEKALAPKO array are estimated to be precise within 2 km (Kozlovskaya, personal communication).

For a point in the center of the array we conduct several inversions by varying the Moho depth by 3 km. The Moho depth affects the velocity of the lower crustal layer and of the mantle down to approximately 120 km: the deeper the Moho, the higher the velocities. Variations are of the order of 0.75% for the crustal layer and less than 0.5% for the mantle.

The modifications of the velocity model produced by a reasonable modification of the Moho depth are half an order of magnitude lower than the lateral variations. Further improvements of the Moho map are unlikely to significantly modify our

3D model.

5.6 Discussion

Our 3D shear-wave velocity model is characterized by relatively high velocities in the lower crust and shallower mantle down to at least 100 km in the area where the Moho is anomalously deep. No clear pattern seems to be related to the surface geology, and in particular the Archean and Proterozoic domains do not have significantly different velocities in the lithospheric mantle.

For a further interpretation we made a classification of the shear-wave velocity profiles with depth. Figure 5.10 presents the 9 families we define. Plots 5.10a,c,g,i are the principal families, the five others have intermediate shapes. The transitional families could be due to the horizontal smoothing we apply during the inversion or to real different material. If we compare our map 5.10j to the map of Plomerova *et al.* [2003] showing the pattern of anisotropy direction observed from P-wave residuals, we can associate their Proterozoic family to our categories 5.10a,g,h,i, their Archean family to our 5.10c family and their transitional region to our intermidiate families 5.10d,e,f. The two independent data sets agree on the existence of a region in the centre of the SVEKALAPKO array caracterized by a signature that seems to be intermediate between the Archean and the Proterozoic domains.

Interpretation of seismic velocity heterogeneities are generally based on thermal variations [see for example Goes *et al.*, 2000; Röhm *et al.*, 2000]. However, Fennoscandia has probably not been submitted to major thermal events for approximately the last 1.5 Ga. Present measurements of the surface heat flow [Kukkonen, 1993] supports the idea of uniform upper mantle temperatures beneath Finland. The study of receiver functions also depicts horizontal interfaces at the seismic boundaries of 410 and 660 km [Alinaghi *et al.*, 2003], which also implies a homogeneous upper-mantle temperature. These interfaces are slightly shallower

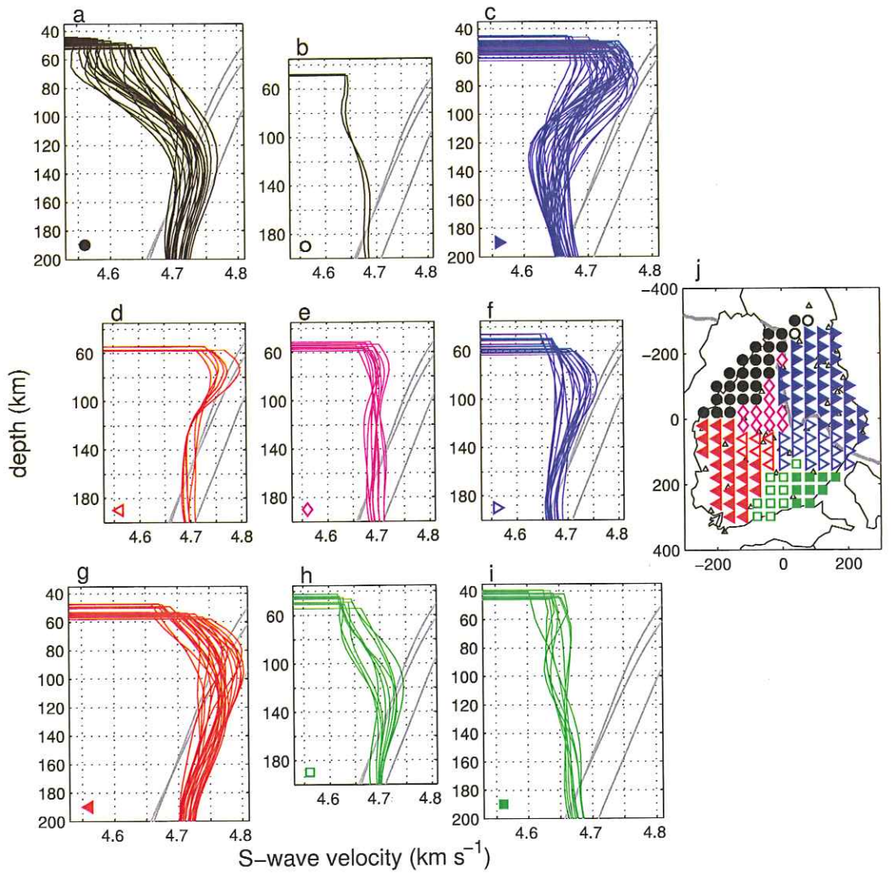

FIG. 5.10 – *Classification of the shear-wave velocity with depth profiles. a-i) black lines: S-wave velocity profiles, grey lines: composition-based velocities, the marker in the lower-left corner refer to the marker on the map; j) map showing the location of the different families.*

than the global average depth on the Earth indicating a cold upper mantle. The cause of the observed seismic velocity variations must therefore be of compositional origin. We compare the velocity profiles to models computed from the mineral composition of "normal" rocks for a precambrian lithosphere. We propose here a possible explanation for our four main families (5.10a,c,g,i). The rock composition used are lherzolite and harzburgite xenoliths sampled in the Eastern Finland kimberlite cluster [from lower to higher velocities, samples L66, L29 and L48 of Kukkonen & Peltonen, 1999].

The seismic velocities depend on the density and elastic parameters, which in turn depend on the rock composition, the orientation of minerals and temperature and pressure conditions. Reference values for the elastic parameters of the major minerals as well as their pressure and temperature derivatives are known from laboratory experiment [see Table A1 of Goes *et al.*, 2000]). The geotherm used is that of Kukkonen *et al.* [2003], it is calculated from a two-dimensional conductive model along a seismic profile in the kimberlite province [Kukkonen & Jõeleht, 1996; Kukkonen & Peltonen, 1999]. The boundary condition used in the mantle for this geotherm is a constant heat flow density of 12 mW m^{-2} at 250 km depth. It is in satisfactory agreement with the thermobarometry of the xenolith samples (less than 100°C discrepancy except for three samples). The overall velocity of the rock is calculated using the Voigt-Reuss-Hill average, which gives the same average values as the more accurate Hashin-Shtrikman averaging but is easier to compute [Vacher *et al.*, 1996]. Following Goes *et al.* [2000] we also take into account anharmonicity and anelasticity.

Family 5.10g in the south-western part of the array resides inside the Svecofennian domain. These profiles have velocities compatible with a "normal" composition from 100 km depth down to the loss of resolution of our model. For the shallower mantle the velocities are lower in the surface wave derived profiles, however it is the part of our model where the uncertainties are higher and these variations may not be significant.

In the north-western region, family 5.10a presents "normal" velocities for the lower part of the model below 140 km, and significantly lower velocities for the upper part of the lithospheric mantle. New interpretation of the geology of the Baltic shield yields a complex history for the formation of the Svecofennian domain Nironen *et al.* [2002]. These author present a map of the curent position of lithospheric blocks that accreted around 2 Ga. The location of our 5.10a family corresponds to the Knaften arc. The subduction that produced the volcanic arc also introduced a certain amount of water in the upper part of the mantle therefore modifying the composition of the peridotites. The hydrated minerals generally produce slower seismic velocities. Such a tectonic history could also add some eclogitic material to the mantle, eclogite are another composition that produce slower velocities.

Family 5.10i has an anomalous velocity profile: almost constant for all depths. The south-eastern corner of the SVEKALAPKO array where this family is located correlates with the Rapakivi granitoids. As these rocks are associated with mafic dykes derived from upper mantle partial melts [Korja *et al.*, 1993] they are thought to be of deep origin. Our model suggest that they are associated with an anomaly extending at least to 200 km.

The Archean domain (5.10c) is the most difficult to interpret. The velocity seems compatible with "normal" peridotites immediately below the Moho to 90 km depth, a low velocity zone is situated at 140 km depth, followed by velocities again increasing. A metasomatisme of deep origin could have lowered the velocities from the bottom of the lithosphere without reaching the surface. The relatively higher velocities deeper than 140 km could be an artifact of our horizontal smoothing.

The hypothesis of a high degree of heterogeneity in the lithosphere of the Svecofennian domain also correlates well with the observations of a complex pattern of crustal conductivity in Fennoscandia [Korja *et al.*, 2002]. The history of the Baltic Shield appears to be more complex than that of the Kaapvaal Craton

in South Africa [Fouch *et al.*, submitted; James *et al.*, 2001] or the Australian continent [Simons *et al.*, 2002] where the seismic tomography closely relates to surface features.

A comparison with an absolute P-wave velocity model could be of a great help to understand these variations.

5.7 Conclusions

We conducted an inversion of fundamental mode Rayleigh wave travel time data to obtain a regional 3D shear-wave velocity model under a dense array of stations in the Central Baltic Shield. The method used is based on two-dimensional ray tracing which is innovative in that the curvature of the wavefronts is taken into account.

Our final shear-wave velocity model shows lateral variations at each depth of $\pm$ 3% around the average value. The obtained velocities are on average 4% higher than standard Earth models for the upper mantle down to 200 km. There is no evidence for a substantial low velocity zone. Our model does not allow any conclusions to be drawn on the thickness of the lithosphere as lateral heterogeneities are only resolved down to 150 km. The interpretation of the shear-wave velocity profiles with depth yields the definition of nine different regions. The main four regions can be correlated to geological features and can be interpreted by different vertical layering of mantellic rocks.

acknowledgments

We thank Tellervo Hyvönen for her help during the field work, as well as the numerous people who took part in it. The French participation received financial support from the Intérieur de la Terre program of INSU and used Lithoscope and RLBM seismic stations. We thank Valérie Maupin and Jean-Jacques Lévêque for

the dispersion-curve inversion code, Senen Sandoval for the Moho depth model, Ilmo Kukkonen for the xenoliths-based seismic velocity model. This paper highly benefited from discussions with Nick T. Arndt and Michel Bouchon. The European Science Foundation financed most of the workshops of the SVEKALAPKO project. Most of the computations presented in this paper were performed at the Service Commun de Calcul Intensif de l'Observatoire de Grenoble (SCCI). We used SAC for the treatment of the seismograms; figure 5.1 was drawn using GMT.

Bibliographie

Aki, K. & P. G. Richards, 2002. *Quantitative seismology*, second edition, University Science Books, Sausalito, California.

Alinaghi, A., G. Bock, R. Kind, W. Hanka, K. Wylegalla, TOR and SVEKALAPKO Groups, 2003. Receiver function analysis of the crust and upper mantle from the North German Basin to the Archean Baltic Shield. *Geophys. J. Int.*, 155, 641–652.

Babuška, V., J. Plomerová & P. Pajdušák, 1988. Seismologically determined deep lithosphere structure in Fennoscandia, Proceedings in *Geologiska Föreningens i Stokholm Förhandlingar*, **110**, 380–382.

Bock, G. & the SVEKALAPKO Seismic Tomography Working Group, 2001. Seismic Probing of the Fennoscandian lithosphere, *EOS, Trans. Am. Geophys. Un.*, **82**, 621, 628–629.

Bruneton, M., V. Farra, H. A. Pedersen & the SVEKALAPKO Seismic Tomography Working Group, 2002. Non-linear surface wave phase velocity inversion based on ray theory, *Geophys. J. Int.*, **151**, 583–596.

Calcagnile, G., 1982. The lithosphere-asthenosphere system in Fennoscandia, *Tectonophysics*, **90**, 19–35.

Calcagnile, G., 1991. Deep structure of Fennoscandia from fundamental and higher mode dispersion of Rayleigh waves, *Tectonophysics*, **195**, 139–149.

Cotte, N., H. A. Pedersen, M. Campillo, J. Ni, R. Kind, E. Sandvol & W. Zhao, 1999. Determination of the crustal structure in South Tibet by dispersion and amplitude analysis of surface waves, *Geophys. J. Int.*, **138**, 809–819.

De Boor, C., 1978. *A practical guide to splines*, Spring-Verlag, New-York.

Deschamps, G. A., 1972. Ray techniques in electromagnetics, *Proc. IEEE*, **60**, 1022–1035.

Dziewonski, A. M. & D. L. Anderson, 1981. Preliminary Reference Earth Model, *Phys. Earth Planet. Int.*, **25**, 297–356.

Farra, V. & R. Madariaga, 1987. Seismic waveform modeling in heterogeneous media by ray perturbation theory, *J. Geophys. Res.*, **92**, 2697–2712.

Fouch, M. J., D. E. James, J. C. Vandecar, S. van der Lee & the Kaapvaal Seismic Group, submitted. Mantle seismic structure beneath the Kaapvaal and Zimbabwe cratons, *S. Africa J. Geol.*.

Friederich, W., 2003. The S-velocity structure of the East Asian mantle from inversion of shear and surface waveforms, *Geophys. J. Int.*, **153**, 88-102.

Friederich, W., E. Wielandt & S. Stange, 1994. Non-plane geometries of seismic surface wavefields and their implications for regional surface-wave tomography, *Geophys. J. Int.*, **119**, 931–948.

Gee, D. G. & H. J. Zeyen (eds.), 1996. *EUROPROBE 1996 – lithosphere dynamics: origin and evolution of continents*, EUROPROBE secretariat, Uppsala University, Uppsala, Sweden.

Goes, S., R. Gover & P. Vacher, 2000. Shallow mantle temperatures under Europe from P and S wave tomography, *J. Geophys, Res.*,**105**, 11153–11169.

Gorbatschev, R. & S. Bogdanova, 1993. Frontiers in the Baltic Shield. *Precambrian Res.*, **64**, 3-21.

Herrin, E. & T. Goforth, 1977. Phase-matched filters: application to the study of Rayleigh waves, *Bull. Seism. Soc. Am.*, **67**, 1259–1275.

Hjelt, S.-E. & J. S. Daly, 1996. SVEKALAPKO, evolution of Paleoproterozoic and Archean lithosphere, in *EUROPROBE 1996 – lithosphere dynamics: origin and evolution of continents*, D. G. Gee and H. J. Zeyen (eds.), EUROPROBE secretariat, Uppsala University, Uppsala, Sweden.

Husebye, E. S. & J. Hovland, 1982. On upper mantle seismic heterogeneities beneath Fennoscandia, *Tectonophysics*, **90**, 1–17.

Hwang, H. J. & B. J. Mitchell, 1986. Interstation surface wave analysis by frequency-domain Wiener deconvolution and modal isolation, *Bull. Seism. Soc. Am.*, **76**, 847-864.

James, D. E., M. J. Fouch, J. C. VanDecar, S. van der Lee & the Kaapvaal Seismic Group, 2001. Tectospheric structure beneath southern Africa, *Geophys. Res. Lett.*, **28**, 2485–2488.

Jordan, T. H., 1979. The deep structure of the continents, *Scientific American*, **240**, 92–107.

Kennett, B. L. N. & K. Yoshizawa, 2002. A reappraisal of regional surface wave tomography, *Geophys. J. Int.*, **150**, 37–44.

Kennett, B. L. N., E. R. Engdhal & R. Buland, 1995. Constraints on seismic velocities in the Earth from traveltimes, *Geophys. J. Int.*, **122**, 108–124.

Korja, A., T. Korja, U. Luosto & P. Heikkinen, 1993. Seismic and geoelectric evidence for collisional and extensional events in the Fennoscandian Shield – implication for Precambrian crustal evolution, *Tectonophysics*, **219**, 129–152.

Korja, T., M. Engels, A. A. Zhamaletdinov, A. A. Kovtun, N. A., Palshin, M. Yu. Smirnov, A. D. Tokarev, V. E. Asming, L. L. Vanyan, I. L. Vardaniants & the BEAR Working Group, 2002. Crustal conductivity in Fennoscandia – a compilation of a database on crustal conductance in the Fennoscandian Shield, *Earth Planets Space*, **54**, 535–558.

Kozlovskaya, E., S. Elo, S.-E. Hjelt, J. Yliniemi, M. Pirttijärvi & the SVEKALAPKO Seismic Tomography Working Group, submitted. 3D density model of the crust of southern and central Finland obtained from joint interpretation of SVEKALAPKO crustal P-wave velocity model and gravity data, *Geophys. J. Int.*.

Kukkonen, I. T., 1993. Heat-flow map of northern and central parts of the Fennoscandian Shield based on geochemical surveys of heat producing elements, *Tectonophysics*, **225**, 3–13.

Kukkonen, I. T., and A. Jõeleht, 1996. Geothermal modelling of the lithosphere in the central Baltic shield and its southern slope, *Tectonophysics*, **255**, 24–45.

Kukkonen, I. T., and P. Peltonen, 1999. Xenolith-controlled geotherm for the central Fennoscandian Shield: implications for lithospheric-asthenospheric relations, *Tectonophysics*, **304**, 301–315.

Kukkonen, I. T., K. Kinnunen & P. Peltonen, 2003. Mantle xenoliths and thick lithosphere in the Fennoscandian Shield, *Physics and Chemistry of the Earth*, **28**, 349–360.

Lander, A. V. & A. L. Levshin, 1989. Recording, identification, and measurement of surface wave parameters, in *Seismic surface waves in laterally inhomogeneous Earth*, V. I. Keilis-Borok (ed.), Kluwer Academic Publishers, Dordrecht, 131–182.

Lévêque, J.-J., M. Cara & D. Rouland, 1991. Waveform inversion of surface wave data: test of a new tool for systematic investigation of upper mantle structures, *Geophys. J. Int.*, **104**, 565–581.

Maupin, V. & M. Cara, 1992. Love-Rayleigh wave incompatibility and possible deep upper mantle anisotropy in the Iberian peninsula, *Pure appl. Geophys.*, **138**, 429–444.

Nironen, M., R. Lahtinen & A. Korja, 2002. Paleoproterozoic tectonic evolution of the Fennoscandian shield – comparison to modern analogues, in *Lithosphere 2002 – second symposium on the structure, composition and evolution of the lithosphere in Finland. Programme and extended abstracts, Espoo, Finland*, R. Lahtinen, A. Korja, K. Arhe, O. Eklund, S.-E. Hjelt & L. J. Pesonen (eds.), Institute of Seismology,

University of Helsinki, report S-42, 95–97.

Pearson, D. G., G. J. Irvine, R. W. Carlson, M. G. Kopylova & D. A. Ionov, 2002. The development of lithospheric keels beneath the earliest continents: time constraints using PGE and Re-Os isotope systematics, in *The early Earth: physical, chemical and biological development*, C. M. R. Fowler, C. J. Ebinger & C. J. Hawkesworth (eds.), Geologycal Society, London, Special Publication, **199**, 65–90.

Plomerová, J., T. Hyvönen, V. Babuška, L. Vecsey, T. Raita , the SVEKALAPKO Seismic Tomography Working Group & the TOR Working Group, 2003. Seismic-wave anisotropy of the subcrustal lithosphere of Fennoscandia based on body-wave data recorded during the international passive experiments, *EGS-AGU-EUG Joint Meeting*, Session TS2.02 The deep structure of continents, G. Bock & S. Daly, abstract EAE03-A-03891, Nice, 2003.

Röhm, A. H., R. K. Snieder, S. Goes & J. Trampert, 2000. Thermal structure of the continental upper mantle inferred from S wave velocity and surface heat flow, *Earth Planet. Sci. Lett.*, **181**, 395–408.

Sacks, I. S., J. A. Snoke & E. S. Husebye, 1979. Lithosphere thickness beneath the Baltic Shield, *Tectonophysics*, **56**, 101–110.

Saito, M., 1988. Disper 80: a subroutine package for the calculation of seismic modes solutions, in *Seismological Algorithms*, D. J. Doornbos (ed.), Academic Press, New-York.

Sandoval, S., 2002. *The lithosphere-asthenosphere system beneath Fennoscandia (Baltic shield) by body-wave tomography*, Ph-D thesis, Swiss Federal Institute of Technology, Zurich.

Sandoval, S., E. Kissling, J. Ansorge & the SVEKALAPKO Seismic Tomography Working Group, 2003. High-resolution body wave tomography beneath the SVEKALAPKO array: I. a priori 3D crustal model and associated traveltime effects on teleseismic wavefronts, *Geophys. J. Int.*, **153**, 75–87.

Sandoval, S., E. Kissling, J. Ansorge & the SVEKALAPKO Seismic Tomography Working Group, submitted. High-resolution body wave tomography beneath the SVEKALAPKO array: II. anomalous upper mantle structure beneath central Baltic Shield, *Geophys. J. Int.*.

Simons, F. J., R. D. van des Hilst, J.-P. Montagner & A. Zielhuis, 2002. Multimode Rayleigh wave inversion for heterogeneity and azimuthal anisotropy of the Australian upper mantle, *Geophys., J., Int.*, **151**, 738–754.

Tarantola, A., 1987. *Inverse Problem Theory: Methods for Data Fitting and Parameter Estimation*, Elsevier, Amsterdam.

Tarantola, A. & B. Valette, 1982. Generalized nonlinear inverse problems solved using

the least square criterion, *Rev. Geophys. Space Phys.*, **20**, 219–232.

Tryggvason, E., 1961. Crustal thickness in Fennoscandia from phase velocities of Rayleigh waves, *Annali di Geofisica*, **14**, 267–293.

Vacher, P., A. Mocquet & C. Sotin, 1996. Comparison between tomographic structures and models of convection in the upper mantle, *Geophys. J. Int.*, **124**, 45–56.

Wielandt, E., 1993. Propagation and structural interpretation of non-plane waves, *Geophys. J. Int.*, **113**, 45–53.

Wiener, N., 1949. *Time Series*, M.I.T. Press, Cambridge, Massachusetts.

Conclusions et perspectives

Nous avons développé une nouvelle méthode de tomographie en ondes de surface à l'échelle régionale. Cette méthode a ensuite été appliquée aux données du projet SVEKALAPKO sur le bouclier Balte.

Notre méthode est basée sur le tracé de rais en deux dimensions, sa principale innovation tient au fait que nous prenons en compte la courbure des fronts d'onde incidents sur la zone d'étude [Bruneton *et al.*, 2002]. Les données de l'inversion sont les temps d'arrivée des fronts d'onde en chaque station; le modèle contient les vitesses de phase au travers de la zone d'étude et les temps d'arrivée des fronts d'onde sur les bords de la région étudiée. La modélisation des fronts d'onde est possible parce que les stations sismologiques sont situées à l'intérieur de la zone d'étude et pas simplement sur un bord comme c'est le cas dans une tomographie en ondes de volume. Puisque les ondes de surface sont dispersives, une inversion pour chaque fréquence est nécessaire pour une étude complète. Nous obtenons une carte de vitesse de phase par fréquence. L'ensemble des cartes de vitesse de phase est équivalent à une courbe de dispersion en chaque point. Nous inversons ces courbes de dispersion pour obtenir un modèle tridimensionnel de notre région d'étude en vitesse des ondes S, sous le réseau de stations. Cette méthode relativement simple à mettre en œuvre du fait de l'utilisation de la théorie des rais s'est révélée stable sur les données du projet SVEKALAPKO.

Dans un premier temps les données du projet SVEKALAPKO sont inversées pour obtenir un profil moyen de vitesse des ondes S en fonction de la profondeur

pour toute la région. Calculé à partir des enregistrements de 69 séismes par 46 stations, ce profil est très bien contraint jusqu'à 300 km de profondeur. Les vitesses d'onde S sont environ 4% plus rapides que le modèle de référence ak135 [Kennett *et al.*, 1995] jusqu'à 200 km de profondeur. Nos données ne nécessitent pas la présence d'une zone à moindre vitesse significative qui pourrait être interprétée comme la base de la lithosphère.

Nous avons comparé ces vitesses d'onde S obtenues à partir d'observations d'ondes de surface à des calculs théoriques de vitesses sismiques basés sur la composition de xénolites mantelliques échantillonnées à l'est de la Finlande. Pour la profondeur d'origine des xénolites (160-240 km), la correspondance entre les vitesses d'origine sismique et les vitesses d'origine pétrologique est excellente. La résolution des études sismiques de même que les incertitudes dans l'estimation des paramètres élastiques des minéraux ne permettent toutefois pas de discriminer entre les différents types de péridotites plus ou moins appauvries.

Pour des profondeurs inférieures à 100 km, l'accord entre les courbes basées sur les ondes de surface et sur les xénolites disparaît. Les vitesses obtenues par analyse sismique sont jusqu'à 3% plus faibles que les vitesses théoriques. Qui plus est le gradient de vitesse avec la profondeur observé en sismologie est pratiquement nul (légèrement positif ou négatif suivant les modèles et la profondeur) alors qu'une composition constante donne toujours un gradient de vitesse sensiblement négatif dans la lithosphère. Nos données sismiques ne peuvent pas être expliquées sans une stratification de la lithosphère, la partie superficielle jusqu'à 100 km étant formée d'un matériau plus lent. Nous avons testé des compositions de roches mantelliques issues de la littérature pouvant produire des vitesses plus faibles: péridotites hydratées, éclogites ou compositions provenant d'interactions entre la croûte et le manteau. Le métasomatisme peut être du à des épisodes de subduction qui peuvent également incorporer du matériel crustal dans le manteau superficiel, donnant des éclogites. Des échanges entre la croûte inférieure et le manteau pourraient produire des résidus de la formation de granitoïdes par fusion dans la croûte, ou bien des cumulats de différenciation de magma picritique resté bloqué à la base de la croûte [Arndt & Goldstein, 1989].

Nous nous sommes ensuite intéressé aux variations latérales, c'est-à-dire à un modèle tridimensionnel en vitesse des ondes S. L'utilisation des ondes de surface entraîne une sensibilité aux variations latérales qui diminue avec la profondeur. Pour les périodes suppérieures à 100 s la longueur d'onde est supérieure à l'ouverture du réseau, nous limitons donc notre modèle tridimensionnel aux 150 premiers kilomètes de profondeur. Les variations latérales de vitesse sont au maximum de $\pm$ 3% par rapport au modèle moyen. Les études de flux de chaleur et des interfaces de la zone de transition du manteau par fonctions récepteur montrent que ces hétérogénéités ne peuvent pas être dues à des variations de température, elles sont forcément produites par des variations de composition chimique. Il peut s'agir de péridotites plus ou moins fertiles ou appauvries, de degrés de métasomatisme différents ou de compositions anormales, par exemple mélangées avec des constituants de la croûte.

Notre modèle est caractérisé par des vitesses rapides dans la croûte inférieure et dans les 100 premiers kilomètres du manteau dans les régions montrant un Moho anormalement profond. Les granitoïdes de Rapakivi semblent être associés à une zone lente jusqu'à 150 km de profondeur.

La principale structure géologique de la zone d'étude – la frontière entre la Carélie archéenne et la Svecofennie protérozoïque – n'a pas de signature dans les images de tomographie sismologique. Toutefois en classant les profils de vitesse en fonction de la profondeur obtenus en différents points, nous obtenons quatre familles principales et cinq intermédiaires dont la position correspond à la géologie de surface et à un certain nombre d'autes études géophysiques. La comparaison des profils des différentes familles avec les vitesses calculées à partir de compositions de xénolithes implique à la fois des variations latérales et verticales de la composition de la lithosphère sous le Bouclier Balte. Le centre du Bouclier Balte semble formé de plusieur blocs lithosphériques de composition différentes accrétés.

Nous avons pour l'instant analysé les données large-bande de l'expérience de sismologie passive du projet SVEKALAPKO en interprétant les temps d'arrivée d'ondes de Rayleigh en terme de structure 3D isotrope en vitesse des ondes S et en terme de profil moyen. De nombreuses études sont encore possibles pour exploiter ces données.

Nous n'avons pas abordé le problème de l'anisotropie dans ce travail. Plomerova *et al.* [2003] ont montré par des études de résidus de temps d'arrivée des ondes P et de biréfringence des ondes S, que l'anisotropie du manteau sous la Fennoscandie était relativement complexe. En séparant dans nos données les événements provenant de différents azimuts nous pouvons obtenir la valeur moyenne de l'anisotropie azimutale. La prise en compte de l'anisotropie peut modifier notre modèle tridimensionnel en vitesse des ondes S, en particulier en ce qui concerne les amplitudes des variations.

A l'origine du projet SVEKALAPKO deux mini-réseaux de stations large-bande ont été prévus de part et d'autre de la suture Archéen-Protérozoïque. Les mini-réseaux sont utilisés pour mesurer la structure en vitesse des onde S à la verticale de leur situation, ainsi que pour estimer les directions de propagation des ondes de surface [Cotte *et al.*, 2000]. Toutefois, de par leur petite taille par rapport aux longueurs d'onde utilisées, les mesures de vitesse de phase sont difficiles et les vitesses peuvent être influencées par une large zone autour du réseau. La situation de ces deux mini-réseaux au centre d'une expérience plus large doit permettre de tester la résolution des mesures basées sur ces techniques. Il serait en effet possible de comparer les vitesses et directions de propagation obtenues par analyse de réseau sur les stations proches aux valeurs obtenues en utilisant l'ensemble des stations de l'expérience SVEKALAPKO.

Enfin nous avons calculé les directions de propagation apparentes du mode fondamental de l'onde de Rayleigh sur le réseau de stations sans les exploiter directement. Ces mesures devraient nous permettre de quantifier dans le cas d'une

région relativement simple et homogène les écarts entre la direction réelle de propagation des ondes de surface et le grand cercle. Dans les Alpes, Cotte *et al.* [2000] ont observé des écarts maximum au grand cercle de 30°, la moitié étant attribuée à la propagation à l'échelle globale et la moitié à des effets locaux. Il serait donc intéressant de vérifier ces conclusions dans une région géodynamiquement très différente.

Pour tenter de répondre aux questions restées en suspens, la comparaison avec un modèle en vitesse absolue des ondes P serait très utile. En effet les comportements des vitesses d'ondes P et S diffèrent face aux variations possibles de composition et aux variations de température.

Enfin pour élargir l'étude de la composition des boucliers, il serait intéressant de conduire une expérience de sismologie d'ampleur semblable à SVEKALAPKO dans une région où l'échantillonnage des xénolithes est plus important qu'en Finlande.

Bibliographie

Arndt, N. T. & S. L. Goldstein, 1989. An open boundary between lower continental crust and mantle: its role in crust formation and crustal recycling, *Tectonophysics*, **161**, 201–212.

Bruneton, M., V. Farra, H. A. Pedersen & the SVEKALAPKO Seismic Tomography Working Group, 2002. Non-linear surface wave phase velocity inversion based on ray theory, *Geophys. J. Int.*, **151**, 583–596.

Cotte, N., H. A. Pedersen, M. Campillo, V. Farra & Y. Cansi, 2000. Off-great circle propagation of intermediate period surface waves as observed on a dense array in the French Alps, *Geophys. J. Int.*, **142**, 825–840.

Kennett, B. L. N., E. R. Engdhal & R. Buland, 1995. Constraints on seismic velocities in the Earth from traveltimes, *Geophys. J. Int.*, **122**, 108–124.

Plomerová, J., T. L. Hyvönen, V., Babuška, L., Vecsey, T., Raita, the SVEKALAPKO Seismic Tomography Working Group & the TOR Working Group, 2003. Seismic-wave anisotropy of the subcrustal lithosphere of Fennoscandia based on body-wave data recorded during the international passive experiments, *EGS-AGU-EUG Joint*

Meeting, Session TS2.02 The deep structure of continents, Bock G., Daly S., Nice 2003-04, abstract EAE03-A-03891.

Bibliographie

Aki, K. & P. G. Richards, 2002. *Quantitative seismology*, second edition, University Science Books, Sausalito, California.

Aki, K., A. Christoffersson & E. S. Husebye, 1977. Determination of 3-dimensional seismic structure of lithosphere, *J. Geophys. Res.*, **82**, 277–296.

Alinaghi, A., G. Bock, R. Kind, W. Hanka, K. Wylegalla, TOR and SVEKALAPKO Groups, 2003. Receiver function analysis of the crust and upper mantle from the North German Basin to the Archean Baltic Shield. *Geophys. J. Int.*, 155, 641–652.

Arlitt, R., 1999. *Teleseismic body wave tomography across the Trans-European Suture Zone between Sweden and Denmark*, thèse de doctorat, Swiss Federal Institute of Technology, Zurich.

Arndt, N. T. & S. L. Goldstein, 1989. An open boundary between lower continental crust and mantle: its role in crust formation and crustal recycling, *Tectonophysics*, **161**, 201–212.

Babuška, V., J. Plomerová & P. Pajdušák, 1988. Seismologically determined deep lithosphere structure in Fennoscandia, Proceedings in *Geologiska Föreningens i Stockholm Förhandlingar*, **110**, 380–382.

Barker, J. S., M. Campillo, F. J. Sánchez-Sesma, D. Jongmans & S. K. Singh, 1996. Analysis of wave propagation in the valley of Mexico from a dense array of seismometers, *Bull. Seism. Soc. Am.*, **86**, 1667–1680.

Bartels, R. H., J. C. Beatty & B. A. Barsky, 1988. *B-splines*, Hermès, Paris.

Baumont, D., 1999. *Caractérisation sismologique de la structure lithosphérique des Andes Centrales (17°-20°)*, thèse de doctorat, Université Joseph Fourier, Grenoble.

Bock, G. & the SVEKALAPKO Seismic Tomography Working Group, 2001. Seismic probing of Fennoscandian lithosphere, *EOS, Trans. Am. Geophys. Un.*, **82**, 621, 628–629.

Bousquet R., B. Goffé, P. Henry, X. Le Pichon & C. Chopin, 1997. Kinematic, thermal and petrological model of the Central Alps: Lepontine metamorphism in the upper crust and eclogitisation of the lower crust, *Tectonophysics*, **273**, 105–127.

Boyd, F. R., 1989. Compositional distinction between oceanic and cratonic lithosphere, *Earth Plant. Sci. Lett.*, *96*, 15–26.

Brueckner, H. K., D. A. Carswell & W. L. Griffin, 2002. Paleozoic diamonds within a Precambrian peridotite lens in UHP gneisses of Norwegian Caledonides, *Earth Planet. Sci. Lett.*, **203**, 805–816.

Bruneton, M., V. Farra, H. A. Pedersen & the SVEKALAPKO Seismic Tomography Working Group, 2002. Non-linear surface wave phase velocity inversion based on ray theory, *Geophys. J. Int.*, **151**, 583–596.

Calcagnile, G., 1982. The lithosphere-asthenosphere system in Fennoscandia, *Tectonophysics*, **90**, 19–35.

Calcagnile, G., 1991. Deep structure of Fennoscandia from fundamental and higher mode dispersion of Rayleigh waves, *Tectonophysics*, **195**, 139–149.

Červený, V., 1989. Ray tracing in factorized anisotropic inhomogeneous media, *Geophys. J. Int.*, **99**, 91–100.

Červený, V., I. A. Molotov & I. Pšenčik, 1977. *Ray method in seismology*, Univerzita Karlova, Praha.

Cotte, N. & H. A. Pedersen, 2002. Sharp contrast in lithospheric structure across the Sorgenfrei-Tornquist Zone as inferred by Rayleigh wave analysis of TOR1 project data, *Tectonophysics*, **360**, 75–88.

Cotte, N., H. A. Pedersen, M. Campillo, J. Ni, R. Kind, E. Sandvol & W. Zhao, 1999. Determination of the crustal structure in South Tibet by dispersion and amplitude analysis of surface waves, *Geophys. J. Int.*, **138**, 809–819.

Cotte, N., H. A. Pedersen, M. Campillo, V. Farra & Y. Cansi, 2000. Off-great circle propagation of intermediate period surface waves as observed on a dense array in the French Alps, *Geophys. J. Int.*, **142**, 825–840.

Coulomb J. & G. Jobert (eds.), 1972. *Traité de géophysique interne, tome 1: sismologie et pesanteur*, Masson & C^{ie}, Paris.

Courant, R. & D. Hilbert, 1966. *Methods of mathematical physics*, Intersciences Publishers, Inc., New-York.

Dalrymple, G. B., 1991. *The age of the Earth*, Stanford University Press, Stanford, California.

de Boor, C., 1978. *A practical guide to splines*, Springer-Verlag, New-York.

Deschamps, G. A., 1972. Ray techniques in electromagnetics, *Proc. IEEE*, **60**, 1022–1035.

Dziewonski, A. M. & D. L. Anderson, 1981. Preliminary reference Earth model, *Phys. Earth Planet. Int.*, **25**, 297–356.

Edgard, A. D., F. E. Lloyd, D. M. Forsyth & L. R. Barnett, 1989. Origin of glass in upper mantle xenoliths from Quaternary volcanics of Gees, West Eifel, Germany, *Contrib. Mineral. Petrol.*, **103**, 277–286.

Engels, M., T. Korja and the BEAR Working Group, 2002. Multisheet modelling of the electrical conductivity structure in the Fennoscandian Shield, *Earth Planets Space*, **54**, 559–573.

Farra, V., 1990. Amplitude computation in heterogeneous media by ray perturbation theory: a finite element approach, *Geophys. J. Int.*, **103**, 341–354.

Farra, V., 1993. Ray tracing in complex media, *J. appl. Geophys.*, **30**, 55–73.

Farra, V. & R. Madariaga, 1987. Seismic waveform modeling in heterogeneous media by ray perturbation theory, *J. Geophys. Res.*, **92**, 2697–2712.

Farra, V. & R. Madariaga, 1988. Non-linear reflection tomography, *Geophys. J.*, **95**, 135–147.

Fouch, M. J., D. E. James, J. C. Vandecar, S. van der Lee & the Kaapvaal Seismic Group, submitted. Mantle seismic structure beneath the Kaapvaal and Zimbabwe cratons, *S. Africa J. Geol.*.

Fowler, C. M. R., 1990. *The solid Earth, an introduction to global geophysics*, Cambridge University Press.

Friederich, W., 1998. Wave-theoretical inversion of teleseismic surface waves in a regional network: phase-velocity maps and a three-dimensional upper-mantle shear-wave-velocity model for southern Germany, *Geophys. J. Int.*, **132**, 203–225.

Friederich, W., 2003. The S-velocity structure of the East Asian mantle from inversion of shear and surface waveforms, *Geophys. J. Int.*, **153**, 88-102.

Friederich, W. & E. Wielandt, 1995. Interpretation of seismic surface waves in regional networks: joint estimation of wave-field geometry and local phase velocity; Method and numerical tests, *Geophys. J. Int.*, **120**, 731–744.

Friederich, W., E. Wielandt & S. Stange, 1993. Multiple forward scattering of surface waves: comparison with an exact solution and Born single-scattering methods, *Geophys. J. Int.*, **112**, 264–275.

Friederich, W., E. Wielandt & S. Stange, 1994. Non-plane geometries of seismic surface wavefields and their implications for regional surface-wave tomography, *Geophys. J. Int.*, **119**, 931–948.

Gao, S., R. L. Rudnick, R. W. Carlson, W. F. McDonough & Y.-S. Liu, 2002. Re-Os evidence for replacement of ancient mantle lithosphere beneath the North China craton, *Earth Planet. Sci. Lett.*, **198**, 307–322.

Gee, D. G. & H. J. Zeyen (eds.), 1996. *EUROPROBE 1996 – lithosphere dynamics:*

origin and evolution of continents, EUROPROBE secretariat, Uppsala University, Uppsala, Sweden.

Goes, S., R. Govers & P. Vacher, 2000. Shallow mantle temperatures under Europe from P and S wave tomography *J. Geophys. Res.*, **105**, 11153–11169.

Gorbatschev, R. & S. Bogdanova, 1993. Frontiers in the Baltic Shield. *Precambrian Res.*, **64**, 3–21.

Gregersen, S. & the TOR Working Group, 1999. Important findings expected from Europe's largest seismic array, *EOS, Trans. Am. Geophys. Un.*, **80**, 1–2.

Herrin, E. & T. Goforth, 1977. Phase-matched filters: application to the study of Rayleigh waves, *Bull. Seism. Soc. Am.*, **67**, 1259–1275.

Herrmann, R. B., 1985. *Computer Programs in seismology, Volume III: Surface waves in plane layers*, Saint Louis University, Missouri.

Herrmann, R. B., 1987. *Computer Programs in seismology, Volume IV: Surface waves inversion*, Saint Louis University, Missouri.

Hjelt, S.-E. & J. S. Daly, 1996. SVEKALAPKO, evolution of Paleoproterozoic and Archean lithosphere, in *EUROPROBE 1996 – lithosphere dynamics: origin and evolution of continents*, D. G. Gee and H. J. Zeyen (eds.), EUROPROBE secretariat, Uppsala University, Uppsala, Sweden.

Husebye, E. S. & J. Hovland, 1982. On upper mantle seismic heterogeneities beneath Fennoscandia, *Tectonophysics*, **90**, 1–17.

Hwang, H. J. & B. J. Mitchell, 1986. Interstation surface wave analysis by frequency-domain Wiener deconvolution and modal isolation, *Bull. Seism. Soc. Am.*, **76**, 847-864.

Ionov, D. A., U. Kramm & H. G. Stosch, 1992. Evolution of the upper mantle beneath the southern Baikal rift zone; an Sr-Nd isotope study of xenoliths from the Bartoy volcanoes, *Contrib. Mineral. Petrol.*, **111**, 235–247.

James, D. E., M. J. Fouch, J. C. VanDecar, S. van der Lee & the Kaapvaal Seismic Group, 2001. Tectospheric structure beneath southern Africa, *Geophys. Res. Lett.*, **28**, 2485–2488.

Jeffreys, H & K. E. Bullen, 1940. Seismological Tables, *British Association for the Advancement of Science*, Gray Milne Trust (reprinted 1970).

Jobert, N. & G. Jobert, 1987. Ray tracing for surface waves, in *Seismic tomography with applications in global seismology and exploration geophysics*, G. Nolet (ed.), D. Reidel publishing company, Dordrecht, 275–300.

Jordan, T. H., 1979. The deep structure of the continents, *Scientific American*, **240**, 92–107.

Keilis-Borok, V. I. (ed.), 1989. *Seismic surface waves in laterally inhomogeneous Earth*, Kluwer Academic Publishers, Dordrecht.

Kennett, B. L. N. & K. Yoshizawa, 2002. A reappraisal of regional surface wave tomography, *Geophys. J. Int.*, **150**, 37–44.

Kennett, B. L. N., E. R. Engdhal & R. Buland, 1995. Constraints on seismic velocities in the Earth from traveltimes, *Geophys. J. Int.*, **122**, 108–124.

Korja, A., T. Korja, U. Luosto & P. Heikkinen, 1993. Seismic and geoelectric evidence for collisional and extensional events in the Fennoscandian Shield – implications for Precambrian crustal evolution, *Tectonophysics*, **219**, 129–152.

Korja, T., M. Engels, A. A. Zhamaletdinov, A. A. Kovtun, N. A. Palshin, M. Y. Smirnov, A. D. Tokarev, V. E. Asming, L. V. Vanyan, I. L. Vardaniants and the BEAR Working Group, 2002. Crustal conductivity in Fennoscandia – a compilation of a database on crustal conductance in the Fennoscandian Shield, *Earth Planets Space*, **54**, 535–558.

Kozlovskaya, E., S. Elo, S.-E. Hjelt, J. Yliniemi, M. Pirttijärvi & The SVEKALAPKO Seismic Tomography Working Group, submitted. 3D density model of the crust of southern and central Finland obtained from joint interpretation of SVEKALAPKO crustal P-wave velocity model and gravity data, *Geophys. J. Int.*.

Kukkonen, I. T., 1993. Heat-flow map of northern and central parts of the Fennoscandian Shield based on geochemical surveys of heat producing elements, *Tectonophysics*, **225**, 3–13.

Kukkonen, I. T. & A. Jõeleht, 1996. Geothermal modelling of the lithosphere in the central Baltic shield and its southern slope, *Tectonophysics*, **255**, 24–45.

Kukkonen, I. T. & P. Peltonen, 1999. Xenolith-controlled geotherm for the central Fennoscandian Shield: implications for lithosphere-asthenosphere relations. *Tectonophysics*, **304**, 301–315.

Kukkonen, I. T., K. Kinnunen & P. Peltonen, 2003. Mantle xenoliths and thick lithosphere in the Fennoscandian Shield, *Physics and Chemistry of the Earth*, **28**, 349–360.

Lander, A. V., A. L. Levshin, 1989. Recording, identification, and measurement of surface wave parameters, in *Seismic surface waves in laterally inhomogeneous Earth*, V. I. Keilis-Borok (ed.), Kluwer Academic Publishers, Dordrecht, 131–182.

Lévêque, J.-J., M. Cara & D. Rouland, 1991. Waveform inversion of surface wave data: test of a new tool for systematic investigation of upper mantle structures, *Geophys. J. Int.*, **104**, 565–581.

Levshin, A. L., 1989. Surface waves in media with weak lateral inhomogeneity, in *Seis-*

mic surface waves in a laterally inhomogeneous Earth, V. I. Keilis-Borok (ed.), Kluwer Academic Publishers, Dordrecht, 35–69.

Levshin, A. L. & K.-A. Berteussen, 1979. Anomalous propagation of surface waves in the Barents Sea as inferred from NORSAR recordings, *Geophys. J. R. astr. Soc.*, **56**, 97–118.

Lomax, A. & R. Snieder, 1995. The contrast in upper mantle shear-wave velocity between the East European Platform and Tectonic Europe obtained with genetic algorithm inversion of Rayleigh wave group dispersion, *Geophys. J. Int.*, **123**, 169–182.

Luosto, U., 1990. Seismic data from the northern segment of the EGT and from the nearby profiles, in *The European Geotransverse (EGT) Project, data compilations and synoptic interpretation*, R. Freeman & St. Mueller (eds.), 53–63.

Luosto, U., 1997. Structure of the Earth's crust in Fennoscandia as revealed from refraction and wide-angle reflection studies, *Geophysica*, **33**, 3–16.

Marquering, H. & R. Snieder, 1996. Shear-wave velocity structure beneath Europe, the northeastern Atlantic and western Asia from waveform inversions including surface-wave mode coupling, *Geophys. J. Int.*, **127**, 283–304.

Marquering, H., R. Snieder & G. Nolet, 1996. Waveform inversions and the significance of surface-wave mode coupling, *Geophys. J. Int.*, **124**, 258–278.

Maupin, V., 1988. Surface waves across 2D structures: a method based on coupled local modes, *Geophys. J.*, **93**, 173–185.

Maupin, V. & M. Cara, 1992. Love-Rayleigh wave incompatibility and possible deep upper mantle anisotropy in Iberian Peninsula *Pure app. Geophys.*, *138*, 429–444.

McMechan, G. A. & M. J. Yedlin, 1981. Analysis of dispersive waves by wave field transformation, *Geophysics*, **46**, 869–874.

Montagner, J. P. & B. L. N. Kennett, 1996. How to reconcile body-wave and normal-mode reference Earth model? *Geophys. J. Int.*, **125**, 229–248.

Montagner, J.-P. & T. Tanimoto, 1991. Global upper mantle tomography of seismic velocities and anisotropies, *J. Geophys. Res.*, **96**, 20337–20351.

Nielson, J. E., J. R. Budahn, D. M. Unruh & H. G. Wilshire, 1993 Actualistic models of mantle metasomatism documented in a composite xenolith from Dish Hill, California, *Geochim. Cosmochim. Acta*, **57**, 105–121.

Nironen, M., R. Lahtinen & A. Korja, 2002. Paleoproterozoic tectonic evolution of the Fennoscandian shield – comparison to modern analogues, in *Lithosphere 2002 – second symposium on the structure, composition and evolution of the lithosphere in Finland. Programme and extended abstracts, Espoo, Finland*, R. Lahtinen, A. Korja, K. Arhe, O. Eklund, S.-E. Hjelt and L. J. Pesonen (eds.), Institute of Seismology, University of Helsinki, report S-42, 95–97.

Nolet, G., 1987. Seismic wave propagation and seismic tomography, in *Seismic tomography with applications in global seismology and exploration geophysics*, G. Nolet (ed.), D. Reidel publishing company, Dordrecht.

Nolet, G., 1990. Partitioned waveform inversion and two-dimensional structure under the Network of Autonomously Recording Seismographs, *J. Geophys. Res.*, **95**, 8499–8512.

Nur, A., 1987. Seismic rock properties for reservoir descriptions and monitoring, in *Seismic tomography with applications in global seismology and exploration geophysics*, G. Nolet (ed.), D. Reidel publishing company, Dordrecht, 203–237.

Nyblade, A. A., 1999. Heat flow and the structure of Precambrian lithosphere, *Lithos*, **48**, 81–91.

Olivier, J., 1962. A summary of observed seismic surface wave dispersion, *Bull. Seism. Soc. Am.*, **52**, 81–86.

Pearson, D. G., G. J. Irvine, R. W. Carlson, M. G. Kopylova & D. A. Ionov, 2002. The development of lithospheric keels beneath the earliest continents: time constraints using PGE and Re-Os isotope systematics, in *The early Earth: physical, chemical and biological development*, C. M. R. Fowler, C. J. Ebinger & C. J. Hawkesworth (eds.), Geologycal Society, London, Special Publication, **199**, 65–90.

Pedersen, H. A., F. J. Sánchez-Sesma & M. Campillo, 1994. Three-dimensional scattering by two-dimensional topographies, *Bull. Seism. Soc. Am.*, **84**, 1169–1183.

Pedersen, H. A., V. Maupin & M. Campillo, 1996. Wave diffraction in multi-layered media with the Indirect Boundary Element Method: application to 3-D diffraction of long-period surface waves by 2-D lithospheric structures, *Geophys. J. Int.*, **125**, 545–558.

Pedersen, H. A., O. Coutant, A. Deschamps & M. Soulage, 2003. An improved algorithm for measuring surface wave phase velocities beneath a small broad-band array. Application to the French Alps, *Geophys. J. Int.*, sous presse.

Plomerová, J., T. L. Hyvönen, V. Babuška, L. Vecsey, T. Raita, the SVEKALAPKO Seismic Tomography Working Group & the TOR Working Group, 2003. Seismic-wave anisotropy of the subcrustal lithosphere of Fennoscandia based on body-wave data recorded during the international passive experiments, *EGS-AGU-EUG Joint Meeting*, Session TS2.02 The deep structure of continents, Bock G., Daly S., Nice 2003-04, abstract EAE03-A-03891.

Pollitz, F. F., 1999. Regional velocity structure in northern California from inversion of scattered seismic surface waves, *J. Geophys. Res.*, **104**, 15043–15072.

Poupinet, G., W. L. Ellsworth & J. Fréchet, 1984. Monitoring velocity variations in the

crust using earthquake doublets: an application to the Calaveras fault, California, *J. Geophys. Res.*, **89**, 5719–5731.

Röhm, A. H., R. K. Snieder, S. Goes & J. Trampert, 2000. Thermal structure of the continental upper mantle inferred from S wave velocity and surface heat flow, *Earth Planet. Sci. Lett.*, **181**, 395–408.

Sacks, I. S., J. A. Snoke & E. S. Husebye, 1979. Lithosphere thickness beneath the Baltic Shield, *Tectonophysics*, **56**, 101–110.

Saito, M., 1988. Disper 80: a subroutine package for the calculation of seismic modes solutions, in *Seismological Algorithms*, D. J. Doornbos (ed.), Academic Press, New-York.

Sandoval, S., 2002. *The lithosphere-asthenosphere system beneath Fennoscandia (Baltic Shield) by body-wave tomography*, thèse de doctorat, Swiss Federal Institute of Technology, Zurich.

Sandoval, S., E. Kissling, J. Ansorge & the SVEKALAPKO Seismic Tomography Working Group, 2003. High-resolution body wave tomography beneath the SVEKALAPKO array: I. A priori 3D crustal model and associated traveltime effects on teleseismic wavefronts, *Geophys. J. Int.*, **153**, 75–87.

Sandoval, S., E. Kissling, J. Ansorge & the SVEKALAPKO Seismic Tomography Working Group, submitted. High-resolution body wave tomography beneath the SVEKALAPKO array: II. anomalous upper mantle structure beneath central Baltic Shield, *Geophys. J. Int.*.

Shapiro, N. M., M. Campillo, A. Paul, S. K. Singh, D. Jongmans & F. J. Sánchez-Sesma, 1997. Surface-wave propagation across the Mexican Volcanic Belt and the origin of the long-period seismic-wave amplification in the valley of Mexico, *Geophys. J. Int.*, **128**, 151–166.

Shomali, H. Z., R. G. Roberts & the TOR Working Group, 2002. Non-linear body wave teleseismic tomography along the TOR array, *Geophys. J. Int.*, **148**, 562–574.

Simons, F. J., A. Zielhuis & R. D. van der Hilst, 1999. The deep structure of the Australian continent from surface wave tomography, *Lithos.*, **48**, 17–43.

Simons, F. J., R. D. van des Hilst, J.-P. Montagner & A. Zielhuis, 2002. Multimode Rayleigh wave inversion for heterogeneity and azimuthal anisotropy of the Australian upper mantle, *Geophys., J., Int.*, **151**, 738–754.

Snieder, R., 1988a. Large-scale waveform inversion of surface waves for lateral heterogeneity, 1. Theory and numerical examples, *J. Geophys. Res.*, **93**, 12055–12065.

Snieder, R., 1988b. Large-scale waveform inversion of surface waves for lateral heterogeneity, 2. Application to surface waves in Europe and the Mediterranean, *J. Geophys. Res.*, **93**, 12067–12080.

Tarantola, A., 1987. *Inverse problem theory: methods for data fitting and parameter estimation*, Elsevier, Amsterdam.

Tarantola, A. & B. Valette, 1982. Generalized nonlinear inverse problems solved using the least square criterion, *Rev. Geophys. Space Phys.*, **20**, 219–232.

Tromp, J. & F. A. Dahlen, 1992. Variational principles for surface wave propagation on a laterally heterogeneous Earth – II. frequency-domain JWKB theory, *Geophys. J. Int.*, **109**, 599–619.

Tromp, J. & F. A. Dahlen, 1993. Surface wave propagation in a slowly varying anisotropic waveguide, *Geophys. J. Int.*, **113**, 239–249.

Tryggvason, E., 1961. Crustal thickness in Fennoscandia from phase velocities of Rayleigh waves, *Annali di Geofisica*, **14**, 267–293.

Vacher, P., A. Mocquet & C. Sotin, 1996. Comparison between tomographic structures and models of convection in the upper mantle, *Geophys. J. Int.*, **124**, 45–56.

van der Lee, S., 1998. Observations and origin of Rayleigh-wave amplitude anomalies, *Geophys. J. Int.*, **135**, 691–699.

Wielandt, E., 1993. Propagation and structural interpretation of non-plane waves, *Geophys. J. Int.*, **113**, 45–53.

Wiener, N., 1949. *Time series*, M.I.T. Press, Cambridge, Massachusetts.

Yanovskaya, T. B., 1996. Ray tomography based on azimuthal anomalies, *Pure appl. Geophys.*, **148**, 319–336.

Yanovskaya, T. B., E. S. Kizima & L. M. Antonova, 1998. Structure of the crust in the Black Sea and adjoining regions from surface wave data, *J. Seismology*, **2**, 303–316.

Yoshizawa, K. & B. L. N., Kennett, 2002. Non-linear waveform inversion for surface waves with a neighbourhood algirithm – application to multimode dispersion measurements, *Geophys. J. Int.*, **149**, 118–133.

Zielhuis, A. & G. Nolet, 1994. Shear-wave velocity variations in the upper mantle beneath central Europe, *Geophys. J. Int.*, **117**, 695–715.

Thèse de doctorat de l'**Université Joseph Fourier – Grenoble I**

Préparée au **Laboratoire de Géophysique Interne et Tectonophysique**

par **Marianne BRUNETON**

Etude de la structure lithosphérique 3D du Bouclier Balte par l'analyse des ondes de Rayleigh

La tomographie sismologique à l'échelle régionale peut donner des informations sur la structure profonde des continents anciens.

Nous développons une méthode de tomographie en ondes de surface, puis nous l'appliquons aux ondes de Rayleigh du projet SVEKALAPKO (bouclier Balte). Cette méthode est basée sur le tracé de rais 2D, elle tient compte de la courbure des fronts d'onde incidents.

Le profil moyen en vitesse des ondes S obtenu est de 4des modèles de Terre standards et ne présente pas de zone à moindre vitesse. La comparaison avec des données issues de xénolithes implique une stratification chimique de la lithosphère.

Le modèle 3D présente des variations latérales de $\pm$3attribuées à des différences de composition des roches. La limite Archéen-Protérozoïque n'a pas de signature nette peut-être à cause d'une modification du manteau à grande échelle au cours du Protérozoïque et/ou de la structure complexe du domaine Protérozoïque, héritée de sa formation.

Mots Clefs: tomographie sismologique, ondes de surface, ondes de Rayleigh lithosphère, Bouclier Balte.

3D lithospheric structure of the central Baltic Shield from Rayleigh wave analysis

Regional seismic tomography can provide information on the deep structure of old continents.

We develop a surface-wave teleseismic tomography method and apply it to the Rayleigh waves recorded during the SVEKALAPKO deep seismic experiment (Baltic Shield). This method is based on 2D ray tracing and takes into account the curvature of incoming wavefronts.

The obtained regional-average S-wave velocity profile is 4than standard Earth models for depths down to 200 km. It does not present any low velocity zone. Comparisons with xenolith-derived data imply a chemically-stratified lithospheric mantle.

The 3D model presents lateral amplitude variations of $\pm$3must be due to varying rock compositions. The Archean-Proterozoic boundary does not show a clear signature in the tomographic model. This is possibly due to a large-scale modification of the mantle during Proterozoic times and/or to the complex formation of the Proterozoic domain resulting in a complex structure.

Key words: tomography, surface waves, Rayleigh waves, lithosphere, Baltic Shield.